NCAR/TN–469+STR
NCAR TECHNICAL NOTE
January 2006

A Baroclinic Wave Test Case for Dynamical Cores of General Circulation Models: Model Intercomparisons

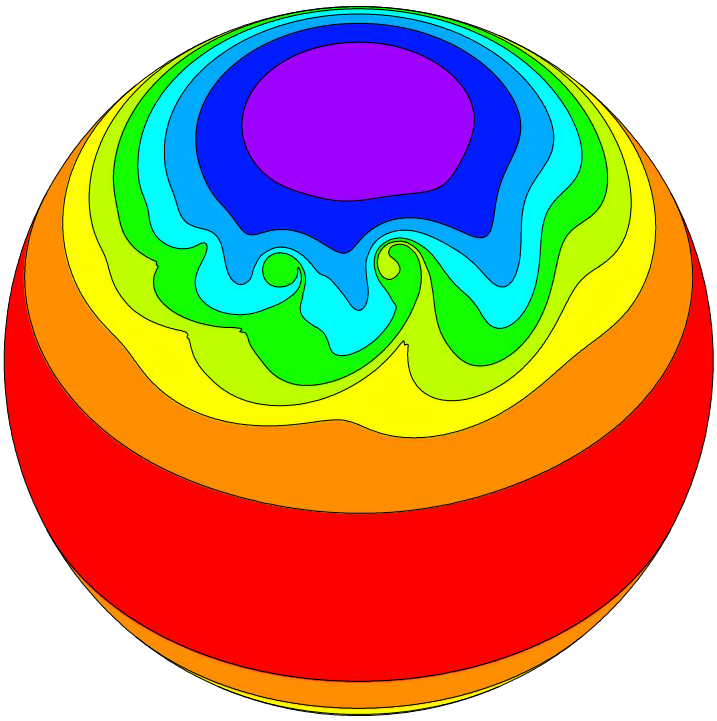

Christiane Jablonowski

Advanced Study Program and
Scientific Computing Division
National Center for Atmospheric Research
Boulder, Colorado, USA

David L. Williamson

Climate and Global Dynamics Division
National Center for Atmospheric Research
Boulder, Colorado, USA

NCAR TECHNICAL NOTES

The Technical Note series provides an outlet for a variety of NCAR manuscripts that contribute in specialized ways to the body of scientific knowledge but which are not suitable for journal, monograph, or book publication. Reports in this series are issued by the NCAR Scientific Divisions; copies may be obtained on request from the Publications Office of NCAR. Designation symbols for the series include:

EDD: *Engineering, Design, or Development Reports*
Equipment descriptions, test results, instrumentation, and operating and maintenance manuals.

IA: *Instructional Aids*
Instruction manuals, bibliographies, film supplements, and other research or instructional aids.

PPR: *Program Progress Reports*
Field program reports, interim and working reports, survey reports, and plans for experiments.

PROC: *Proceedings*
Documentation of symposia, colloquia, conferences, workshops, and lectures. (Distribution may be limited to attendees.)

STR: *Scientific and Technical Reports*
Data compilations, theoretical and numerical investigations, and experimental results.

The National Center for Atmospheric Research (NCAR) is operated by the University Corporation for Atmospheric Research (UCAR) and is sponsored by the National Science Foundation. Any opinions, findings, conclusions, or recommendations expressed in this publication are those of the author(s) and do not necessarily reflect the views of the National Science Foundation.

Contents

List of Figures

List of Tables

Acknowledgments

We would like to thank Jerry Olson (NCAR, Climate ad Global Dynamics Division) for his help with the CAM3 Eulerian and semi-Lagrangian dynamical cores. In addition, we thank Detlev Majewski and Aurelia Müller (German Weather Service DWD) for providing us with the GME source code.

CJ was partially supported by NASA Headquarters under the Earth System Science Fellowship Grant NGT5-30359 and DLW by the Office of Biological and Environmental Research, U. S. Department of Energy, as part of its Climate Change Prediction Program.

Preface

A deterministic initial value test case for dynamical cores of atmospheric general circulation models is presented that assesses the evolution of an idealized baroclinic wave in the Northern Hemisphere. The initial zonal state is quasi-realistic and completely defined by analytic expressions which are a steady-state solution of the hydrostatic primitive equations. A two-component test strategy first evaluates the ability of the discrete approximations to maintain the steady-state solution. Then an overlaid perturbation is introduced which triggers the growth of a baroclinic disturbance over the course of several days.

The test is applied to four very different dynamical cores at varying horizontal and vertical resolutions. In particular, the NCAR/NASA Finite Volume dynamics package, the NCAR spectral transform Eulerian and the semi-Lagrangian dynamical cores of the Community Atmosphere Model CAM3 are evaluated. In addition, the icosahedral finite-difference model GME of the German Weather Service (DWD) is tested. These dynamical cores represent a broad range of numerical approaches and, at very high resolutions, provide independent reference solutions. This report discusses the convergence-with-resolution characteristics of the schemes and evaluates the uncertainty of the high resolution reference solutions.

Chapter 1

Introduction

Tests of atmospheric General Circulation Models (GCMs) and, in particular, dynamical core assessments are important steps towards future model improvements. They reveal the influence of an individual model design on climate and weather simulations and indicate whether the circulation is described representatively by the numerical approach. Testing a global 3D atmospheric model is not straightforward. In the absence of non-trivial analytic solutions, the model evaluations most commonly rely on intuition, experience and model intercomparisons like AMIP, the Atmospheric Model Intercomparison Project (Gates 1995; Gates et al. 1999). In addition, GCM simulation statistics are typically compared to global reanalysis data while numerical weather forecasts are compared to local observations. Such approaches are not applicable to pure dynamical core assessments that isolate the dynamics package from the physical parameterizations.

Very few standard test cases for 3D dynamical cores on the sphere have been developed to date. Among them are the long-term idealized benchmarks as suggested by Held and Suarez (1994) and Boer and Denis (1997). They require 1200-day model integrations with simple, pre-defined forcing functions that replace the complex physics parameterizations. Typically time-mean zonal-mean flow fields are evaluated for both test scenarios that assess the model's idealized climatic state and its variability. But as a consequence, the averaging of the flow patterns essentially eliminates all small-scale flow features in the analysis although these are the main contributors to the creation of the mean state. Improvements of the statistical mean state are therefore directly related to an improved representations of the fine-scale flow characteristics.

Standard techniques for short-term baroclinic dynamical core assessments can only rarely be found in the literature. This is in contrast to the long history of test cases available for shallow water models (see Williamson et al. (1992) for a collection). One deterministic test technique was suggested by Polvani and Saravanan (2000) who simulated the breakdown of the polar vortex in a 3D dynamical core. The definition of this test case was inspired by earlier 1D and 2D studies of the vortex erosion problem. These were conducted by Juckes and McIntyre (1987) and Bates and Li (1997), respectively, who applied the 1D principles to the 2D shallow water framework. In addition, Giraldo and Rosmond (2004) used a 3D version of the classical Rossby-Haurwitz test (Phillips 1959) for dynamical core assessments. This 3D extension of the shallow water Rossby-Haurwitz wave was derived by Monaco and Williams (1975). Other early test techniques from the 70s, like the baroclinic wave problem used in Hoskins and Simmons (1975), have not been widely applied by the community. Most often, the lack of a concise test specification make these tests difficult to use and interpret, especially in comparing new schemes to older results.

As modeling groups now move towards the next generation of dynamical cores with new nu-

merical schemes and gridding options (Tomita and Sato 2004; Bonaventura 2003; Fournier et al. 2004; Giraldo and Rosmond 2004) a standard test suite for hydrostatic and non-hydrostatic dynamics packages is highly desirable. With the baroclinic instability test case described here we contribute to this effort. The new test is based on four design principles. In particular, it is deterministic, easy-to-use, relevant to typical atmospheric phenomena and applicable to a wide variety of model formulations and grids.

The test assesses the evolution of an idealized baroclinic wave in the Northern Hemisphere over a short 10-day time period. In addition, the initial conditions can also be used to test the ability of a model to maintain a non-trivial, analytic steady-state solution. Recently, a similar baroclinic wave test case has been independently developed by Polvani et al. (2004) (hereafter POL). The main difference between POL and the test proposed here is that POL prescribe an explicit second-order horizontal diffusion mechanism that significantly damps the evolution of the baroclinic wave, in particular the cascade mechanism at small scales. Additionally, the POL test requires the numerical evaluation of 1D integrals to define a quasi-realistic balanced flow in the Northern Hemisphere. In contrast, the test proposed here starts from a reasonably realistic initial data set in both hemispheres which is completely represented by analytic expressions. Overall, the evolution in POL is dominated by strong diffusion processes that eliminate small-scale features expected to be resolved at higher resolutions. This diffusion is needed to obtain the exact numerical convergence of two models assessed in their study. On the other hand, POL also shows that any other choice of the diffusion mechanism leads to a truly different numerically converged flow field.

Our test is designed to evaluate dynamical cores in the form that will be applied to Numerical Weather Prediction (NWP) and climate simulations at the resolutions typically used for these applications. Thus the aim of the new test presented here is not to compute a numerically converged diffusive solution but to assess the accuracy of solutions at any resolved scale. An analytic solution to the problem is not known. We compute a set of reference solutions with a variety of models at very high resolution. This set is used to estimate the uncertainty in any of the reference solutions. Throughout this report, we consider the subgrid-scale diffusivity as part of the numerical scheme as also argued by Held and Suarez (1994). Indeed, for some schemes, such as those incorporating nonlinear shape preservation, the inherent diffusion can not be isolated. Thus this test allows the comparison of schemes with very different diffusive behaviors, like a spectral transform semi-Lagrangian method (Collins et al. 2004) or a monotonic finite volume technique (Lin 2004), that do not require explicit horizontal diffusion to control the solution spectra at the small scales. In contrast, alternative schemes, like a spectral transform Eulerian method (Collins et al. 2004) or a finite difference approach on an icosahedral grid (Majewski et al. 2002), generally apply a rather scale-selective fourth-order horizontal diffusion mechanism to prevent the accumulation of kinetic energy in the smallest scales or to ensure numerical stability. These four types of models are compared herein. The study sheds light on the convergence-with-resolution model characteristics and defines a set of reference solutions along with their uncertainties.

The report is organized as follows. The design principles of the baroclinic wave test case as well as the derivation and discussion of the initial conditions are presented in Section 2 (with further details in appendix A). Section 3 briefly summarizes the four dynamical cores used in the study. The models represent a broad range of numerical approaches and provide independent reference solutions. In Section 4 the models are assessed in a steady-state scenario without an explicitly imposed trigger for a baroclinic perturbation. This approach reveals how well the dynamical cores maintain the zonally symmetric initial state. The evolution of the baroclinic wave is discussed in

Section 5. In particular, this section includes a model intercomparison and assesses the uncertainty of the reference solutions. The findings are summarized in Section 6.

Chapter 2

Definition of the test case

The underlying concept of the initial value test was inspired by ideas in Hoskins and Simmons (1975) and Simmons and Hoskins (1975) who used a numerically balanced initial flow with a superimposed wavenumber 8 perturbation. In contrast to these authors though, the new idealized test is entirely described by analytic initial conditions with a local nonperiodic perturbation (Jablonowski 2004; Jablonowski and Williamson 2006). The initial data can therefore be immediately computed on any computational mesh.

The deterministic test is comprised of two parts. First, the dynamical core is initialized with steady-state, balanced initial conditions that are an analytic solution to the hydrostatic primitive equations. This model setup reveals how well a dynamical core maintains this initial state before numerical round-off and truncation errors as well as gravity waves degrade the steady-state. Second, a relatively large-scale but localized Gaussian hill perturbation is superimposed onto the zonal wind in the northern midlatitudes. This small-amplitude disturbance triggers the evolution of a baroclinic wave over the course of several days.

2.1 The initial state

The baroclinic wave test case has been developed for dry dynamical cores with pressure-based vertical coordinates like the pure pressure coordinate p, the hybrid η coordinate (Simmons and Burridge 1981) or the pure $\sigma = p/p_s$ coordinate (Phillips 1957) where p_s symbolizes the surface pressure. The latter two coordinate systems are typically used in GCMs today. The definition of the η coordinate together with the specification of all model levels for the integrations herein are provided in appendix B. It is important to note that constant η-surfaces coincide with constant σ or pressure surfaces if there are no variations in the surface pressure, which is the case here. The choice of the vertical coordinate system is therefore left to the modeling group despite the fact that each vertical coordinate system implies a different boundary condition for the vertical velocity. In practice, this has been found to be insignificant for the evolution of the baroclinic wave over a 10-day time period (not shown).

The initial state is defined by analytic expressions in spherical (λ, φ, η) coordinates where $\lambda \in [0, 2\pi]$ stands for the longitude and $\varphi \in [-\pi/2, \pi/2]$ represents the latitude. The subsequent expressions can also be straightforwardly transformed into different, e.g. Cartesian, coordinate systems. All physical constants used in the test specification are listed below. Users of the test case are encouraged to select the same parameter set in their models to foster future model intercom-

parisons.

Assuming that a model utilizes η-levels an auxiliary variable η_v is defined by

$$\eta_v = (\eta - \eta_0)\,\frac{\pi}{2} \tag{2.1}$$

with $\eta_0 = 0.252$. In case of a vertical σ coordinate the η-level in Eq. (2.1) can be simply replaced with the corresponding σ value. This principle applies to all subsequent equations. Eq. (2.1) can also be directly applied to models with pure pressure coordinates if $\eta = \sigma = p/p_s$ is adopted at each pressure level p. The surface pressure p_s is constant and given by $p_s(\lambda, \varphi) = 10^5$ Pa.

The flow field is comprised of two symmetric zonal jets in midlatitudes. The zonal wind u is defined as

$$u(\lambda, \varphi, \eta) = u_0\, \cos^{\frac{3}{2}} \eta_v\, \sin^2(2\,\varphi) \quad . \tag{2.2}$$

Here the maximum amplitude u_0 is set to 35 m s^{-1} which is close to the wind speed of the zonal-mean time-mean jet streams in the troposphere. The meridional wind v is set to zero. This flow field in nondivergent and allows the derivation of the analytic initial data even for models in vorticity-divergence (ζ,δ) form. In particular, the radial outward component of the relative vorticity ζ is given by

$$\zeta(\lambda, \varphi, \eta) = \frac{-4\,u_0}{a}\, \cos^{\frac{3}{2}} \eta_v\, \sin\varphi\, \cos\varphi\, (2 - 5\sin^2\varphi) \tag{2.3}$$

and $\delta = 0$ s^{-1} is automatically fulfilled. $a = 6.371229 \times 10^6$ m indicates the mean radius of the Earth.

The horizontally averaged temperature $\langle\, T(\eta)\rangle$ is split into two representations for the lower (Eq. (2.4)) and middle (Eq. (2.5)) atmosphere. This introduces the characteristic atmospheric temperature profiles especially at upper levels. They are given by

$$\langle\, T(\eta)\rangle = T_0\, \eta^{\frac{R_d \Gamma}{g}} \qquad \text{(for } \eta_s \geq \eta \geq \eta_t\text{)} \tag{2.4}$$

$$\langle\, T(\eta)\rangle = T_0\, \eta^{\frac{R_d \Gamma}{g}} + \Delta T\, (\eta_t - \eta)^5 \qquad \text{(for } \eta_t > \eta\text{)} \tag{2.5}$$

with the surface level $\eta_s = 1$, the tropopause level $\eta_t = 0.2$ and the horizontal-mean temperature at the surface $T_0 = 288$ K. The temperature lapse rate Γ is set to 0.005 K m^{-1} which is similar to the observed diabatic lapse rate. Additionally, the empirical temperature difference $\Delta T = 4.8 \times 10^5$ K is chosen. $R_d = 287.0$ J (kg K)$^{-1}$ represents the ideal gas constant for dry air and $g = 9.80616$ m s^{-2} is the gravitational acceleration. The total temperature distribution comprises the horizontal-mean temperature and a horizontal variation at each level. It is given by

$$\begin{aligned} T(\lambda, \varphi, \eta) = \langle\, T(\eta)\rangle + \frac{3}{4}\, \frac{\eta\, \pi\, u_0}{R_d}\, \sin\eta_v\, \cos^{\frac{1}{2}} \eta_v\, \times \\ \Big\{ \Big(-2\sin^6\varphi\, (\cos^2\varphi + \frac{1}{3}) + \frac{10}{63} \Big)\, 2\, u_0\, \cos^{\frac{3}{2}} \eta_v + \\ \Big(\frac{8}{5} \cos^3\varphi\, (\sin^2\varphi + \frac{2}{3}) - \frac{\pi}{4} \Big)\, a\, \Omega \Big\} \end{aligned} \tag{2.6}$$

where $\Omega = 7.29212 \times 10^{-5}$ s^{-1} denotes the Earth's angular velocity.

The surface geopotential Φ_s completes the description of the steady-state initial conditions. The orography field balances the non-zero zonal wind at the surface and Φ_s is determined by

$$\begin{aligned}\Phi_s(\lambda,\varphi) = u_0\ \cos^{\frac{3}{2}}\Big((\eta_s-\eta_0)\,\frac{\pi}{2}\Big)\times \\ \Big\{\Big(-2\sin^6\varphi\,(\cos^2\varphi+\frac{1}{3})+\frac{10}{63}\Big)\,u_0\,\cos^{\frac{3}{2}}\Big((\eta_s-\eta_0)\,\frac{\pi}{2}\Big)+ \\ \Big(\frac{8}{5}\cos^3\varphi\,(\sin^2\varphi+\frac{2}{3})-\frac{\pi}{4}\Big)\,a\,\Omega\Big\}. \end{aligned} \tag{2.7}$$

Besides the assessment of the steady-state solution, the test is primarily designed to simulate the evolution of a baroclinic wave. It can be triggered if the initial conditions are overlaid with a perturbation. Here a perturbation with a Gaussian profile is selected and centered at $(\lambda_c,\varphi_c) = (\pi/9, 2\pi/9)$ which points to the location (20°E,40°N). The perturbation u' of the zonal wind

$$u'(\lambda,\varphi,\eta) = u_p\ \exp\Big(-\Big(\frac{r}{R}\Big)^2\Big) \tag{2.8}$$

with radius $R = a/10$ and maximum amplitude $u_p = 1$ m s^{-1} is superimposed on the zonal wind field (Eq. (2.2)) by adding u' to u at each grid point at all model levels. Here the great circle distance r is given by

$$r = a\ \arccos\Big(\sin\varphi_c\ \sin\varphi+\cos\varphi_c\ \cos\varphi\ \cos(\lambda-\lambda_c)\Big)\quad . \tag{2.9}$$

The corresponding (ζ',δ') perturbations for models in vorticity-divergence form are

$$\begin{aligned}\zeta'(\lambda,\varphi) = \frac{u_p}{a}\,\exp\Big(-\Big(\frac{r}{R}\Big)^2\Big)\ \times\ \Big\{\tan\varphi- \\ 2\Big(\frac{a}{R}\Big)^2\,\arccos(X)\,\frac{\sin\varphi_c\,\cos\varphi-\cos\varphi_c\,\sin\varphi\,\cos(\lambda-\lambda_c)}{\sqrt{1-X^2}}\Big\}\end{aligned} \tag{2.10}$$

$$\delta'(\lambda,\varphi) = \frac{-2\,u_p\,a}{R^2}\,\exp\Big(-\Big(\frac{r}{R}\Big)^2\Big)\,\arccos(X)\,\frac{\cos\varphi_c\ \sin(\lambda-\lambda_c)}{\sqrt{1-X^2}} \tag{2.11}$$

with $X = \big(\sin\varphi_c\ \sin\varphi+\cos\varphi_c\ \cos\varphi\ \cos(\lambda-\lambda_c)\big)$. For both singular points (λ_c,φ_c) and $(\lambda_c+\pi,-\varphi_c)$ with $X^2 = 1$, δ' is identical zero. In addition, $\zeta'(\lambda_c,\varphi_c) = u_p\tan\varphi/a$ is well-defined and $\lim_{\lambda\to\lambda_c+\pi,\varphi\to-\varphi_c}\zeta'$ is zero. Similarly, $\lim_{\varphi\to\pm\frac{\pi}{2}}\zeta'$ is zero at the poles.

2.2 Characteristics of the initial data

The balanced initial flow field comprises a zonally symmetric basic state with a jet in the mid-latitudes of each hemisphere and a quasi-realistic temperature distribution, which are displayed in Figs. 2.1(a) and (b). In addition, the figure shows the profile of the surface geopotential (Fig. 2.1(c)), three selected vertical temperature distributions on a logarithmic scale (Fig. 2.1(d)) and the unperturbed relative vorticity field ζ (Fig. 2.1(e)) . Overall, the atmospheric conditions resemble the climatic state of a winter hemisphere reasonably well. The centers of the midlatitudinal jets at 45°N/S are placed at the pressure level $p = 252$ hPa, which lies just below the

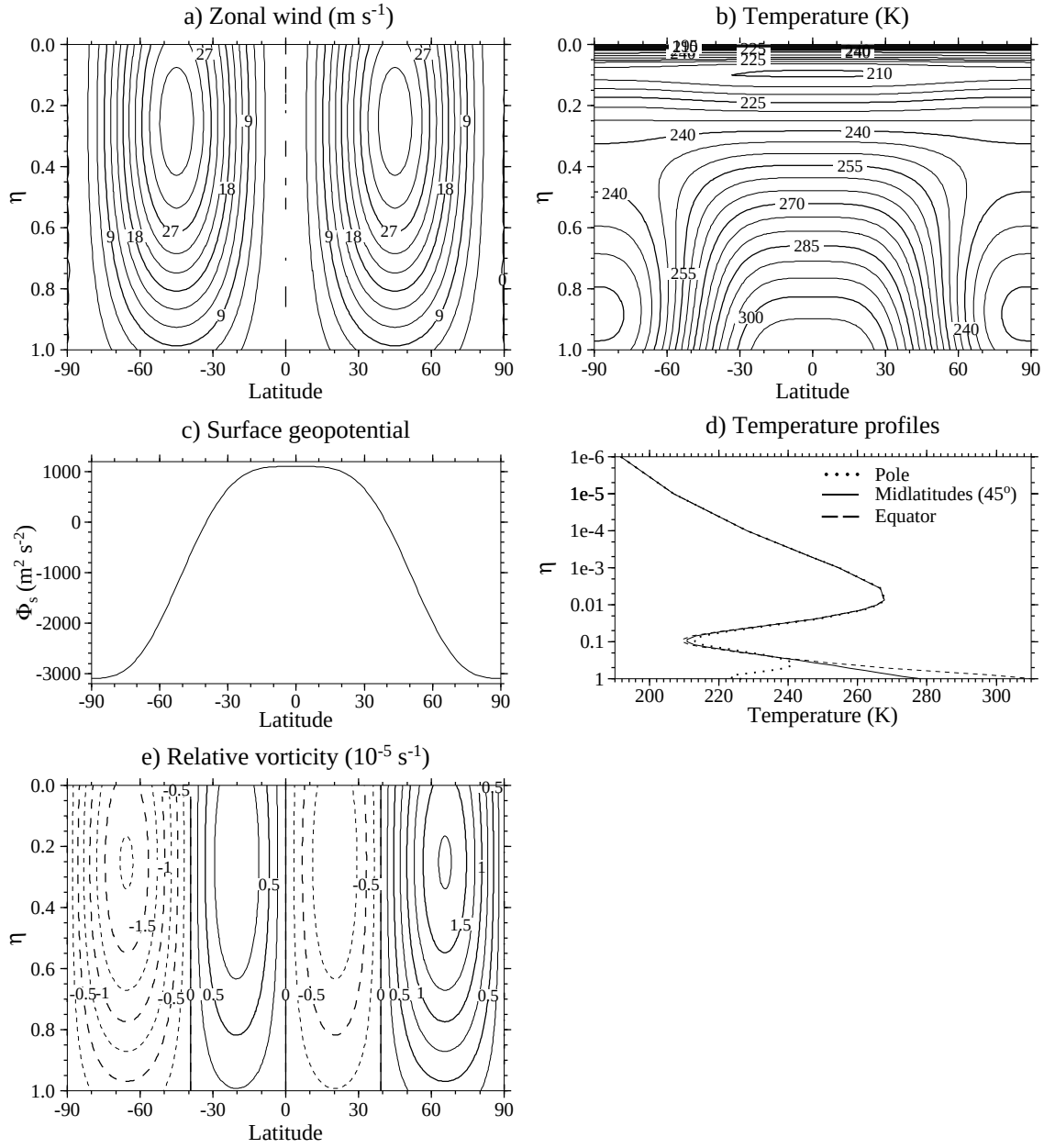

Figure 2.1: Initial conditions for the (a) unperturbed zonal wind u, (b) temperature T, (c) surface geopotential Φ_s, (d) three vertical temperature profiles at the equator, $45°$N/S and the poles, and (e) the relative vorticity ζ.

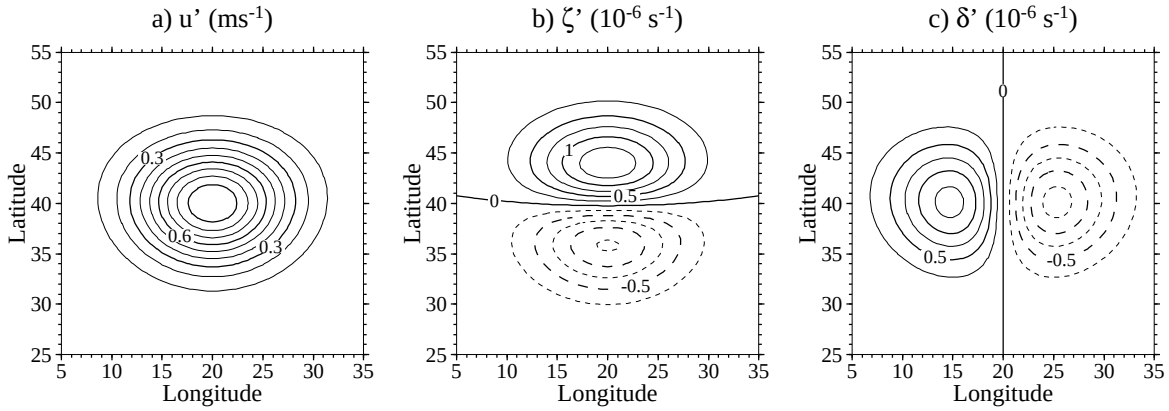

Figure 2.2: Perturbation patterns for the (a) zonal wind, (b) relative vorticity and (c) divergence. The zero contour in (a) is omitted.

tropopause level at $p = 200$ hPa. Furthermore, the globally averaged temperature of this distribution is approximately 256.4 K, which closely matches the observed global temperature of the atmosphere. The horizontally averaged temperature at the surface is selected to be $< T >= 288$ K which corresponds exactly to the surface temperature of the so-called U.S. standard atmosphere (U.S. Standard Atmosphere 1976). In addition, the temperature distribution captures an idealized stratospheric and mesospheric temperature profile and prescribes a low-level temperature inversion in polar regions. A baroclinic wave can be triggered if these balanced initial conditions are overlaid with a perturbation at each model level. Figure 2.2 shows the suggested perturbation patterns for the zonal wind u', the relative vorticity ζ' and the divergence δ', respectively. The latter two are provided for models in vorticity-divergence form.

The test design guarantees static, inertial and symmetric stability properties, but is unstable with respect to baroclinic or barotropic instability mechanisms. These two forms of instabilities result from the vertical and meridional wind shear characteristics. In particular, the growth rate of the baroclinic disturbance highly depends on the strength of the vertical shear. The inertial, symmetric and static stability criteria are analyzed in Fig. 2.3. Figures 2.3(a) and (b) show the absolute and potential vorticity fields. The flow is stable with respect to inertial motions since the absolute vorticity field $(\zeta + 2\Omega \sin \varphi)$ of the basic flow is positive in the Northern Hemisphere and negative in the Southern Hemisphere (Holton 1992). The same argument holds for the potential vorticity that indicates the symmetric stability of the flow. Here the potential vorticity PV is assessed in form of the Ertel potential vorticity. Similar distributions of the Ertel potential vorticity have also been found by Simmons and Hoskins (1976).

The initial data are also statically stable. This is displayed in Fig. 2.3(c) and (d) which show the potential temperature distribution Θ and the Brunt Väisälä frequency N. The flow is statically stable if the vertical potential temperature gradient $\partial\Theta/\partial z$ with respect to the height z, or equivalently the buoyancy frequency N, is positive everywhere. The latter can clearly be seen in Fig. 2.3(d). Note that the buoyancy frequency at the surface approaches zero at the poles which defines almost neutrally stratified conditions.

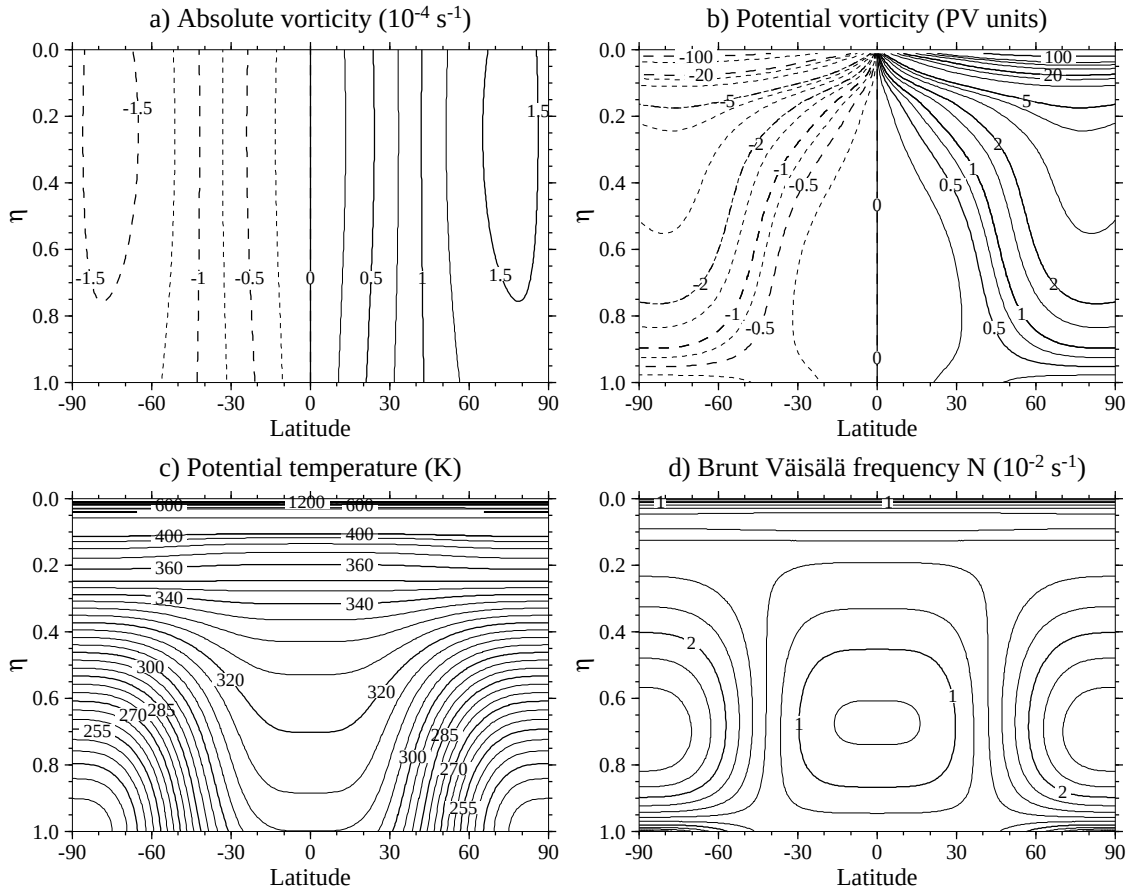

Figure 2.3: Assessment of the stability of the balanced initial conditions: (a) absolute vorticity (inertial stability), (b) potential vorticity with varying contour levels in PV units = 10^{-6} K kg^{-1} m^2 s^{-1} (symmetric stability), (c) potential temperature Θ and (d) Brunt Väisälä frequency N (static stability).

2.3 Test strategy

The following two-step test strategy is suggested. First, the dynamical core is initialized with the balanced initial conditions and run for 30 model days at varying horizontal resolutions. This is a stringent test of the dynamics that not only serves as a debugging tool but also as an assessment tool for the algorithmic design of the numerical scheme and its horizontal grid (Williamson et al. 2006). For these model runs error norms can be directly assessed since the initial state is the true solution (see Section 4). If possible, the unperturbed model simulations should be run without horizontal or vertical diffusion. Most often, the latter is a component of the physics package and therefore already inactive in a dynamical core simulation. In addition, no Rayleigh friction near the model top (if included in the model) should be applied. All three aforementioned diffusion mechanisms would damp the initial data over time which is consequently reflected in the error statistics.

Second, the evolution of a baroclinic wave in the Northern Hemisphere is triggered when using the initial conditions with the overlaid zonal wind perturbation. As before, different horizontal resolutions should be assessed to estimate the convergence characteristics. In general, the baroclinic wave starts growing observably around day 4 and evolves rapidly thereafter with explosive cyclogenesis at model day 8. The wave train breaks after day 9 and generates a full circulation in both hemispheres between day 20-30 depending on the model formulation. Therefore, the simulation should cover at least a 10-day time period that captures the initial and rapid development stages of the baroclinic disturbance. If longer time integrations are performed (e.g. up to 30 days as in the subsequent examples) the spread of the numerical solutions increases noticeably from model day 12 onwards. This indicates the predictability limit of the test case. Nevertheless, the initial development stages of new systems at the leading edge of the baroclinic wave train (compare also to Simmons and Hoskins (1979)) are still predicted reliably until day 16.

The baroclinic wave, although idealized, represents very realistic flow features. Strong temperature fronts develop that are associated with the evolving low and high pressure systems. In addition, the wavenumber with maximum growth rate lies between 5 and 9 (not shown) which agrees well with observations and assessments in the literature (for example Simmons and Hoskins (1977)). It is important to note that the baroclinic wave test case does not have an analytic solution. Therefore, high resolution reference solutions and their uncertainties are assessed in Section 5.

Chapter 3

Description of the dynamical cores

The baroclinic wave test sequence has been applied to the three hydrostatic dynamical cores that are part of NCAR's Community Atmosphere Model version 3 (CAM3). In particular, these are a Finite Volume dynamical core (Lin 2004) and the spectral transform semi-Lagrangian and Eulerian dynamics packages. They are documented in Collins et al. (2004). In addition, the dynamical core of the operational weather forecast model GME at the German Weather Service (DWD) has been tested. This finite-difference model is based on an icosahedral mesh with a triangulated grid structure (Majewski et al. 2002). As mentioned earlier, our test is intended to evaluate dynamical cores as they would be configured for their NWP or climate simulation applications. This includes any diffusion or filtering operators with typical coefficients even if they are not needed for this test. We briefly summarize the four dynamical cores below.

3.1 Eulerian

The Eulerian dynamical core in vorticity-divergence form is based on the traditional three-time-level, semi-implicit spectral transform approximations applied on a quadratically unaliased transform grid with horizontal triangular truncation (Machenhauer 1979). The vertical coordinate is terrain following hybrid pressure. The core includes ∇^4 horizontal diffusion on temperature, divergence and vorticity to control the energy at the smallest resolved scales. The coefficient has been chosen for each resolution to yield a reasonably straight tail for the kinetic energy spectra in realistically forced simulations. The model also includes a ∇^2 horizontal diffusion on the top three levels of the model which serves as a top boundary condition to control upward propagating waves. The temperature equation includes a frictional heating term corresponding to the momentum diffusion. The Eulerian core includes an *a posteriori* mass fixer applied at every time step. An energy fixer is also available with the Eulerian core but was was not invoked for our experiments. The three-time-level core includes a time filter to control the $2\Delta t$ time computational modes.

3.2 Semi-Lagrangian

The semi-Lagrangian dynamical core is based on two-time-level, semi-implicit semi-Lagrangian spectral transform approximations with quasi-cubic Lagrangian polynomial interpolants. Triangular truncation is adopted. The core is based on the same terrain following vertical coordinate as

the Eulerian core. For our experiments we use a quadratically unaliased transform grid. We do not include the ∇^4 and ∇^2 horizontal diffusions which are available in the core; the interpolants control the energy at the smallest resolved scales for the time scales considered here. Since the energy loss due to the damping by the interpolants is not explicitly known, a term corresponding to the ∇^4 diffusive heating in the Eulerian core cannot be derived. Thus an *a posteriori* energy fixer is applied every time step in the model. In addition the *a posteriori* mass fixer is applied every time step as in the Eulerian core.

3.3 Finite Volume

The mass-conservative finite volume dynamical core in flux-form is built upon a 2D shallow water approach in the horizontal plane (Lin and Rood 1996, 1997). The vertical discretization utilizes a "Lagrangian control-volume" principle, which is based on a terrain-following "floating" Lagrangian coordinate system and a fixed "Eulerian" reference frame. In particular, the vertically-stacked finite volumes are allowed to float for a duration of 10 time steps before they are mapped back monotonically and conservatively to the fixed reference system (Lin 2004). The latter coincides with the hybrid levels of CAM3's Eulerian and semi-Lagrangian dynamical cores. The advection algorithm makes use of the monotonic third-order piecewise parabolic method PPM (Colella and Woodward 1984) with an explicit time-stepping scheme. Lower order approximations are applied near the model top to add extra diffusion at the upper boundary. This configuration has been used for both the steady-state and baroclinic wave simulations. The FV dynamics package is built upon a regular latitude-longitude grid and employs both a weak 3-point digital filter in midlatitudes as well as an FFT filter in polar regions. These control the unstable waves in the zonal direction that result from the convergence of the computational grid near the poles. The FV dynamical core does not include explicit horizontal ∇^4 or ∇^2 diffusion terms. The smallest scales are controlled by the monotonicity constraints of the numerical scheme. In addition, a divergence damping mechanism is applied that damps the divergence δ in the form of $\nabla^2(\nu\delta)$ where ν is a spatially varying divergence damping coefficient. As with the semi-Lagrangian core, the energy loss due to the numerical damping is not explicitly known. Therefore, an *a posteriori* energy fixer is applied that has the same form as that in the semi-Lagrangian model.

3.4 GME

The dynamical core of the weather prediction system GME applies a finite-difference approximation with local spherical basis functions at each grid point. The horizontal grid is based on an icosahedron which is further subdivided into smaller triangles. An Arakawa-A grid staggering is chosen that places the prognostic variables at the vertices of the triangles. In the vertical direction GME utilizes the same terrain following η coordinate as the CAM3 Eulerian dynamics package. The semi-implicit numerical scheme is second-order accurate and applies a classical Leapfrog three-time-level approach with an Asselin time filter. Due to the quasi-uniformity of the computational grid no longitudinal FFT-filtering is needed. The smallest scales are controlled by a ∇^4 horizontal diffusion mechanism that is applied to the prognostic wind and temperature variables u, v and T. Near the model top the ∇^4 diffusion is replaced with a stronger ∇^2 diffusion operator that serves as a top boundary condition. Neither a mass fixer nor an energy fixer is applied.

3.5 Resolutions and model parameters

For the basic experiments here which examine the effect of horizontal resolution we adopt the standard 26 vertical levels (L26) used to produce the CAM3 control simulations (Collins et al. 2006). For mid-range horizontal resolutions we also calculate the solutions with increased and decreased vertical resolution: 49 levels (L49), which essentially halve the thickness of the standard 26-level grid intervals, and the 18 levels (L18) used for the standard simulations of the predecessor of CAM3, the Community Climate Model version 3 (CCM3) (Kiehl et al. 1998). In all level setups, the centers of the topmost levels lie between 3 and 5 hPa (see appendix B for the exact level placement).

3.5.1 Eulerian (EUL)

Table 3.1 lists the horizontal resolutions, time steps and ∇^4diffusion coefficients K_4 for the spectral transform Eulerian dynamical core. The abbreviation T symbolizes a triangular truncation which is followed by the maximum resolved wavenumber. The ∇^2 horizontal diffusion coefficient, $K_2 = 2.5 \times 10^5$ m^2 s^{-1}, is independent of horizontal resolution.

Table 3.1: Horizontal grid resolutions, time steps and diffusion coefficients for the spectral Eulerian (EUL) dynamical core in CAM3. The ∇^2 horizontal diffusion coefficient, $K_2 = 2.5 \times 10^5$ m^2 s^{-1}, is independent of horizontal resolution.

Eulerian (EUL)				
Spectral Resolution	# Grid points lat $\times$ lon	Grid distance at the equator	Time step Δt	Diffusion coefficient K_4 (m^4 s^{-1})
T21	32 $\times$ 64	625 km	2400 s	2.0×10^{16}
T42	64 $\times$ 128	313 km	1200 s	1.0×10^{16}
T85	128 $\times$ 256	156 km	600 s	1.0×10^{15}
T170	256 $\times$ 512	78 km	300 s	1.5×10^{14}
T340	512 $\times$ 1024	39 km	150 s	1.5×10^{13}

3.5.2 Semi-Lagrangian (SLD)

The same resolutions as in the Eulerian case are tested (see Table 3.1). In contrast though, the time step Δt is three times the corresponding Eulerian value and both diffusion coefficients K_4 and K_2 are set to zero. The standard CAM3 SLD decentering parameter $\epsilon = 0.2$ is used.

3.5.3 Finite Volume (FV)

The Finite Volume dynamical core is run at the horizontal resolutions listed in Table 3.2. The table also shows the approximate equatorial grid distances in physical space to ease the comparison to the other dynamical cores.

Table 3.2: Horizontal grid resolutions and time steps for the Finite Volume (FV) dynamical core in CAM3.

Finite Volume (FV)			
Resolution $\Delta\varphi \times \Delta\lambda$	# Grid points lat × lon	Grid distance at the equator $\Delta y \times \Delta x$	Time step Δt
$4^\circ \times 5^\circ$	46×72	435 km × 556 km	720 s
$2^\circ \times 2.5^\circ$	91×144	220 km × 278 km	360 s
$1^\circ \times 1.25^\circ$	181×288	111 km × 139 km	180 s
$0.5^\circ \times 0.625^\circ$	361×576	55 km × 69 km	90 s
$0.25^\circ \times 0.3125^\circ$	721×1152	28 km × 35 km	45 s

3.5.4 GME

The horizontal grid of GME is based on an icosahedron with 20 equilateral triangles. The sides of these base triangles are further subdivided into ni equal intervals. The corresponding maximum and minimum grid distances, time steps and diffusion coefficients are listed in Table 3.3.

Table 3.3: Horizontal grid resolutions, time steps and diffusion coefficients for GME with an icosahedral grid.

GME						
Resolution ni	# Grid points	Min. grid distance	Max. grid distance	Time step Δt	Diffusion coefficients K_4 (m^4 s^{-1})	K_2 (m^2 s^{-1})
16	2562	440 km	526 km	1600 s	5.0×10^{16}	2.0×10^6
32	10242	220 km	263 km	800 s	6.0×10^{15}	1.5×10^6
64	40962	110 km	132 km	400 s	1.0×10^{15}	1.0×10^6
128	163842	55 km	66 km	200 s	1.2×10^{14}	2.0×10^5
256	655362	26 km	33 km	100 s	1.2×10^{13}	2.5×10^4

3.6 Run time

The run times of the four dynamical cores at their mid-range and second-highest resolutions and 26 levels are listed in Table 3.4. The table serves as a general guide for the computational costs of each model while acknowledging that such costs are hardware-dependent and vary with the ingenuity of the programmer. The run time data represent the wallclock time needed to complete one model day on a 32-processor node of an IBM Power4 architecture when using a pure MPI (Message Passing Interface) parallelization approach. Identical compiler optimization flags were used for all models. No effort was made to optimize the numerical schemes or to configure the models in their optimal setups, such as selecting an optimal time step or switching from a quadratic to a linear truncation technique in case of EUL and SLD. The dynamical cores represent the standard versions in CAM3 and GME, respectively.

Table 3.4: Wallclock time (s) for one model day measured on a 32-processor node of an IBM Power4 architecture. The run times are listed for the mid-range and second-highest horizontal resolutions and 26 levels.

	Wallclock time (s) for 1 day			
Horizontal resolution	EUL	SLD	FV	GME
T85 — $1^\circ \times 1.25^\circ$ — ni64	44	24	66	48
T170 — $0.5^\circ \times 0.625^\circ$ — ni128	483	271	625	325
increase in run time by a factor of	11.0	11.3	9.5	6.8

Table 3.4 shows that the semi-Lagrangian dynamical core clearly outperforms EUL, FV and GME. At T85 the SLD dynamical core is roughly twice as fast as the other three models at the comparable resolutions. At the higher resolution T170 though, the computational advantage of the SLD model diminishes especially in comparison to GME. This is mainly due to a better cache utilization and reduced parallel overhead in GME. GME shows a superlinear parallel speedup as the horizontal resolution is doubled and the time step is halved. In general, this corresponds to an increase in the workload by a factor of 8 when disregarding any additional work for the parallelization. Here, the increase in the wallclock time for GME ni128 lies around a factor of 7, whereas the EUL T170, SLD T170 and FV $0.5^\circ \times 0.625^\circ$ dynamical cores show an increase in the run time by a factor between 9.5-11.3 compared to the lower resolutions. Nevertheless, the SLD T170 run is still the most cost-effective approach while giving similar simulation results as shown later.

Chapter 4

Results: Steady state test case

All four dynamical cores have been initialized with the steady-state initial conditions and run for 30 model days at varying horizontal resolutions and 26 levels. In an ideal case the models are expected to perfectly maintain the initial state which is the true solution. In practice though, the initial state degrades over time as discussed below. The errors are quantified via unnormalized l_2 error norms. In particular, two types of error measures are used that are applied to the zonal wind field u.

The first l_2 error norm evaluates the symmetry-deviations from the zonal average. It is defined as

$$\begin{aligned} l_2\big(u(t)-\overline{u}(t)\big) &= \left(\frac{1}{4\,\pi} \int_0^1 \int_{-\frac{\pi}{2}}^{\frac{\pi}{2}} \int_0^{2\pi} \left[u(\lambda,\varphi,\eta,t)-\overline{u}(\varphi,\eta,t)\right]^2 \cos\varphi \, d\lambda \, d\varphi \, d\eta \right)^{1/2} \\ &\approx \left(\frac{\sum_k \sum_j \sum_i \left[u(\lambda_i,\varphi_j,\eta_k,t)-\overline{u}(\varphi_j,\eta_k,t)\right]^2 w_j \, \Delta\eta_k}{\sum_k \sum_j \sum_i w_j \, \Delta\eta_k} \right)^{1/2} \end{aligned} \tag{4.1}$$

where the overbar $\overline{(\,)}$ denotes the zonal average and the sums with indices (i,j,k) are taken over all longitude points λ_i, latitude points φ_j and vertical levels η_k of the global grid. The summation weights w_j are the Gaussian weights for the calculations on the spectral transform grids. On uniform grids $w_j = |\sin(\varphi_{j+1/2}) - \sin(\varphi_{j-1/2})|$ is used where the half indices denote the location of the cell interfaces in the meridional direction. The weights $\Delta\eta_k = (\eta_{k+1/2} - \eta_{k-1/2})$ indicate the thickness of a model layer. Here the half indices $k \pm 1/2$ point to the locations of the level interfaces. Eq. (4.1) assumes that the longitudinal grid points are equally spaced.

The second l_2 norm assesses the degradation of the zonal average with respect to the true solution. It is defined by

$$\begin{aligned} l_2\big(\overline{u}(t)-\overline{u}(t=0)\big) &= \left(\frac{1}{2} \int_0^1 \int_{-\frac{\pi}{2}}^{\frac{\pi}{2}} \left[\overline{u}(\varphi,\eta,t)-\overline{u}(\varphi,\eta,t=0)\right]^2 \cos\varphi \, d\varphi \, d\eta \right)^{1/2} \\ &\approx \left(\frac{\sum_k \sum_j \left[\overline{u}(\varphi_j,\eta_k,t)-\overline{u}(\varphi_j,\eta_k,t=0)\right]^2 w_j \, \Delta\eta_k}{\sum_k \sum_j w_j \, \Delta\eta_k} \right)^{1/2} . \end{aligned} \tag{4.2}$$

For both analyses the GME data are biquadratically interpolated to a regular latitude–longitude grid that is identical to the FV grid at a comparable resolution (see Tables 3.2 and 3.3). In general,

alternative numerical approximations to the integrals can also be chosen if models with non-regular computational meshes are assessed.

Figure 4.1 compares the zonal-symmetry characteristics (Eq. (4.1)) of the dynamical cores. The simulations with EUL and FV at all horizontal resolutions show that both models maintain the zonal symmetry exactly up to machine precision (no figure shown). This is in contrast to SLD (Fig. 4.1(a)) and GME (Fig. 4.1(b)) which develop zonal asymmetries immediately after the start of the simulation. In case of SLD the asymmetries grow continuously and become clearly visible after approximately four weeks, especially in surface maps of the meridional wind (not shown). Here it is interesting to note that the growth of the zonal asymmetry is slightly faster at increased

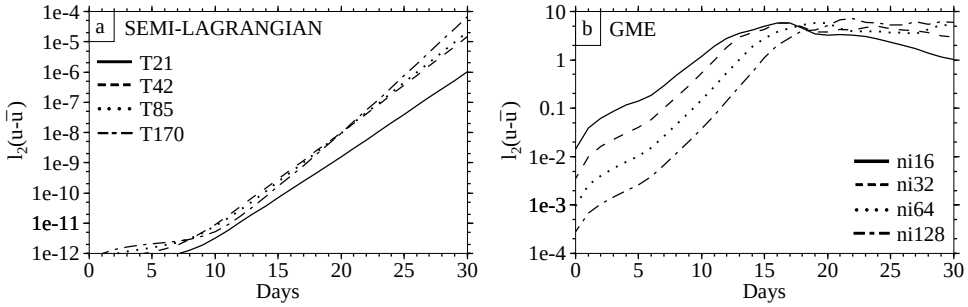

Figure 4.1: l_2 norm of $u - \bar{u}$ in m s^{-1} for the (a) semi-Lagrangian and (b) GME dynamical cores at varying horizontal resolutions and 26 levels.

resolution because of the decreased damping from the interpolations at higher resolution. The asymmetries are introduced at the machine precision level by calculations that involve the longitudes of the grid points such as the departure point which is calculated as an offset from the arrival grid point. Thus the relative location of the departure point within the grid interval will differ at the rounding level for the points on a latitude circle even though the offset is the same to machine precision. In contrast, the Eulerian spectral and Finite Volume methods use only the grid interval and not the actual longitudes of grid points and thus the calculations at all longitudes on a given latitude circle are identical. Other calculations in the semi-Lagrangian core that introduce rounding-level perturbations along latitude circles are the local geodesic trajectory calculations, the rotation of the unit vectors associated with the advection of a vector wind, and the calculation of a wavenumber one polar wind vector used for meridional interpolation which should be zero in this case but is only so to rounding (see Williamson and Olson (1994) and Collins et al. (2004) for algorithm details). We note that these are details of the particular implementation in the CAM3 SLD core. It is possible to devise coding strategies that would not introduce rounding level longitudinal asymmetries, such as by interpolating differences from arrival point values rather than full fields. However, the elimination of rounding level longitudinal asymmetries seems unimportant in practical atmospheric applications. In case of GME (Fig. 4.1(b)) the initial errors as plotted at $t = 0$ are completely determined by the interpolation to the regular grid which sets the lower bound of the detectable signal. During the simulation this noise level is then overlaid with true non-zonal numerical truncation errors. These have a built-in wavenumber 5 structure which arises from the variations in the icosahedral grid intervals. The wavenumber 5 signal grows considerably over time due to the magnitude of the truncation errors and unstable mean state which leads to a visible breakdown of the zonal symmetry after several days. This effect is postponed at higher resolutions as the truncation error perturbations decrease.

Figure 4.2 shows the evolution of the zonal-mean zonal wind for the 30-day time period In general, the degradation of the zonal-mean is mainly attributable to the initial generation of gravity waves in the φ-η plane which slowly decay over time. They adjust the geostrophic balance in the discrete system since the analytically balanced initial state is not entirely balanced in a discrete representation. Both the EUL (Fig. 4.2(a)) and FV (Fig. 4.2(c)) dynamical cores modulate the zonal mean initially and exhibit flat profiles thereafter. There are only minor (FV) or almost no (EUL) improvements of the l_2 errors with increasing horizontal resolution. In contrast, the l_2 norms of the SLD dynamical core (Fig. 4.2(b)) increase linearly over the 30-day forecast period. As resolutions

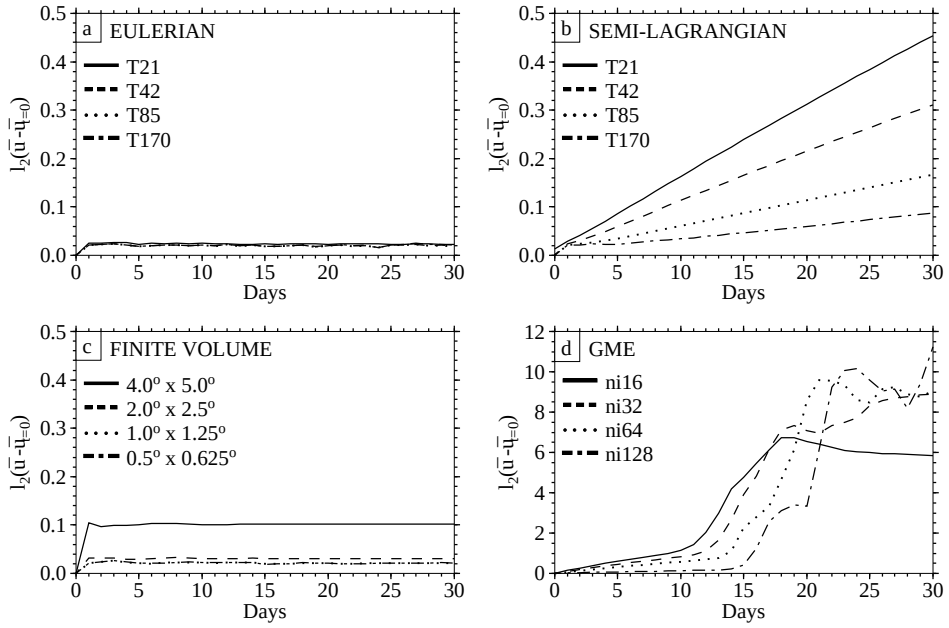

Figure 4.2: l_2 norm of $\bar{u} - \bar{u}_{t=0}$ in m s^{-1} for the four dynamical cores at varying horizontal resolutions and 26 levels.

increase and time steps decrease the zonal-mean is better maintained. This behavior is primarily determined by the decentering parameter ϵ, the length of the time step and the above mentioned meridional position of the non-zonal geodesic trajectory calculations in polar regions where the algorithm is switched from a spherical coordinate based scheme (Williamson and Rasch 1989). Note that the SLD curves closely match the EUL results (Fig. 4.2(a)) if the spherical coordinate based trajectory calculation is used everywhere and if the decentering parameter is set to zero. This is shown in Fig. 4.3(b). The former is, of course, only reasonable with zonal advection as in this case, and the latter in the absence of mountains. We deliberately do not include those variations in the tests here so as to evaluate the scheme as it would be applied in practice. Again, the GME errors arise from the built-in wavenumber 5 truncation errors which lead to the breakdown of the steady-state solution after several days (Fig. 4.2(d)). In general, such a model behavior is an artifact of the computational grid and the numerical method. But despite the clear exposure of this phenomenon it is somewhat artificial and unimportant unless one is trying to model a problem dominated by a zonal flow. For atmospheric applications this is clearly not the case since the forcing is strongly non-zonal. The wavenumber 5 effect is therefore overly enhanced by the idealized setup. Similar conclusion would also apply to models that utilize a cubed-sphere computational grid with a built-in wavenumber 4 structure.

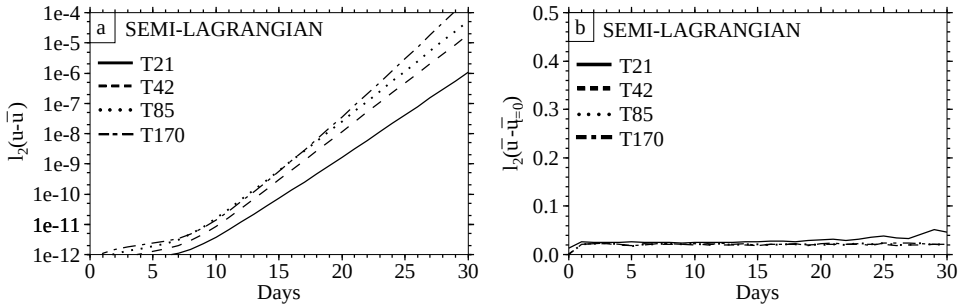

Figure 4.3: (a) l_2 norm of $u - \bar{u}$ and the (b) l_2 norm of $\bar{u} - \bar{u}_{t=0}$ in m s^{-1} for the semi-Lagrangian (SLD) dynamical core at varying horizontal resolutions and 26 levels. A pure spherical coordinate based trajectory calculation is used and the decentering parameter ϵ is set to zero.

Chapter 5

Results: Baroclinic wave test case

The baroclinic wave is triggered when overlaying the steady-state initial conditions with the zonal wind perturbation. As before, 30-day simulations at varying resolutions are performed with all four dynamical cores. In general, the nonlinear analytic solution for finite perturbations is not known. Therefore, we determine a set of reference solutions numerically by applying all the dynamical cores at very high horizontal resolutions. Because the basic state is unstable, small differences in addition to our imposed initial perturbation will also grow with time. In particular small differences between the initial discrete representations of the different cores will grow with time. Such differences can be introduced by different truncation errors between the schemes or between different resolutions of the same scheme, or even by different relative locations of the grid points with respect to the imposed perturbation for a given scheme. Thus the reference solutions differ from each other and the differences grow with time. These differences provide an estimate of the uncertainty in the reference solutions.

5.1 Time evolution

Figures 5.1–5.4 show snapshots of the evolving surface pressure and 850 hPa temperature fields[1] of the four dynamical cores at day 4, 6, 7, 8 and 10. All models are displayed at their second highest horizontal resolution with 26 levels which gives a first impression of the ensemble of reference solutions discussed in this report. Note that the corresponding snapshots at day 9 are presented in Section 5.2 (Figs. 5.5–5.8). In general, the baroclinic wave grows very slowly until day 4. At day 6 the surface pressure shows two weak high and low pressure systems (Figs. 5.1(b)–5.4(b)) and two small-amplitude waves are visible in the temperature field (Figs. 5.1(g)–5.4(g)). At day 7 the rapid development stage of the baroclinic instability sets in (note the change in the scale). The two high and low pressure centers have intensified and the temperature wave can now clearly be seen. By day 8 the highs and lows have deepened significantly (Figs. 5.1(d)–5.4(d)). In addition, the two waves in the temperature field have almost peaked and are beginning to wrap around with fronts trailing from them. A third upstream wave is now visible. At day 10 wave breaking has set in. Three closed cells with relatively warmer temperatures (Figs. 5.1(j)–5.4(j)) have formed with the leading front quite sharp.

[1] The 850 hPa temperature field is computed via a linear interpolation in $\ln p$ coordinates using the two surrounding model levels.

In comparison, the growth characteristics of the baroclinic disturbances in all four models are visually very similar. Differences can only be seen at very small scales as expected. Note that the intensification of the baroclinic wave in the Finite Volume (FV) dynamical core (Fig. 5.3) appears to be slightly weaker than in EUL, SLD and GME. This is due to the intrinsic nonlinear diffusion of the numerical scheme, which is further discussed in Section 5.2 and 5.3. In addition, both the Eulerian (EUL) and semi-Langrangian (SLD) dynamical cores show some spectral noise in the surface pressure fields at day 8 and 10. Such a behavior is most commonly observed for spectral numerical techniques with low diffusion.

5.2 Convergence and model comparison

Figures 5.5–5.8 compare the surface pressure and 850 hPa temperature fields of all four dynamical at day 9 for the range of horizontal resolutions considered here (see Section 3.5). In the vertical direction 26 model levels were used. It can clearly be seen that the two lowermost horizontal resolutions of all four models do not capture the strength of the closed cells in the surface pressure fields. In addition, the fronts in the temperature fields are not as sharp as in the higher resolution model runs. However, the mid-range resolutions T85, $1^\circ \times 1.25^\circ$ and ni64 (Figs. 5.5(c)–5.8(c)) are visually very similar to the simulations at the higher resolutions although the closed cells in the surface pressure at 170°E are not quite as deep. As an aside, these mid-range resolutions or even coarser resolutions (around T42) are typically used for climate simulations today. Note that the GME simulations at ni64 and the lower resolutions (Figs. 5.8(a-c)) are characterized by an apparent phase lag in comparison to the higher resolution runs. This is further analyzed in Section 5.5.3. The second-highest and highest resolution runs are visually almost indistinguishable. Differences can only be seen at the smallest scales that are most influenced by the diffusive characteristics of the numerical schemes. An example are the closed cells in the surface pressure fields of the Eulerian, semi-Lagrangian and GME solutions. They are slightly deeper than those from the Finite Volume dynamical core. The two spectral cores also exhibit spectral noise where the fields become nearly flat.

Figures 5.9–5.12 display the 850 hPa relative vorticity fields of the four dynamical cores at day 7 and 9. As before, the models are shown with increasing horizontal resolution and 26 levels. In these plots, the overall vorticity patterns of all dynamical cores agree reasonably well at the second highest and highest horizontal resolutions despite the fact that the small-scale differences of the vorticity grow more rapidly. Therefore, the differences among the models become more evident in comparison to Figs. 5.5–5.8. At day 7, the high-resolution Finite Volume (FV) dynamical core (Figs. 5.11(d) and (e)) exhibits a slightly weaker vorticity pattern in comparison to EUL, SLD and GME at high resolutions. The latter are visually very similar and almost identical at the second highest and highest resolution. The slightly weaker vorticity fields are caused by the monotonicity constraint in the FV dynamical core. This constraint adds nonlinear intrinsic diffusion in the regions where the monotonocity principles are locally violated. Note that the slightly more diffusive solution of the FV dynamical core can be matched more very closely by EUL and SLD when increasing their diffusion coefficients (see Section 5.3). At day 9 the waves have almost reached their breaking point. Here, the details of vorticity patterns differ, especially in the vicinity of the rolled up tongues of the vortices. Again, the EUL and SLD dynamical cores (Figs. 5.9 and 5.10) show spectral noise that disrupts the vorticity contours. In general, it can be seen that the vorticity

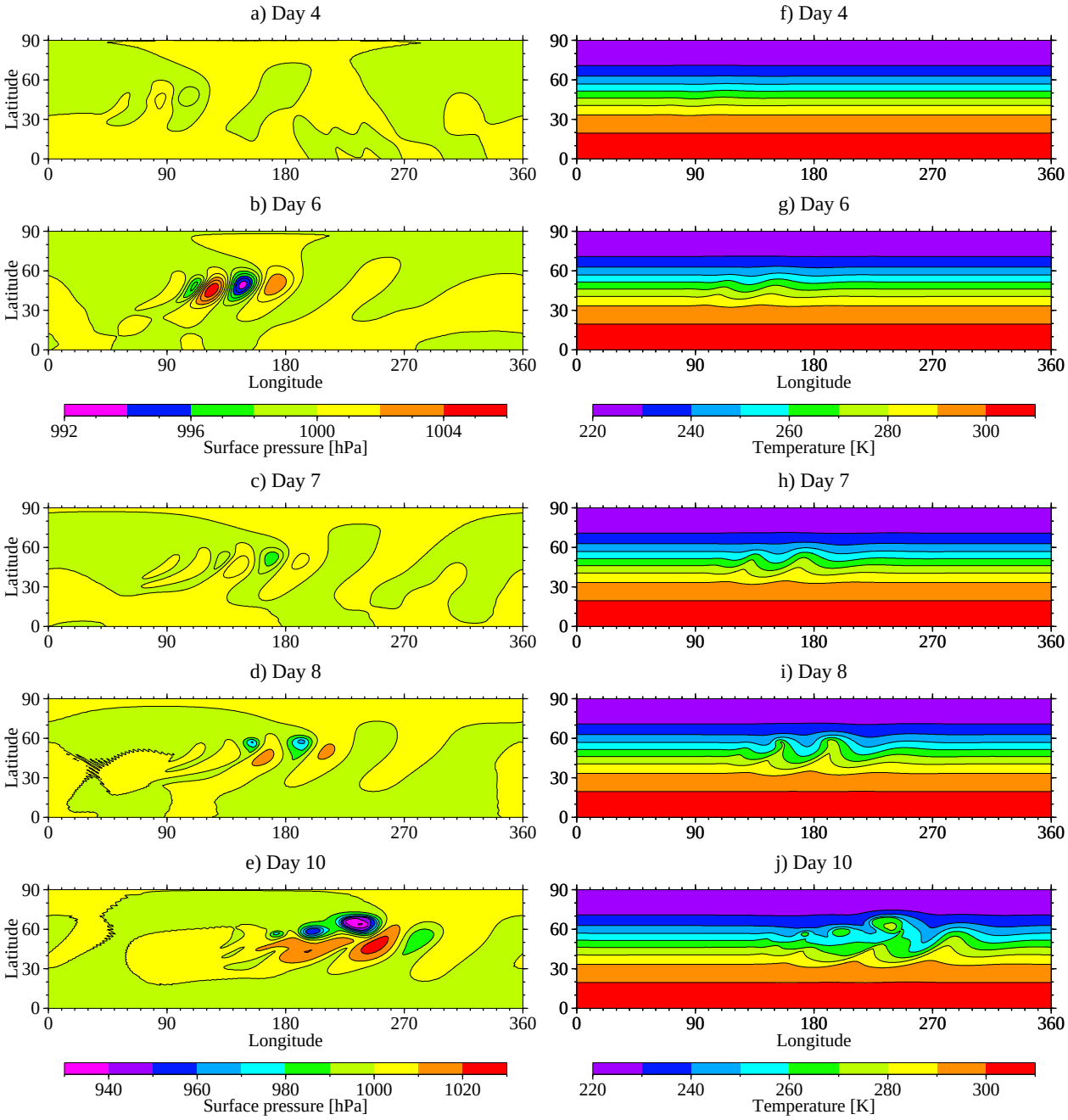

Figure 5.1: Evolution of the baroclinic wave from day 4 until day 10: Surface pressure (left column) and temperature at 850 hPa (right column) modeled with the Eulerian (EUL) dynamical core at the horizontal resolution T170 and 26 levels.

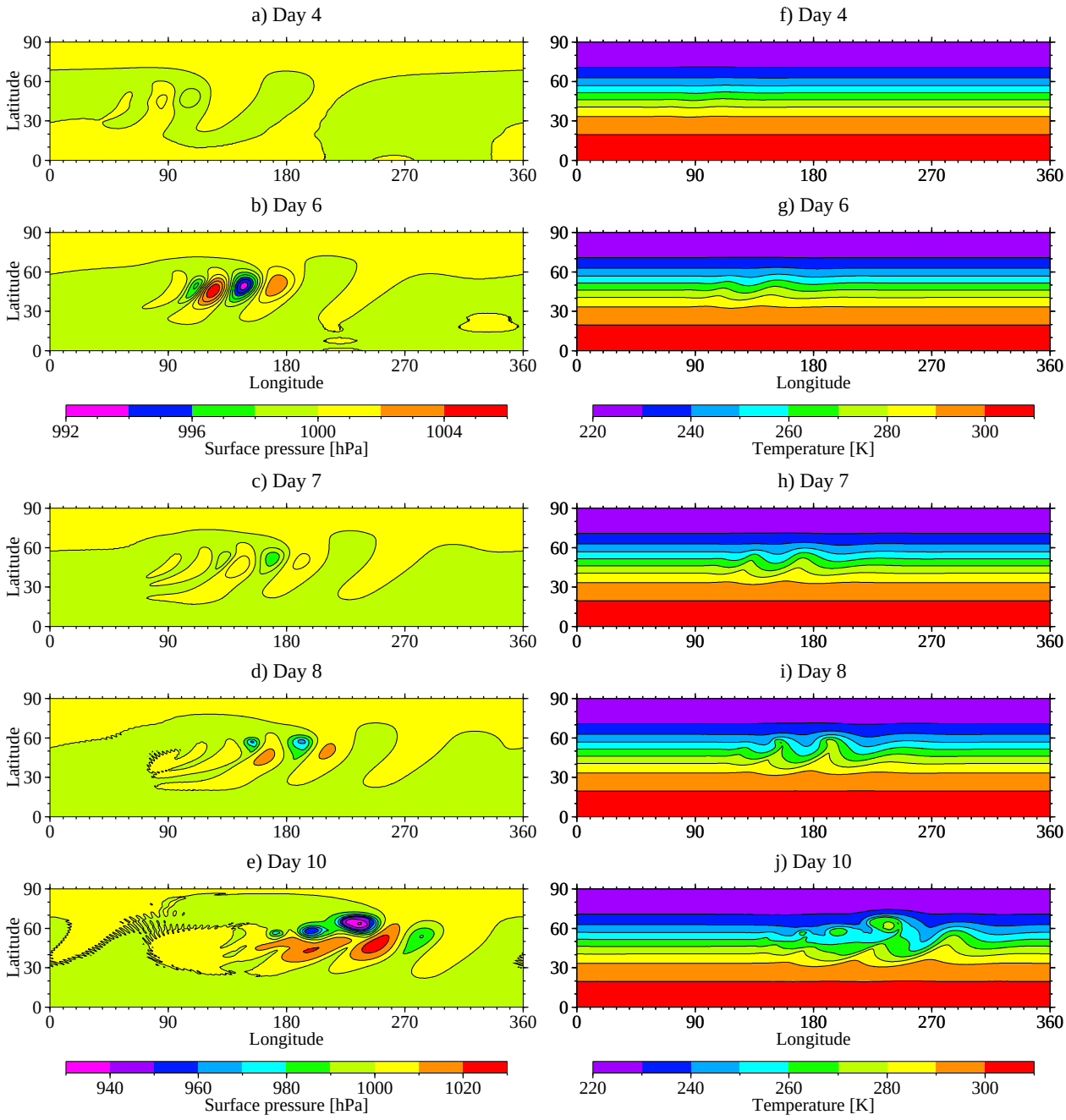

Figure 5.2: Same as Fig. 5.1 but for the semi-Lagrangian (SLD) dynamical core at the horizontal resolution T170 and 26 levels.

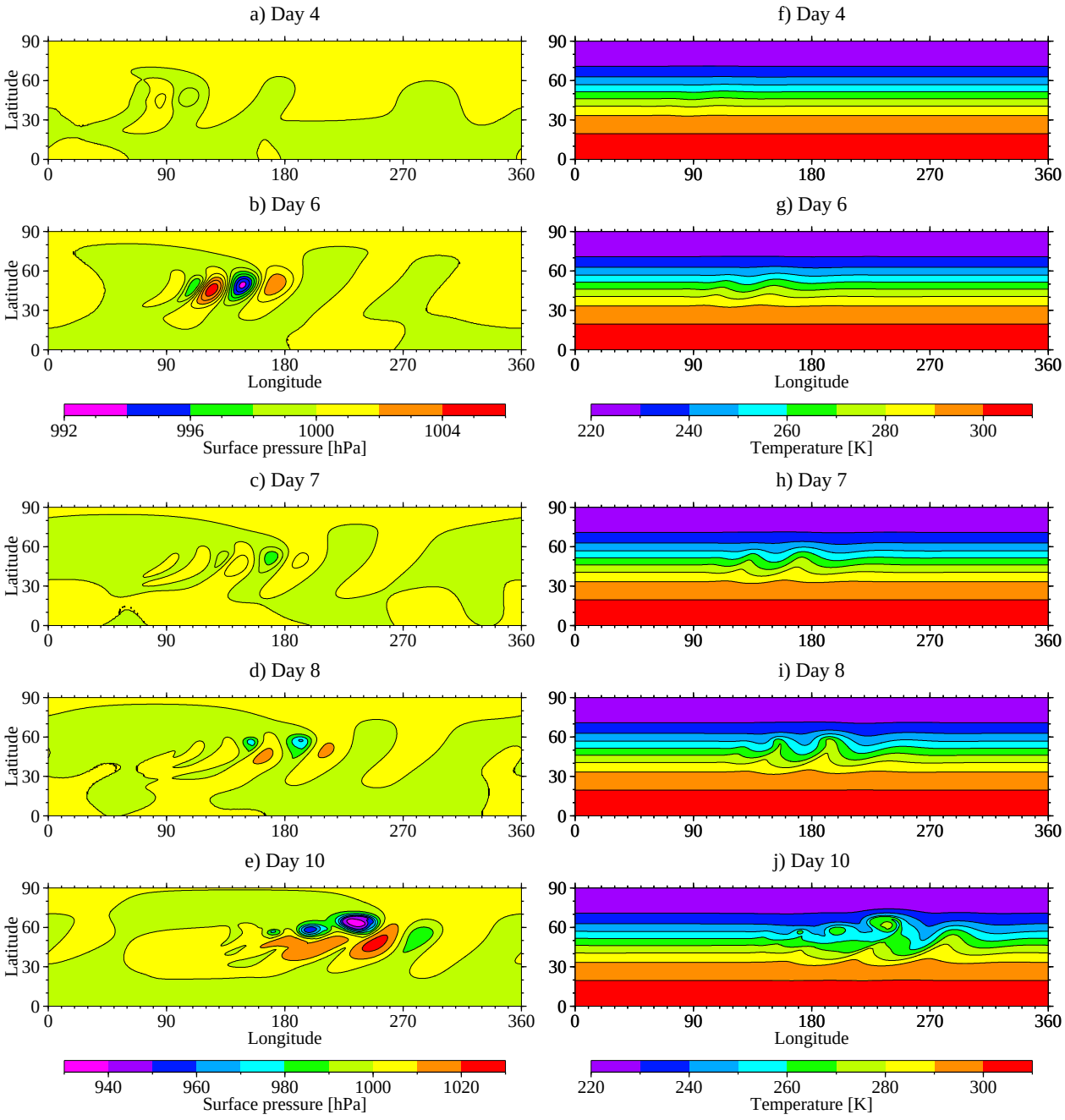

Figure 5.3: Same as Fig. 5.1 but for the Finite Volume (FV) dynamical core at the horizontal resolution $0.5^\circ \times 0.625^\circ$ and 26 levels.

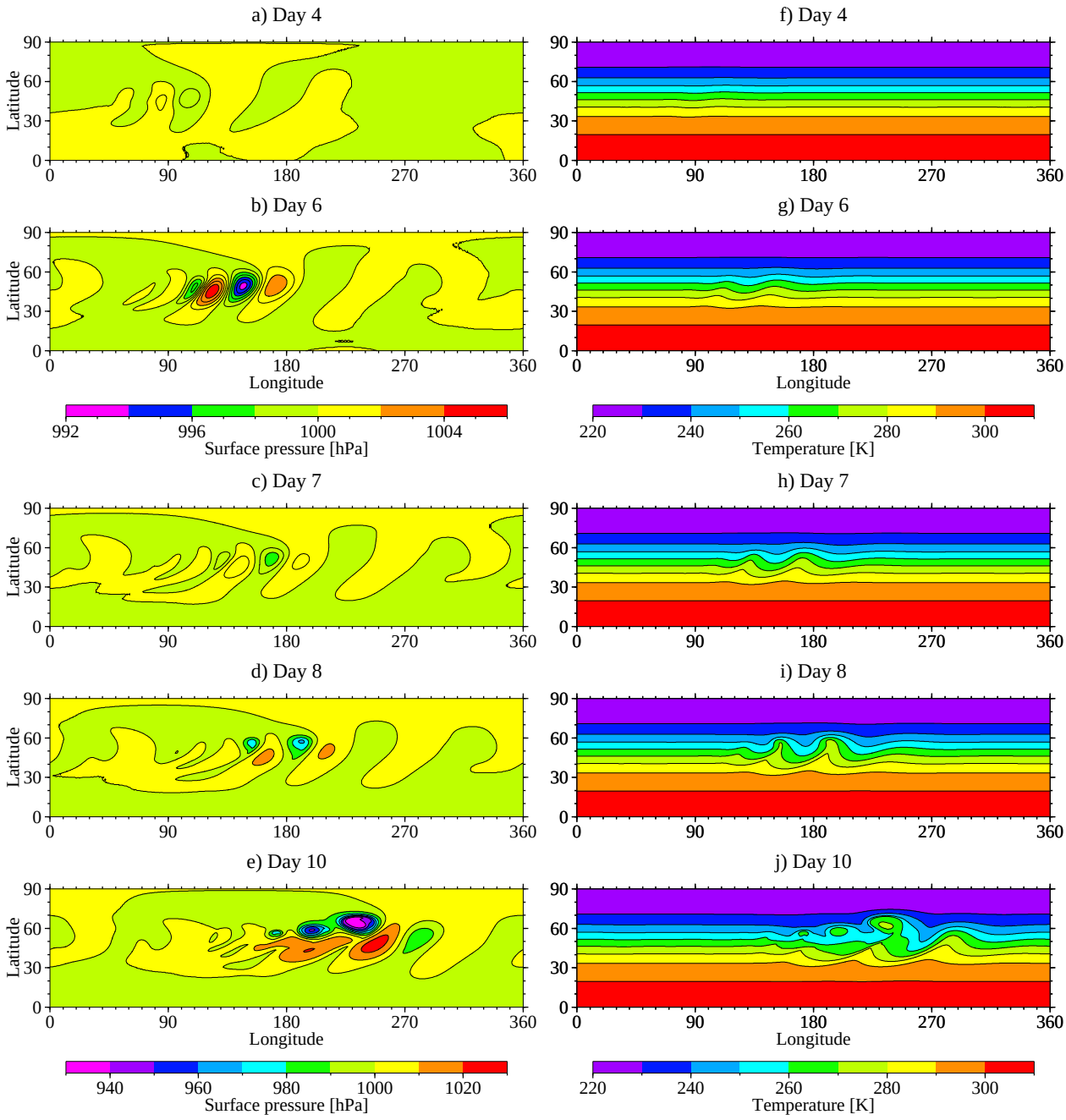

Figure 5.4: Same as Fig. 5.1 but for the dynamical core of GME at the horizontal resolution $ni128$ and 26 levels.

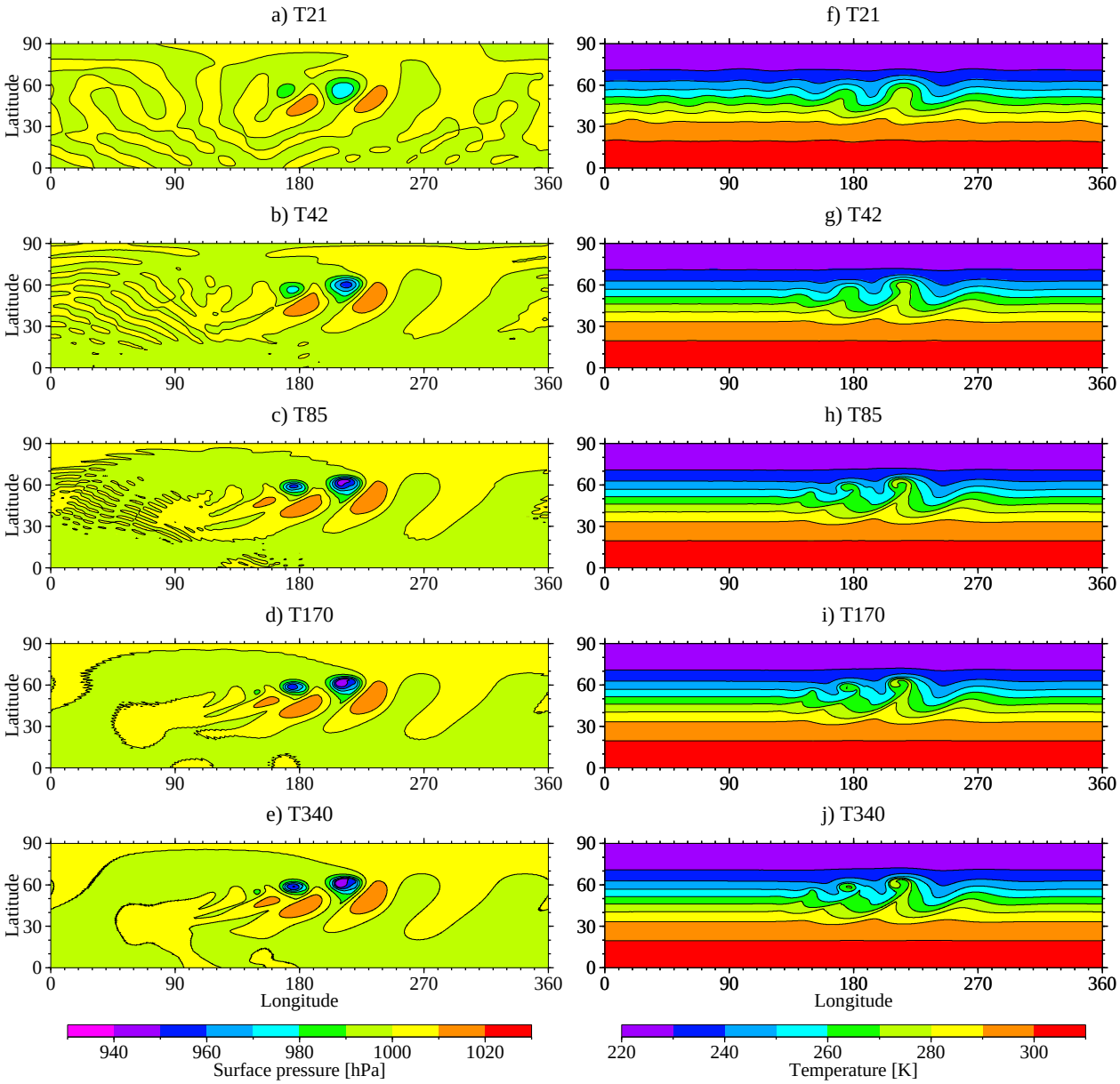

Figure 5.5: Convergence of the Eulerian (EUL) dynamical core with increasing horizontal resolution and 26 levels. The snapshots show the surface pressure (left column) and temperature at 850 hPa (right column) at day 9.

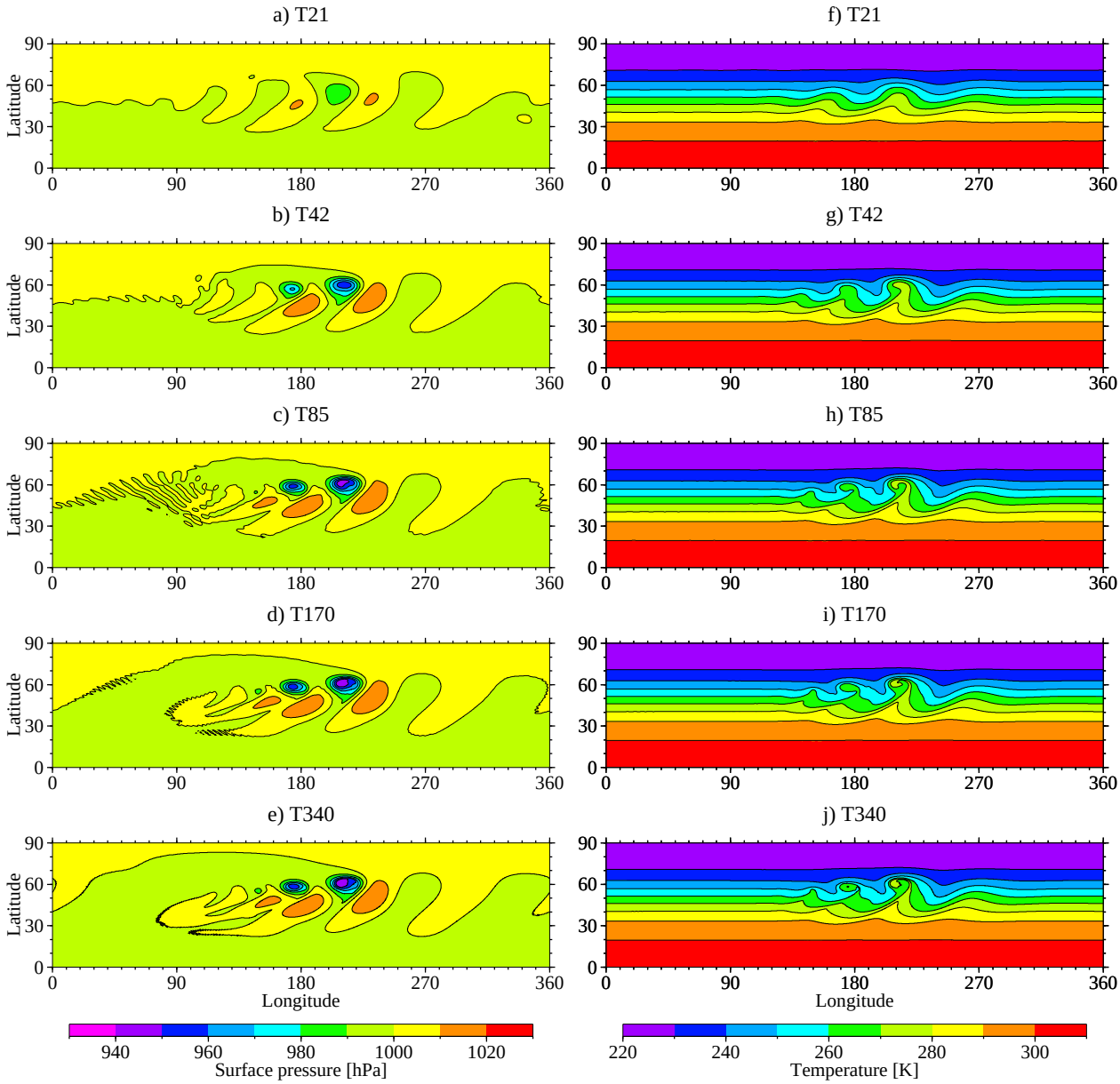

Figure 5.6: Same as Fig. 5.5 but for the semi-Lagrangian (SLD) dynamical core with increasing horizontal resolution and 26 levels (day 9).

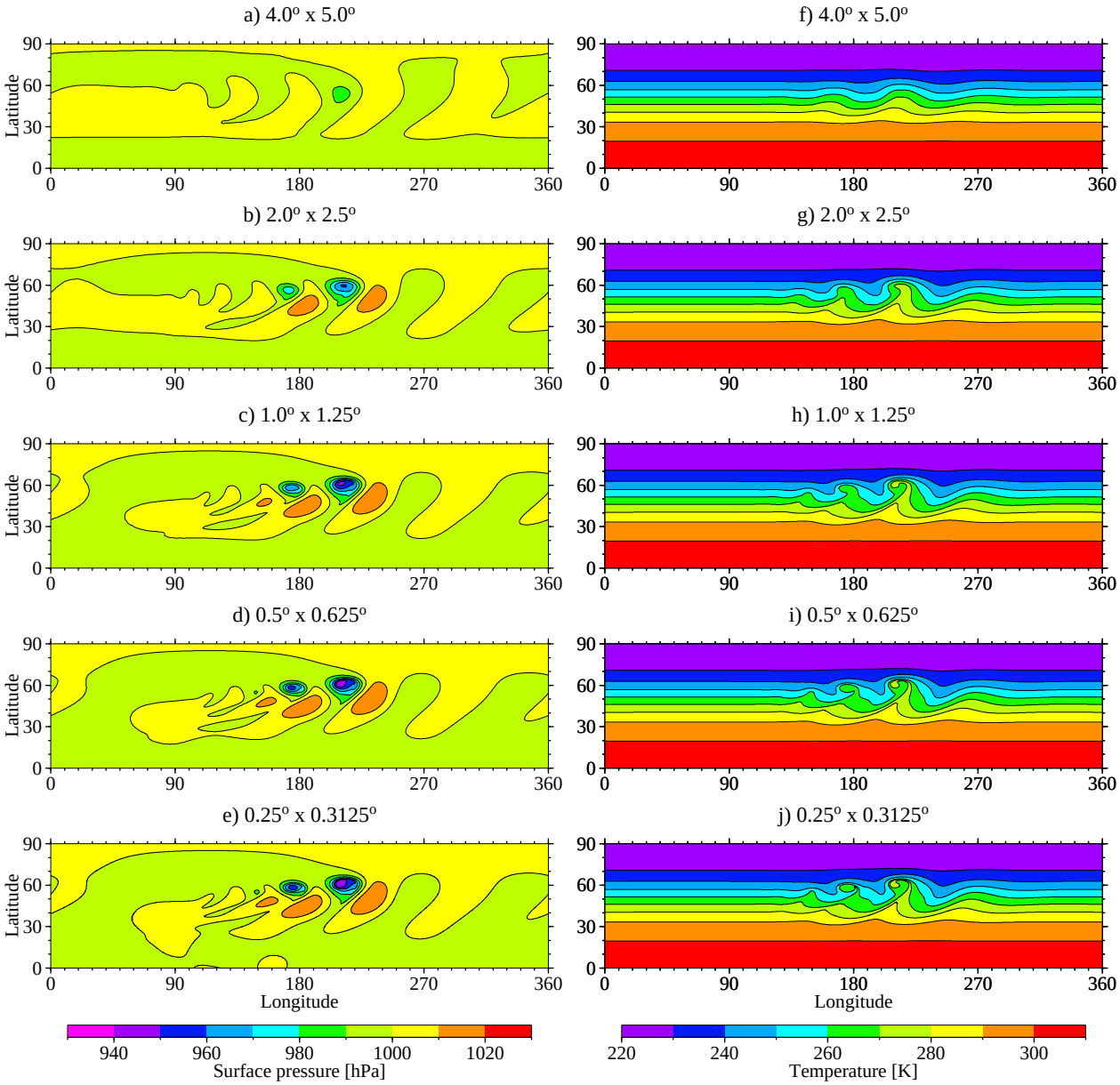

Figure 5.7: Same as Fig. 5.5 but for the Finite Volume (FV) dynamical core with increasing horizontal resolution and 26 levels (day 9).

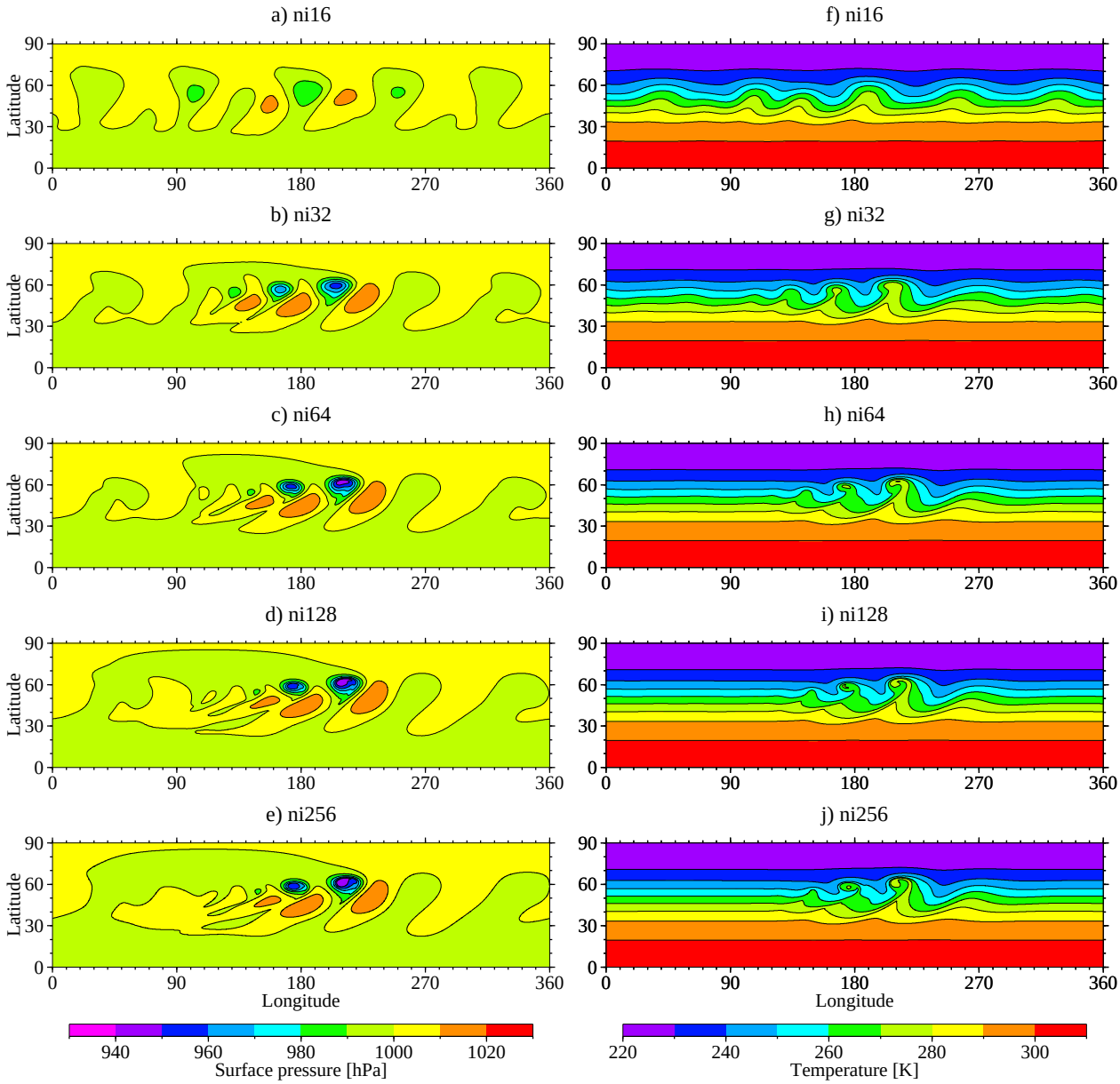

Figure 5.8: Same as Fig. 5.5 but for the dynamical core of GME with increasing horizontal resolution and 26 levels (day 9).

gradients become extremely sharp after day 7 since we purposely do not apply strong diffusion mechanisms as in POL. This enables us to assess the uncertainties in the high-resolution reference solutions for models in their operational configurations (see discussion in Section 5.5).

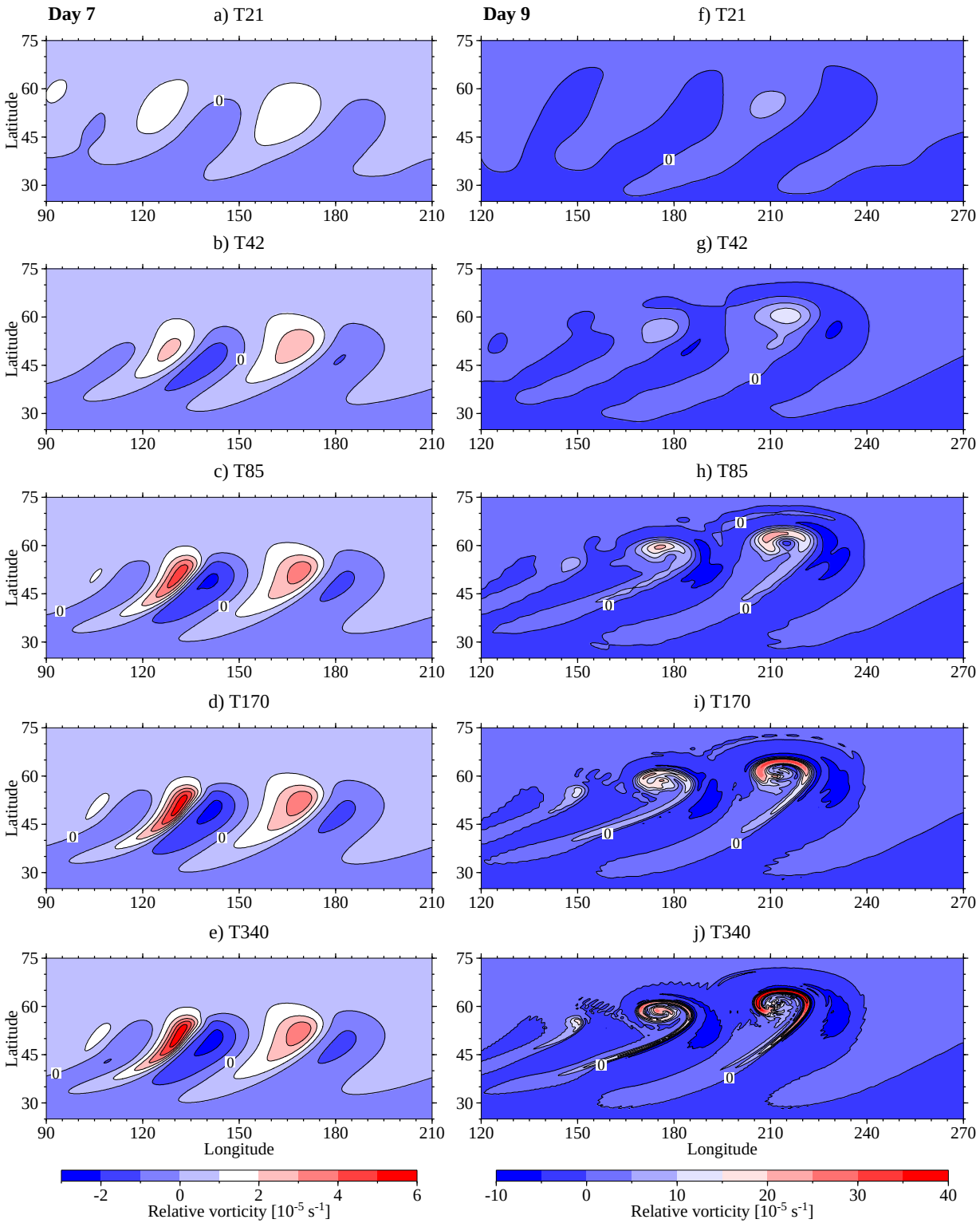

Figure 5.9: Convergence of the Eulerian (EUL) dynamical core with increasing horizontal resolution and 26 levels. The snapshots show the 850 hPa relative vorticity fields at day 7 (left column) and day 9 (right column).

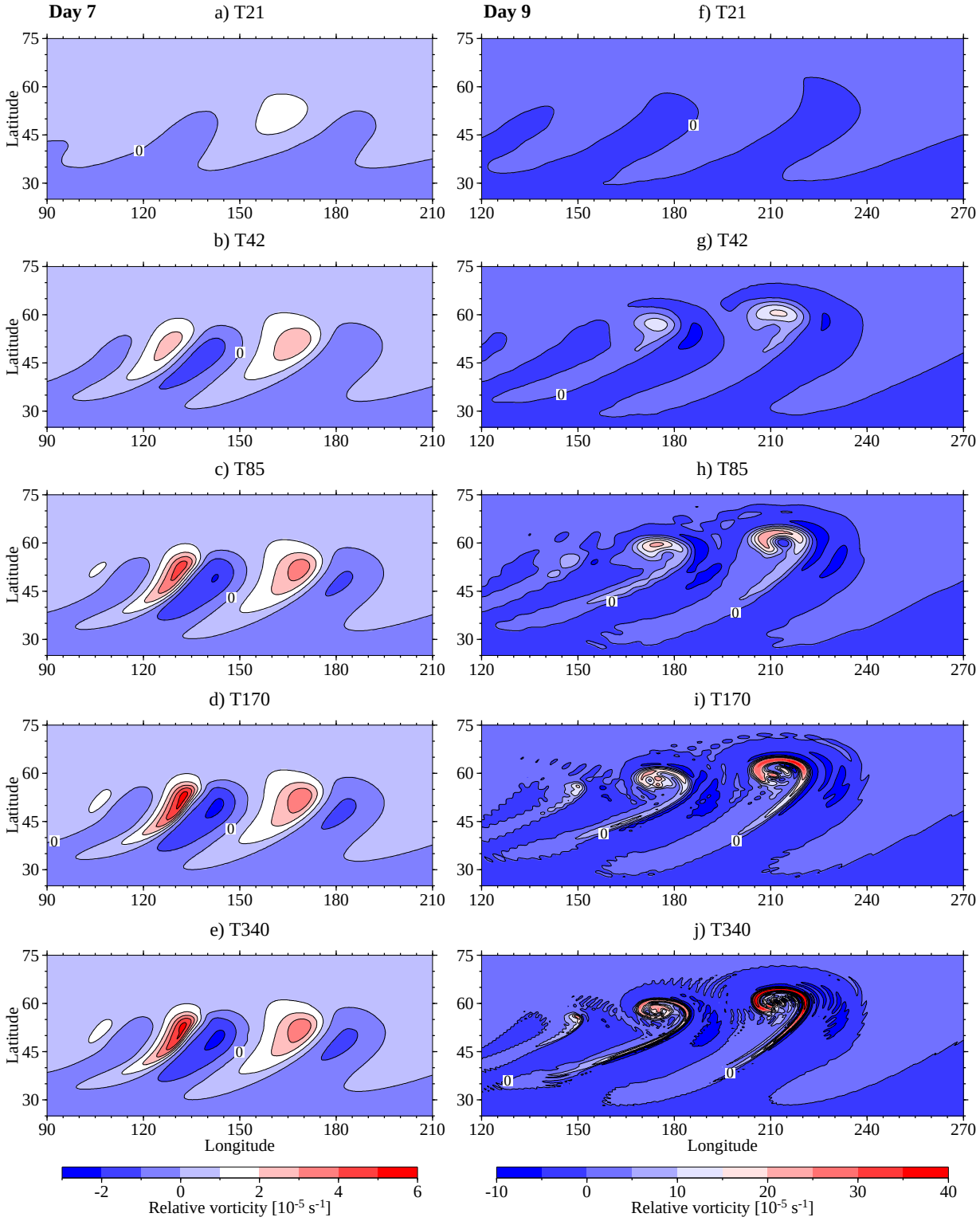

Figure 5.10: Same as Fig. 5.9 but for the semi-Lagrangian (SLD) dynamical core with increasing horizontal resolution and 26 levels.

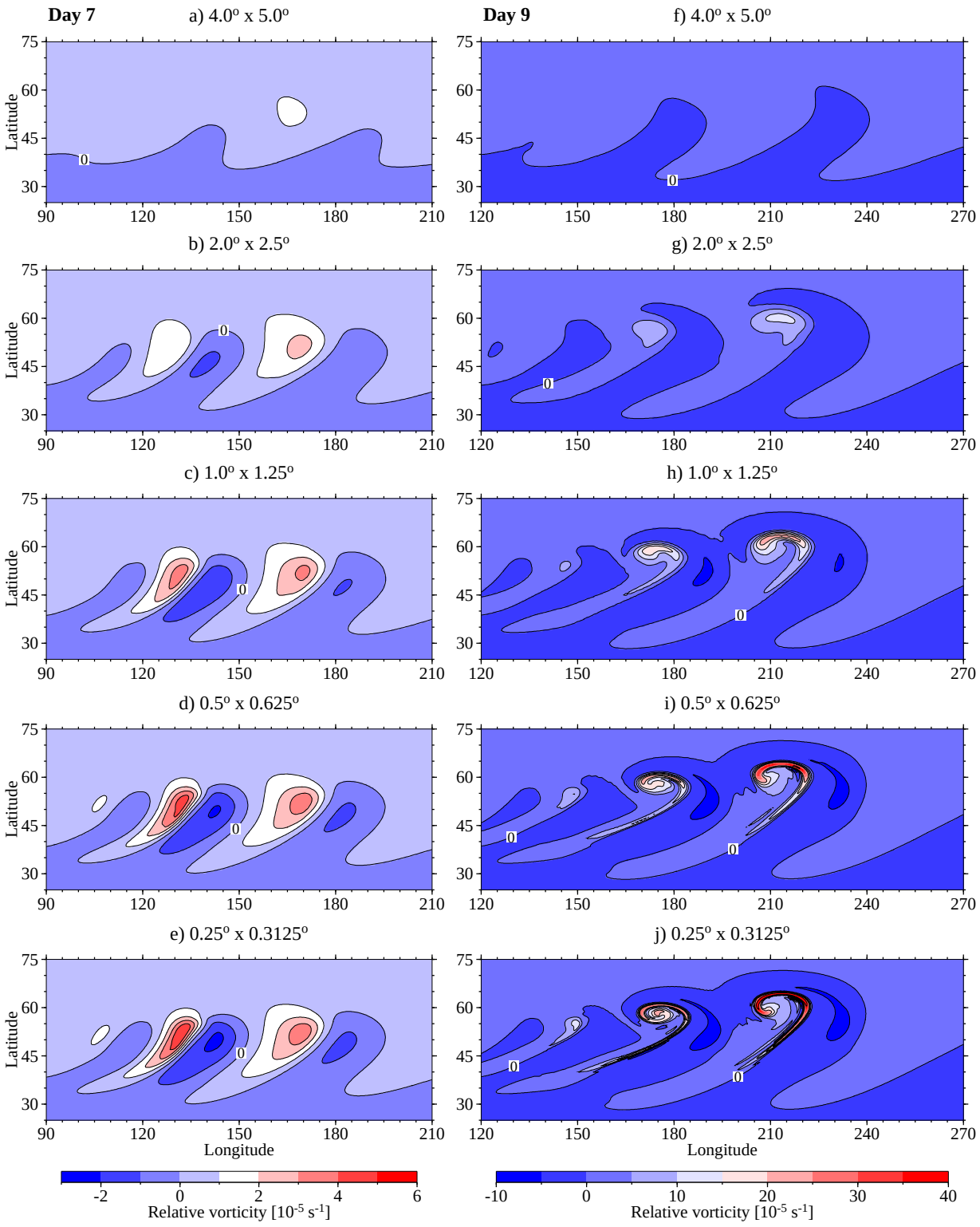

Figure 5.11: Same as Fig. 5.9 but for the Finite Volume (FV) dynamical core with increasing horizontal resolution and 26 levels.

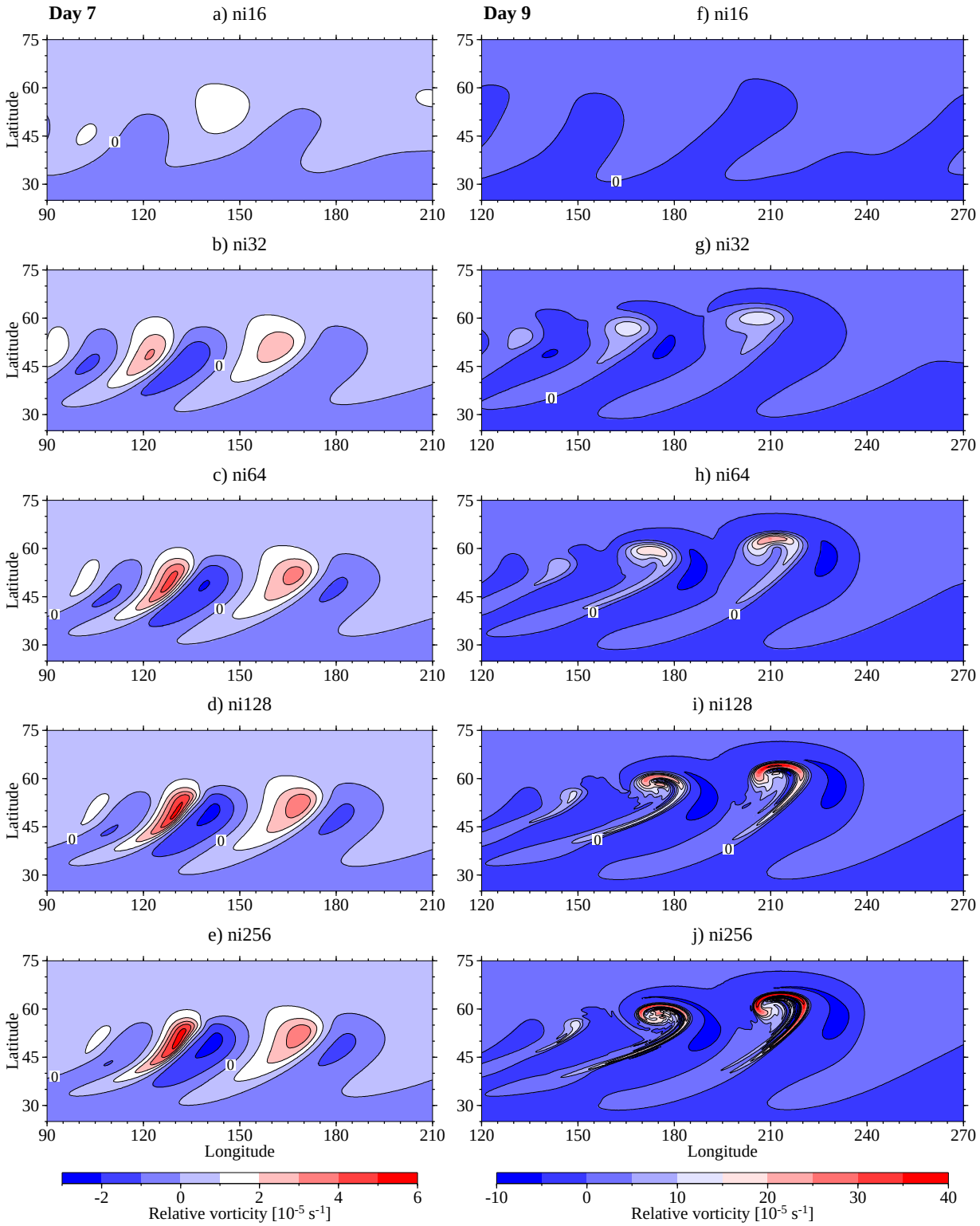

Figure 5.12: Same as Fig. 5.9 but for the dynamical core of GME with increasing horizontal resolution and 26 levels.

5.3 Sensitivity to the diffusion coefficient

For the dynamical core intercomparison presented in this report, all models are run in their typical configurations that would also be used for climate predictions or NWP applications. On purpose, no attempt has been made to tune the models towards a forced converged state. This especially addresses the choice of the diffusion coefficients in the EUL, SLD and GME dynamical cores (Tables 3.1 and 3.3). Note that the numerical scheme of the FV dynamical core exhibits intrinsic nonlinear numerical diffusion that is not tunable by a diffusion coefficient. It is also important to point out that an artificial exact numerical convergence of the models can be forced by adding extreme diffusion (POL). But this essentially inhibits the interesting small-scale features of the solution and, as a consequence, leads to a very different evolution of the baroclinic wave. Therefore, we are not interested in such diffusive simulations.

In order to put the different diffusive characteristics of the models into perspective, a short sensitivity study has been performed. In particular, the sensitivities of the EUL and SLD dynamical cores to moderate increases in the forth-order diffusion coefficient K_4 are assessed. The second-order diffusion coefficient K_2, that is only active in a few model levels near the model top, is left at its standard value $K_2 = 2.5 \times 10^5$ m^2 s^{-1}. Here, the study focuses on the horizontal resolutions T85 and T170 with 26 vertical levels.

Figures 5.13 and 5.14 show the surface pressure, 850 hPa temperature and relative vorticity fields of the EUL simulation with doubled K_4 diffusion coefficients at T85 and T170. Model days 7 (Fig. 5.14) and 9 (Figs. 5.13 and 5.14) are shown that can be compared to the Eulerian model simulations with the standard K_4 setting (Figs. 5.5 and 5.9). Here it can be seen that the additional diffusion helps smooth the spectral noise, but on the other hand leads to a slight weakening of the EUL 850 hPa vorticity field. The latter now resembles the corresponding FV vorticity fields (Fig. 5.11) more closely.

An even clearer demonstration of the impact of the diffusion on the numerical simulation is given in Fig. 5.15. Again, the surface pressure, 850 hPa temperature and relative vorticity fields of the EUL dynamical core at T85 are shown, but now the standard K_4 diffusion coefficient is increased by a factor of 10. In this setup, the spectral noise is eliminated but the diffusion has strong detrimental effects on the overall circulation. This can now be seen in all model fields which show a severely damped evolution of the baroclinic disturbance. Here, the strong gradients and small-scale features of the solution are smoothed out which slows down the rapid growth of the baroclinic wave.

In addition, the sensitivity of the SLD dynamical core to the diffusion coefficients is assessed. Recall, that we did not include any second- or forth-order diffusion in our standard experiments since the smallest scales are mainly controlled by the intrinsic diffusion of the interpolations in the semi-Lagrangian numerical scheme. Nevertheless, the intrinsic diffusion still allowed some spectral noise in the SLD simulations as seen in Figs. 5.7 and 5.11. Therefore, it is interesting to assess the impact of some minor additional diffusion on the SLD model simulation. Here, we evaluate the effects of the standard Eulerian diffusion coefficients (Table 3.1) on the SLD dynamical core at T85 and T170 with 26 model levels. Figures 5.16 and 5.17 show the surface pressure, 850 hPa temperature and relative vorticity fields of the corresponding SLD simulation at model day 7 and 9, respectively. These figures can be compared to the inviscid SLD model simulations in Figs. 5.6 and 5.10. As already seen in the EUL model runs with doubled K_4 diffusion (Figs. 5.13 and 5.14) the additional diffusion helps smooth the spectral noise in the SLD simulation, but on the other hand

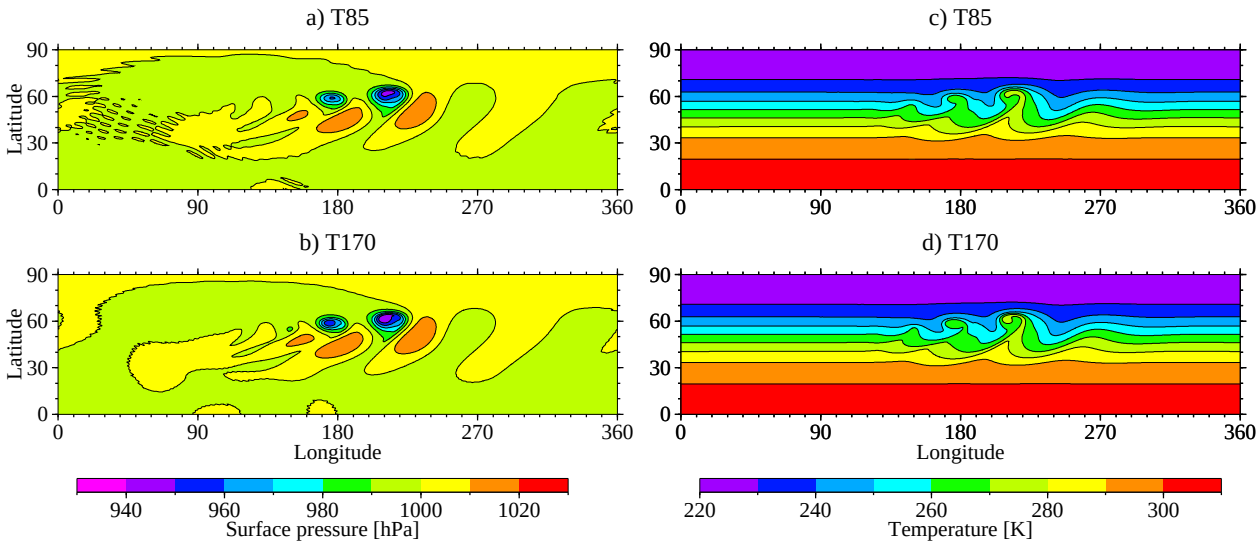

Figure 5.13: Sensitivity of the Eulerian (EUL) dynamical core to the doubling of the standard horizontal diffusion coefficient K_4 at the resolutions T85 and T170 with 26 vertical levels (compare to Fig. 5.5). $K_4 = 2.0 \times 10^{15}$ m^4 s^{-1} (T85) and $K_4 = 3.0 \times 10^{14}$ m^4 s^{-1} (T170) are used. K_2 is standard (Table 3.1). The snapshots show the surface pressure (left column) and temperature at 850 hPa (right column) at day 9.

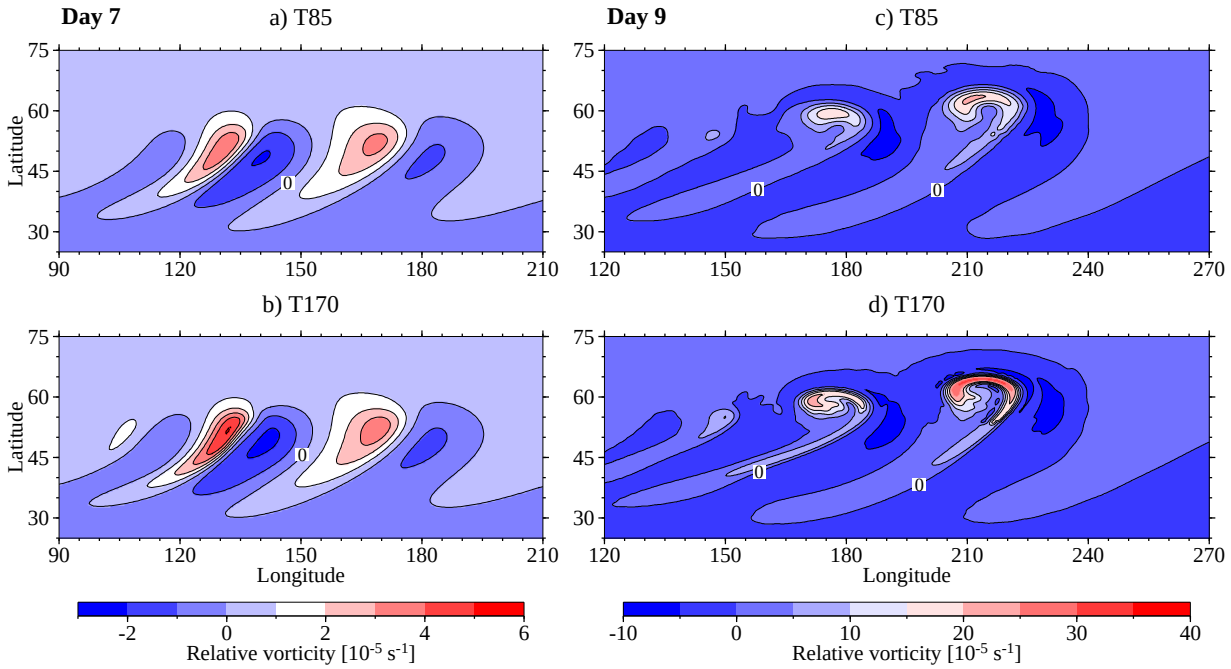

Figure 5.14: Sensitivity of the Eulerian (EUL) dynamical core to the doubling of the standard horizontal diffusion coefficient K_4 at the resolutions T85 and T170 with 26 vertical levels (compare to Fig. 5.9). $K_4 = 2.0 \times 10^{15}$ m^4 s^{-1} (T85) and $K_4 = 3.0 \times 10^{14}$ m^4 s^{-1} (T170) are used. K_2 is standard (Table 3.1) The snapshots show the 850 hPa relative vorticity field at day 7 (left column) and day 9 (right column).

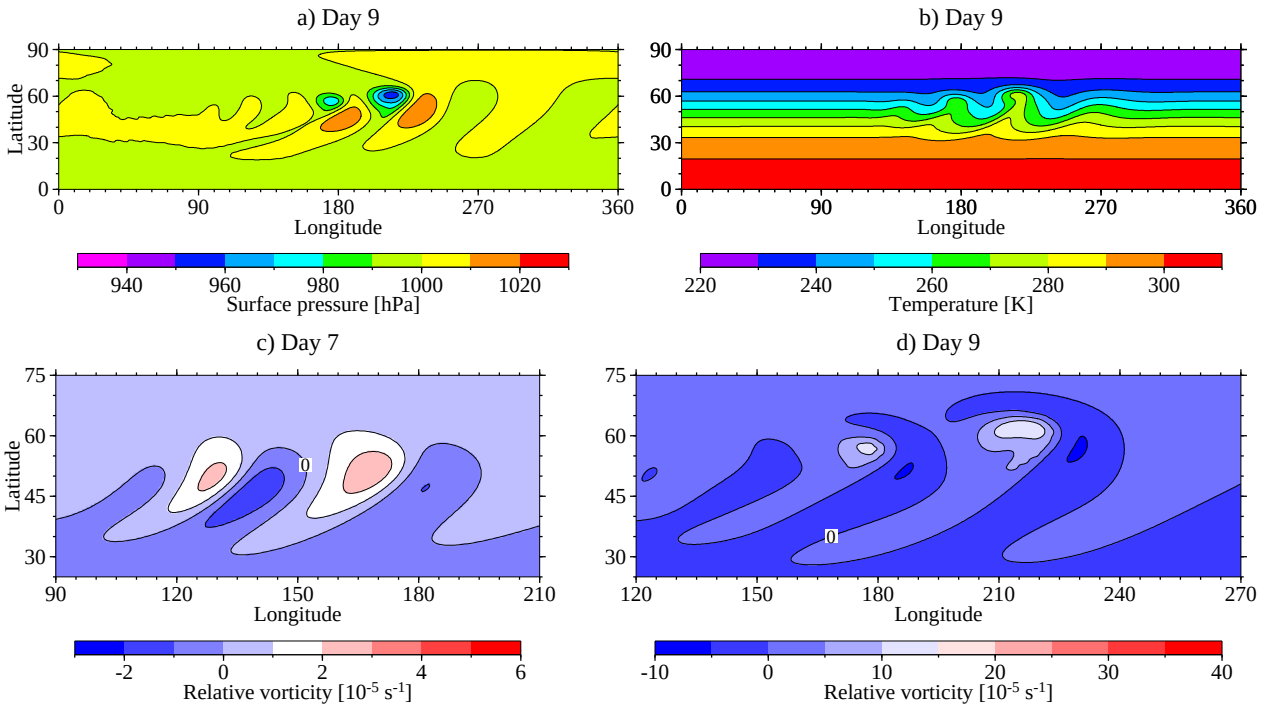

Figure 5.15: Sensitivity of the Eulerian (EUL) dynamical core at the resolution T85L26 to an increase in the horizontal diffusion coefficient K_4 by a factor of 10. $K_4 = 1.0 \times 10^{16}$ m^4 s^{-1} is used, K_2 is standard (Table 3.1). The snapshots show (a) the surface pressure, (b) the 850 hPa temperature and (c–d) the 850 hPa relative vorticity at day 7 and 9, respectively.

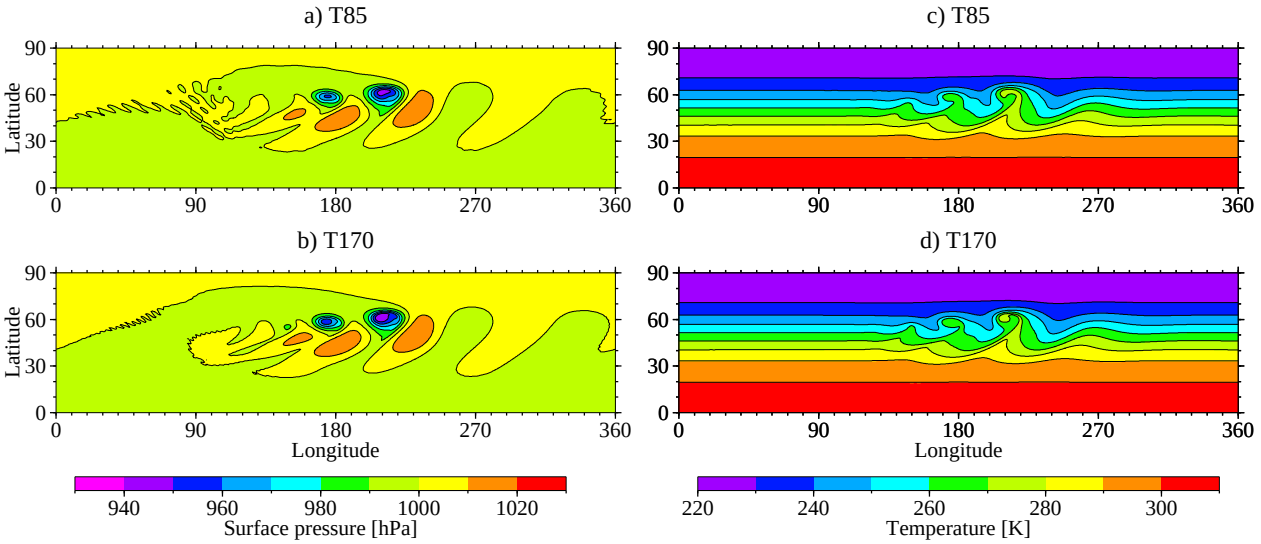

Figure 5.16: Sensitivity of the semi-Lagrangian (SLD) dynamical core to the horizontal diffusion coefficients K_4 and K_2 at the resolutions T85 and T170 with 26 vertical levels (compare to Fig. 5.6). $K_4 = 1.0 \times 10^{15}$ m^4 s^{-1} (T85), $K_4 = 1.5 \times 10^{14}$ m^4 s^{-1} (T170) and $K_2 = 2.5 \times 10^5$ m^2 s^{-1} are used that are standard for the EUL dynamical core (see Table 3.1). The snapshots show the surface pressure (left column) and temperature at 850 hPa (right column) at day 9.

also leads to a slight weakening of the SLD 850 hPa vorticity field. The latter now also resembles the corresponding FV vorticity fields (Fig. 5.11) more closely, especially at day 7.

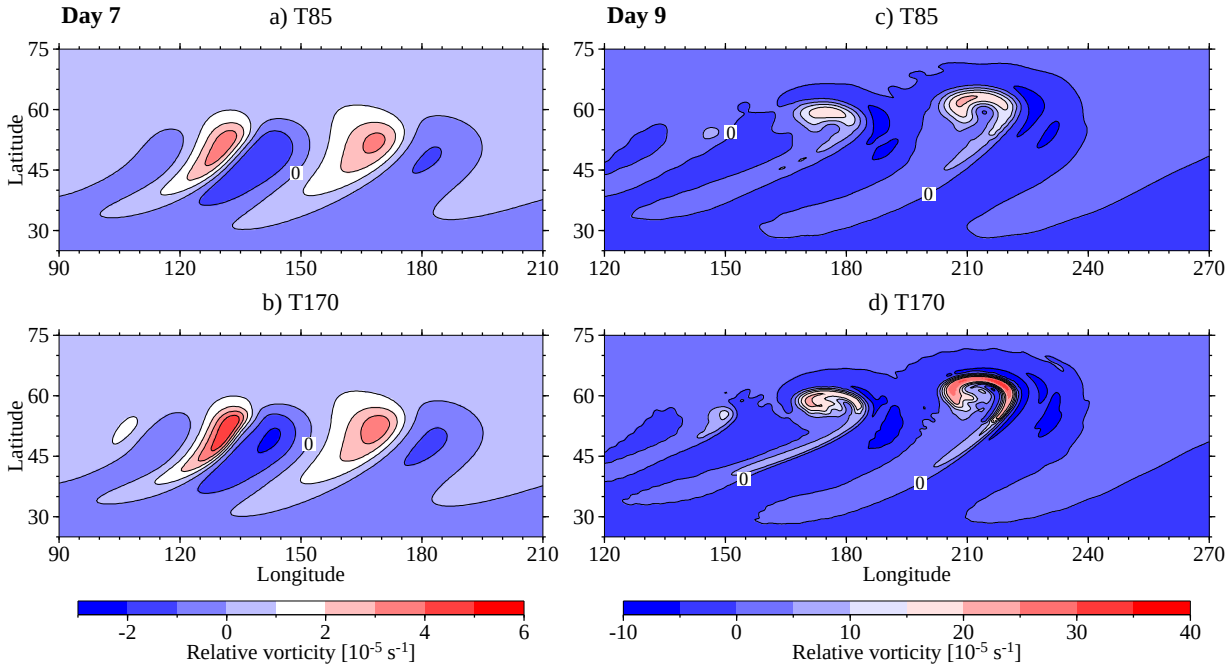

Figure 5.17: Sensitivity of the semi-Lagrangian (SLD) dynamical core to the horizontal diffusion coefficients K_4 and K_2 at the resolutions T85 and T170 with 26 vertical levels (compare to Fig. 5.10). $K_4 = 1.0 \times 10^{15}$ m^4 s^{-1} (T85), $K_4 = 1.5 \times 10^{14}$ m^4 s^{-1} (T170) and $K_2 = 2.5 \times 10^5$ m^2 s^{-1} are used that are standard for the EUL dynamical core (see Table 3.1). The snapshots show the 850 hPa relative vorticity field at day 7 (left column) and day 9 (right column).

5.4 Forecast skills after model day 10

In this report, the discussion of the baroclinic wave test is focused on the first 10 model days although integrations until day 30 have been performed. In general, it can be observed that the solutions of the four dynamical cores start diverging from each other after wave-breaking events set in around day 9. In particular, the differences in the solutions after day 10 become evident in the regions where the baroclinic waves have reached maturity and generated sharp fronts. Nevertheless, in other regions the forecasts after day 10 are still reliable. This is especially true for the newly developing systems downstream of the baroclinic wave. In these regions the initial development is in essence a linear phenomenon. As shown in Fig. 5.18 new systems develop every 2-3 days 60-90° downstream of the leading edge of the wave train. The figure depicts the surface pressure maps of the four dynamical cores at the second-highest resolution at day 11, 14 and 16 in a northpolar-stereographic projection. The high pressure centers are marked with the symbol '+'. The evolution of the new downstream systems agrees well across the four model simulations even until day 16. This is in particular true for the EUL, SLD and FV model runs whereas the GME simulation is noticeably perturbed by the growing wavenumber 5 from day 14 onwards (compare to Section 4). Such a succession of new systems downstream of a baroclinic wave is also discussed in Simmons and Hoskins (1979).

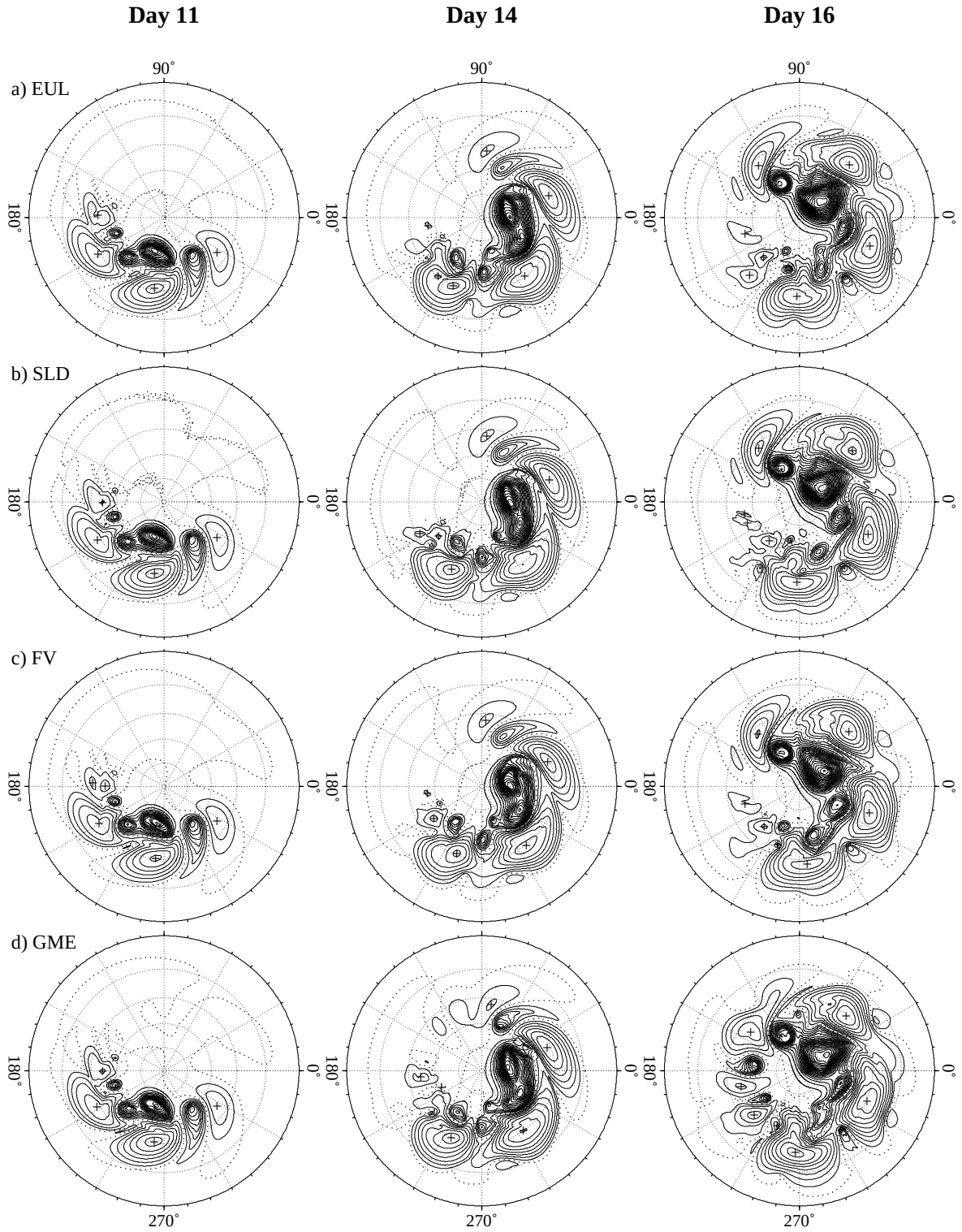

Figure 5.18: Northpolar-stereographic projection of the surface pressure at day 11 (left), day 14 (middle) and day 16 (right) for the four dynamical cores at their second-highest resolution (a) EUL T170, (b) SLD T170, (c) FV $0.5^\circ \times 0.625^\circ$ and (d) GME ni128 with 26 levels. The contour interval is 5 hPa, the 1000 hPa contour line is dotted. The high pressure centers are labeled with the symbol '+'.

5.5 Difference norms

In this section we quantify the differences between solutions from different dynamical cores and at different resolutions using the l_1, l_2 and l_∞ difference norms of the surface pressure, 850mb temperature and 850mb vorticity. Surface pressure is most convenient for general comparisons since the norms can be calculated without vertical interpolation to a specified pressure surface. Also it does not require the calculation of a secondary variable such as vorticity which is not a prognostic variable for many dynamical cores. We present all three variables here to demonstrate that consideration of surface pressure alone is adequate for future comparisons.

The difference norms for p_s are defined by

$$\begin{aligned} l_1\big(p_s(t)\big) &= \frac{1}{4\pi} \int_0^{2\pi} \int_{-\frac{\pi}{2}}^{\frac{\pi}{2}} |p_{s_1}(\lambda,\varphi,t) - p_{s_2}(\lambda,\varphi,t)| \, \cos\varphi \, d\varphi \, d\lambda \\ &\approx \frac{\sum_i \sum_j |p_{s_1}(\lambda_i,\varphi_j,t) - p_{s_2}(\lambda_i,\varphi_j,t)| w_j}{\sum_i \sum_j w_j} \end{aligned} \tag{5.1}$$

$$\begin{aligned} l_2\big(p_s(t)\big) &= \left(\frac{1}{4\pi} \int_0^{2\pi} \int_{-\frac{\pi}{2}}^{\frac{\pi}{2}} [p_{s_1}(\lambda,\varphi,t) - p_{s_2}(\lambda,\varphi,t)]^2 \, \cos\varphi \, d\varphi \, d\lambda \right)^{1/2} \\ &\approx \left(\frac{\sum_i \sum_j [p_{s_1}(\lambda_i,\varphi_j,t) - p_{s_2}(\lambda_i,\varphi_j,t)]^2 w_j}{\sum_i \sum_j w_j} \right)^{1/2} \end{aligned} \tag{5.2}$$

$$l_\infty\big(p_s(t)\big) = \max_{\text{all } i,j} |p_{s_1}(\lambda_i,\varphi_j,t) - p_{s_2}(\lambda_i,\varphi_j,t)| \tag{5.3}$$

where the sums are taken over all points (λ_i, φ_j) of the global grid and p_{s_1} and p_{s_2} represent the two cases being compared. The integration weights w_j are given following Eq. (4.1). As earlier Eq. (5.1) and Eq. (5.2) assume a tensor product grid with a uniform longitudinal grid interval. The model solutions must be interpolated to a common grid in order to calculate the norm. For each pair compared we interpolate from the coarser grid to the finer grid of the pair with horizontal spectral interpolation with no truncation. As outlined in Section 4 the GME data are also biquadratically interpolated to a regular latitude–longitude grid before further spectral interpolations are made for the norm calculations. All spectral interpolations are computed with SPHEREPACK, a publicly available analysis package for problems in spherical geometry (Adams and Swarztrauber 1997). The vorticity is calculated from the wind components u and v on the Gaussian or uniform latitude–longitude grids using spectral approximations. Again SPHEREPACK routines are applied.

5.5.1 Uncertainty in the reference solutions

Figures 5.19, 5.20, and 5.21 show the l_1, l_2 and l_∞ difference norms of the surface pressure, 850mb temperature and 850mb vorticity, respectively, for different models from the highest resolution class (first row), from the second-highest resolution class (second row), and from the highest resolution class with a model from the second-highest resolution class (third and fourth rows). Many

of the individual curves overlay each other and cannot be distinguished. The region below the maximum of all curves in each column of the figures is filled with yellow in all the plots of that column. The significance of this filled region will be discussed later.

The differences in the norms for days 0 to 6 are very small and are easily affected by the interpolations to a common grid needed to calculate the difference norms. The differences from day 0 to day 6 tend to be relatively flat, rather than growing as would be expected. This indicates that the differences are affected by something in addition to the growth of the perturbation itself. During this period dispersion and damping of the gravity waves affect the initial growth characteristics. In addition, the interpolation adds to the difference and can dominate. Thus the norms do not represent the actual difference in the unstable growing mode between the models during this period. That difference is smaller. Before day 6 the differences are very small in practical terms as seen in Figs. 5.1 – 5.4 where, for example, the temperature contours on day 4 are practically straight lines.

For days 7 through 14 the difference norms in the second rows of Figs. 5.19 – 5.21 which compare the different models in the second-highest resolution class are similar to those in first rows which compare models in the highest resolution class. Since the uncertainties are not decreasing going from second-highest to the highest resolution, these reference solutions are the best that can be obtained for the problem as posed here. The highest curves in the first and second rows of Figs. 5.19 – 5.21 provide an indication of the uncertainty in the reference solutions. This is further verified by the third and fourth rows which show the difference norms between a model from the highest resolution class with one from the second-highest class. The largest differences in third and fourth rows are very similar to the largest in the first and second rows again indicating the level of uncertainty in the reference solutions. Thus the top of the filled regions define the uncertainty of our reference solutions for that variable and norm.

Eventually the difference norms grow until they saturate and the two solutions are related to each other as if they were chosen randomly from all possible states. Figures 5.19 and 5.20 indicate that for surface pressure and temperature that leveling occurs around day 25 where the curves begin to level off. The asymptotic levels appear to differ somewhat between models. This apparent different level of saturation occurs because the perturbations in EUL, SLD and FV are in fact not fully developed in the Southern Hemisphere until after day 30, in contrast to GME. In general, the basic zonal state in the test case is symmetric about the equator. Thus any perturbation in the Southern Hemisphere will also grow. However, we impose an initial perturbation in the Northern Hemisphere only. Perturbations are introduced into the Southern Hemisphere by truncation errors and by gravity waves which arise from the geostrophic adjustment associated with the imposed unbalanced perturbation in the Northern Hemisphere and which propagate into the Southern Hemisphere. The perturbations introduced by the gravity waves are of similar amplitude for the different schemes at comparable resolutions, but the truncation errors are not. As indicated earlier by Figs. 4.1 and 4.2 the EUL and FV schemes approximate the zonal balanced state in the Southern Hemisphere rather well without any zonal variations in the truncation error. This is contrary to GME which truncation errors exhibit the built-in wavenumber 5 grid structure. For practical application these errors are small at the higher resolutions. Nevertheless in the Southern Hemisphere they grow fast and saturate sooner than the numerical errors introduced by the EUL, SLD and FV schemes. Notice that in fact the l_1 and l_2 norms for those schemes which saturate later continue to grow to day 30 and eventually reach the same level as the others. The l_∞ norm grows faster than the l_1 and l_2 norms as it reflects the smaller scales where the difference grows faster. Likewise the vorticity norms (Fig. 5.21) grow significantly faster than the corresponding surface pressure and

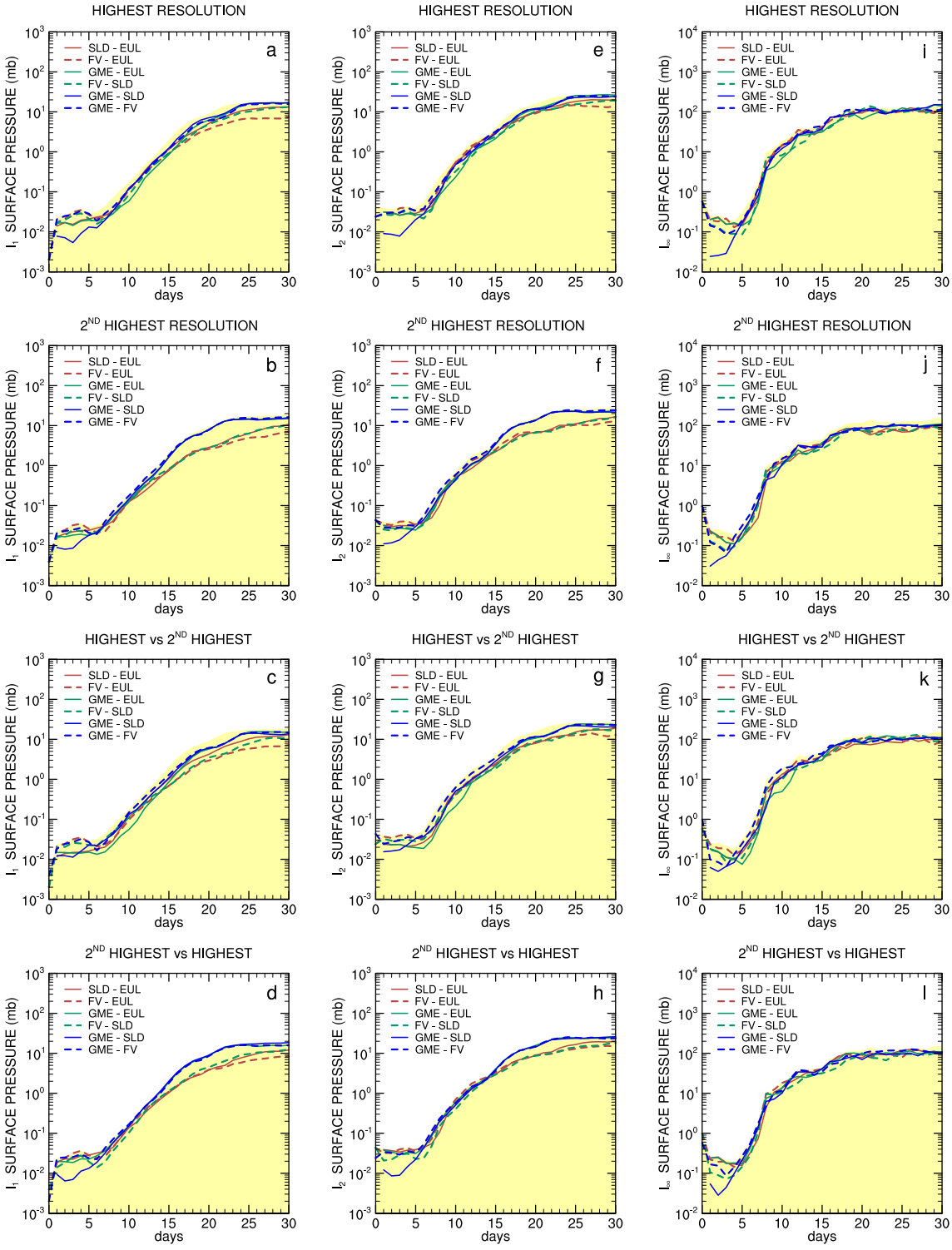

Figure 5.19: l_1, l_2 and l_∞ norms of the surface pressure differences (in hPa) between the four dynamical cores with 26 levels: (first row) highest horizontal resolutions, (second row) second-highest horizontal resolutions, (third and fourth rows) highest of one model compared to second-highest of the other.

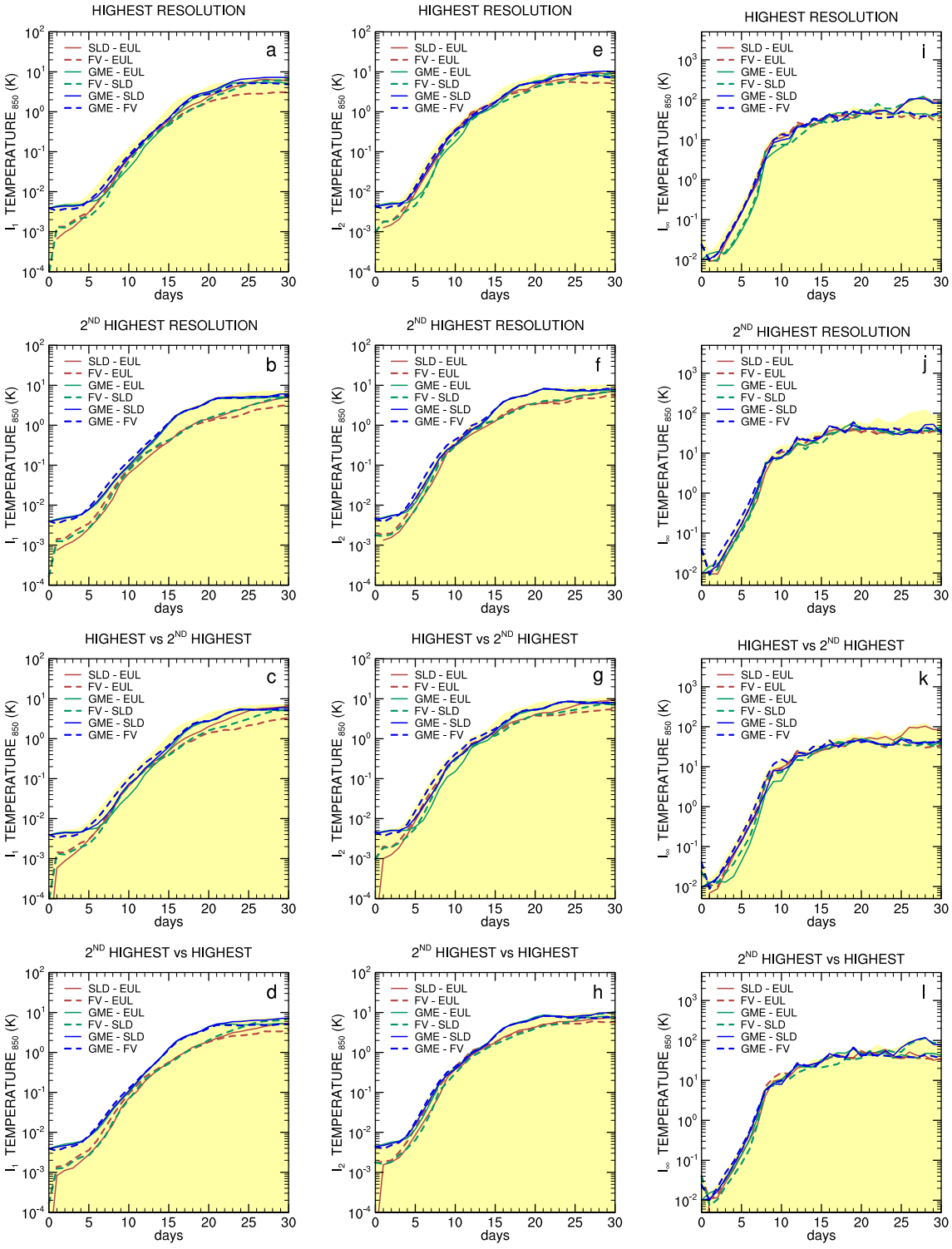

Figure 5.20: l_1, l_2 and l_∞ norms of the 850mb temperature differences (in K) between the four dynamical cores with 26 levels: (first row) highest horizontal resolutions, (second row) second-highest horizontal resolutions, (third and fourth rows) highest of one model compared to second-highest of the other.

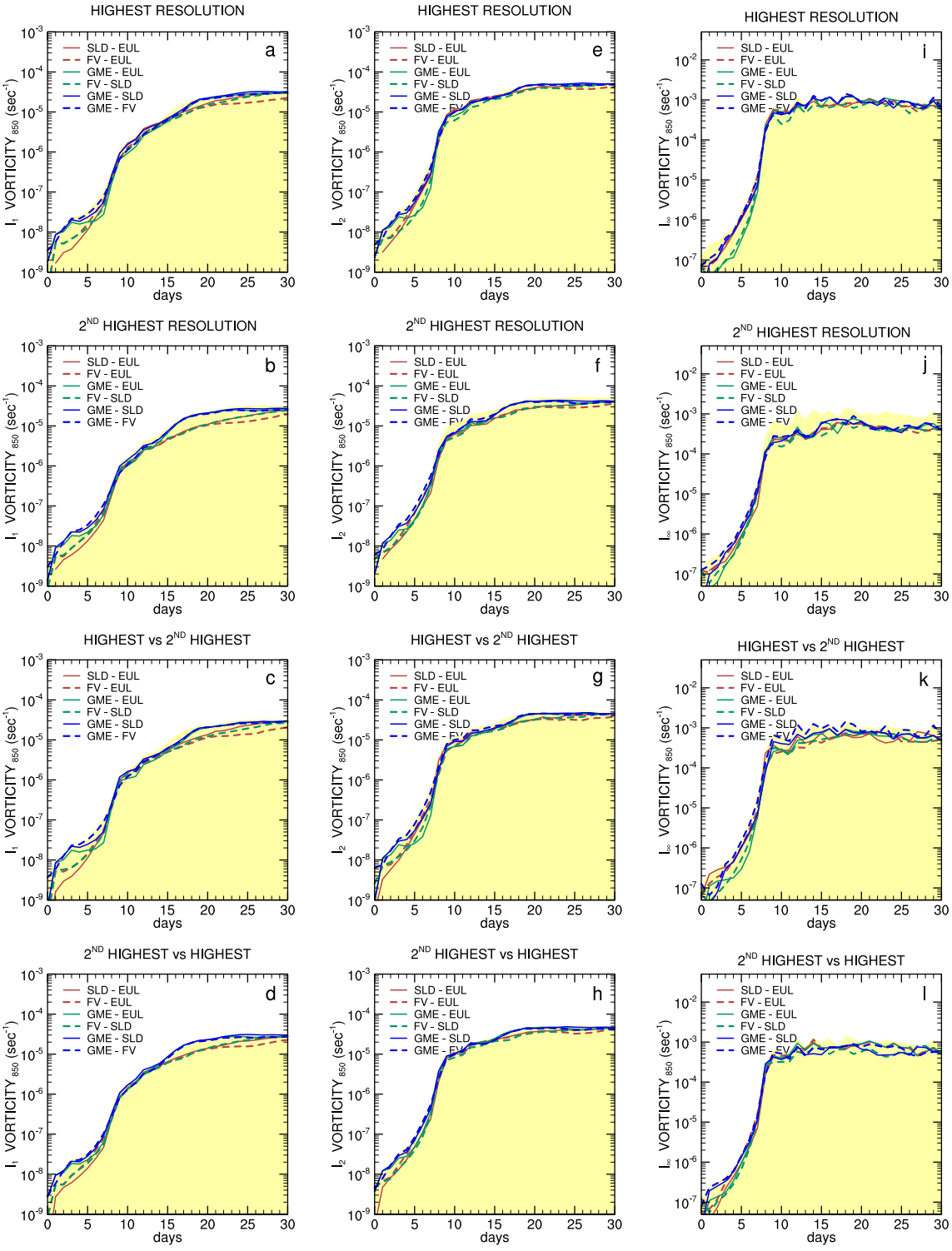

Figure 5.21: l_1, l_2 and l_∞ norms of the 850mb vorticity differences (in s^{-1}) between the four dynamical cores with 26 levels: (first row) highest horizontal resolutions, (second row) second-highest horizontal resolutions, (third and fourth rows) highest of one model compared to second-highest of the other.

temperature norms consistent with the smaller scale uncertainties being more noticeable in the vorticity as seen earlier in the maps of the fields (Figs. 5.9 – 5.12). As mentioned above, for reference in later figures, the regions below all lines in each column are filled in all figures for that norm and variable. The top of that filled region provides an estimate of the uncertainty in the reference solution.

5.5.2 Horizontal resolution

Figures 5.22, 5.23 and 5.24 show the convergence of surface pressure, temperature and vorticity respectively with increasing resolution for the EUL, SLD, FV and GME dynamical cores. Each is compared with the reference solution produced by the highest resolution version of the same model. The first and second rows show that the T42 EUL and SLD do not capture the reference solution to within the uncertainty, but the T85 EUL and SLD do. Likewise, the third rows show that the 2.0 FV does not capture the reference solution but the 1.0 FV does. For the GME (last row), ni64 does not capture the reference solution and the resolution must be at least ni128 to capture it to within the uncertainty.

Notice that the differences between higher resolution solutions of the same model are well below the uncertainty obtained from Figs. 5.19 – 5.21, e.g. T170-T340 EUL and SLD, and 0.5-0.25 FV. The decrease in differences with increasing horizontal resolution is the expected behavior for a single model. As horizontal resolution is increased the errors decrease so the differences between solutions also decrease. On first consideration this might be taken to imply our estimate of the uncertainty in the reference solutions is too large. Rather it implies a danger in using a single model to determine a reference solution for problems involving geostrophic adjustment and unstable states.

Figures 5.19 – 5.21 show that the solutions of different models do not become closer to each other with increasing resolution once the resolutions exceed a certain limit whereas in Figs. 5.22 – 5.24 the differences between solutions with the same model continue to decrease with increasing resolution. A possible explanation is that the truncation errors for a single model at different resolutions are more similar than the errors between models. Thus the differences involving a single model are initially smaller and remain smaller for a fixed elapsed time until saturation is reached. Although the perturbations introduced by the truncation errors of a single model are more similar and the evolving solutions are closer to each other, those solutions are not necessarily more accurate.

A more likely explanation for the convergence of inter-model differences is the different way each numerical method handles the geostrophic adjustment of the unbalanced initial perturbation. The models have different vertical approximations and different effective top boundary conditions, although the nominal level placement is the same in our experiments. With different vertical approximations the models are likely to project the imposed initial unbalanced perturbation differently onto the vertical modes, leading to a slightly different initial partition between the slow modes which grow with time, and the fast modes which are damped out, or at least remain small. This partition will be less affected by the horizontal resolution of a single scheme once it is fine enough with respect to the scales of the imposed initial wind perturbation.

The surface pressure and temperature differences represented by Figs. 5.19 and 5.20 and by Figs. 5.22 and 5.23 are relatively large scale. The corresponding differences for all cases truncated to a T42 representation are shown in Figs. 5.25 and 5.26 and by Figs. 5.28 and 5.29. The

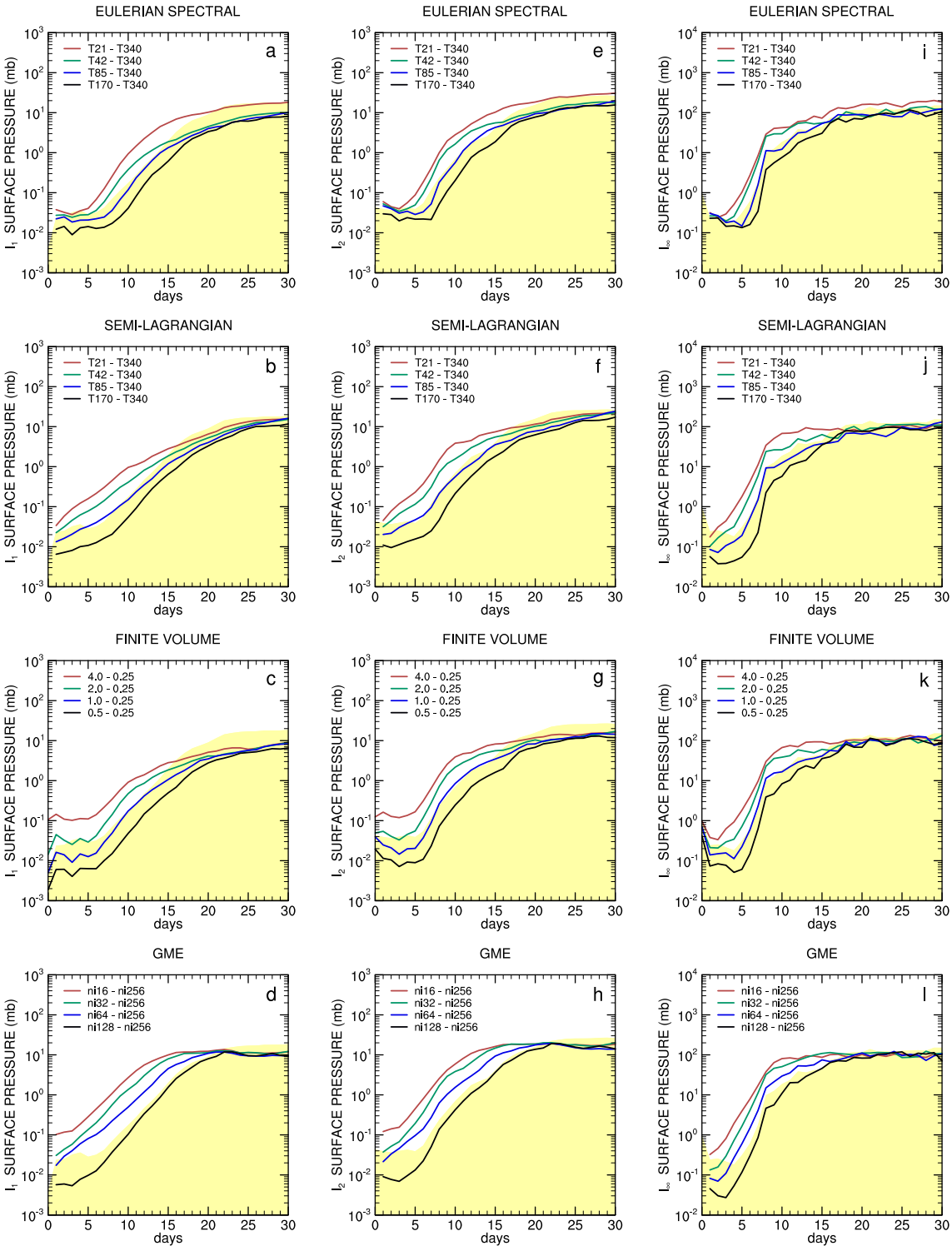

Figure 5.22: l_1, l_2 and l_∞ norms of the surface pressure differences (in hPa) for each horizontal resolution compared to the highest horizontal resolution of the same model with 26 levels: (first row) EUL, (second row) SLD, (third row) FV and (last row) GME.

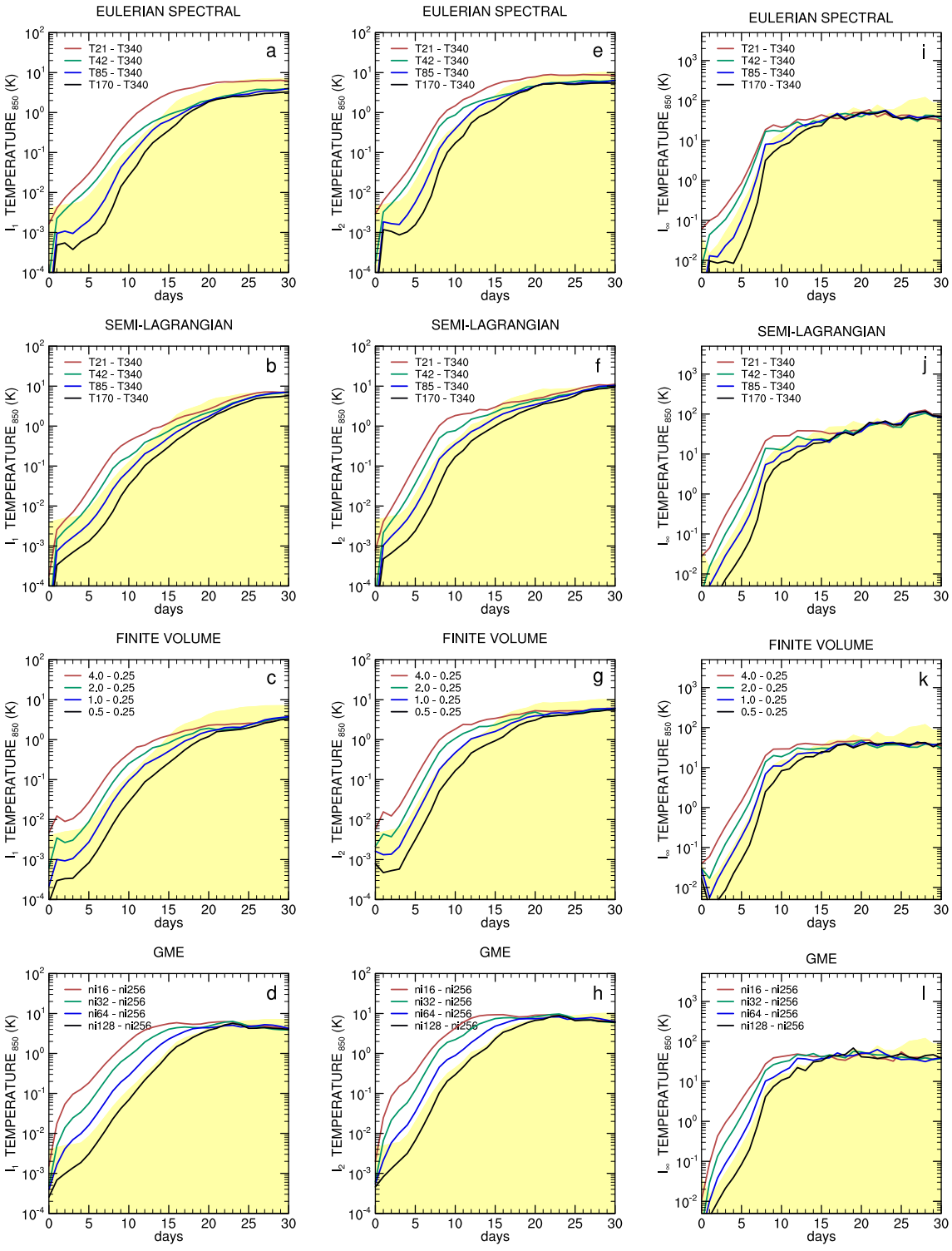

Figure 5.23: l_1, l_2 and l_∞ norms of the 850mb temperature differences (in K) for each horizontal resolution compared to the highest horizontal resolution of the same model with 26 levels: (first row) EUL, (second row) SLD, (third row) FV and (last row) GME.

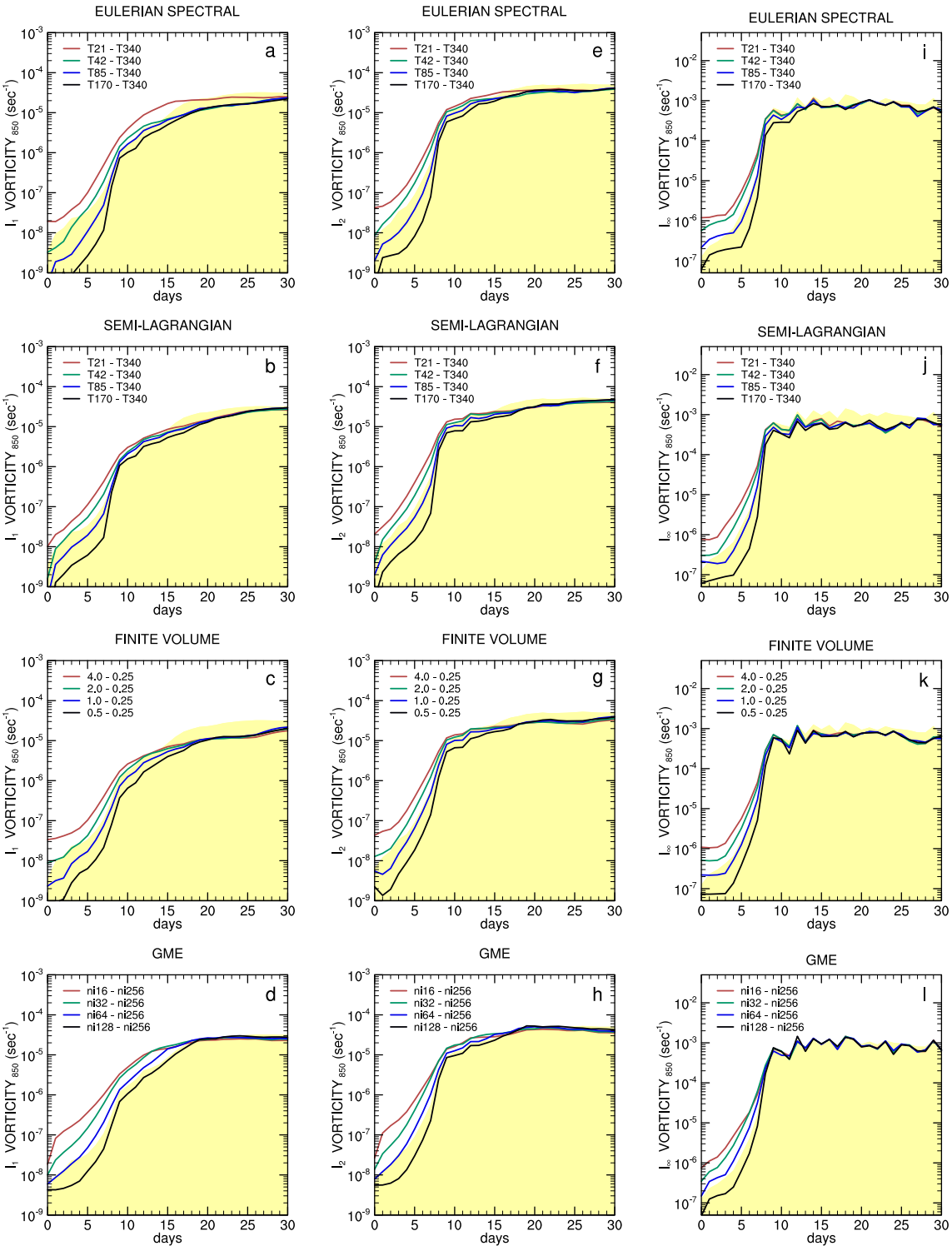

Figure 5.24: l_1, l_2 and l_∞ norms of the 850mb vorticity differences (in s^{-1}) for each horizontal resolution compared to the highest horizontal resolution of the same model with 26 levels: (first row) EUL, (second row) SLD, (third row) FV and (last row) GME.

curves with and without truncation are virtually identical. Thus at least T85 resolution is needed to calculate the T42 component of surface pressure and temperature to within the uncertainty of the reference solution for the EUL and SLD, while at least 1° is needed for the T42 component of the FV and ni128 for the T42 component of the GME. Vorticity, on the other hand, shows the effect of the truncation. Figs. 5.27 and 5.30 show the norms for vorticity truncated to T42. One can see a slower growth compared to the untruncated norms (Figs. 5.21 and 5.24), looking much more like the surface pressure and temperature curves. However the earlier conclusions with regard to the resolutions needed to capture the solution to within the uncertainty continue to hold for the truncated vorticity as well.

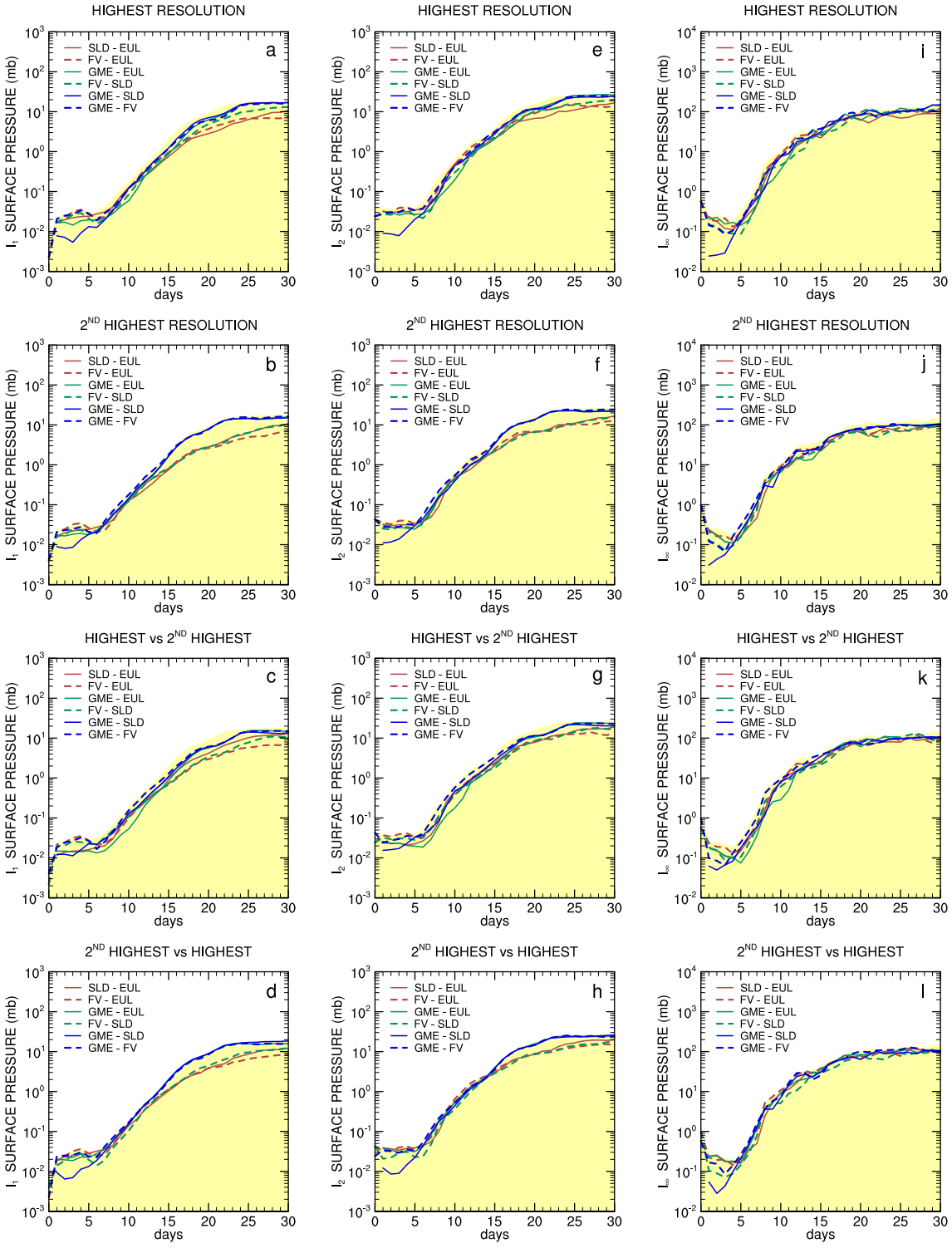

Figure 5.25: l_1, l_2 and l_∞ norms of the surface pressure differences (in hPa) between the four dynamical cores with 26 levels: (first row) highest horizontal resolutions, (second row) second-highest horizontal resolutions, (third and fourth rows) highest of one model compared to second-highest of the other. Fields are truncated to T42 before the calculations.

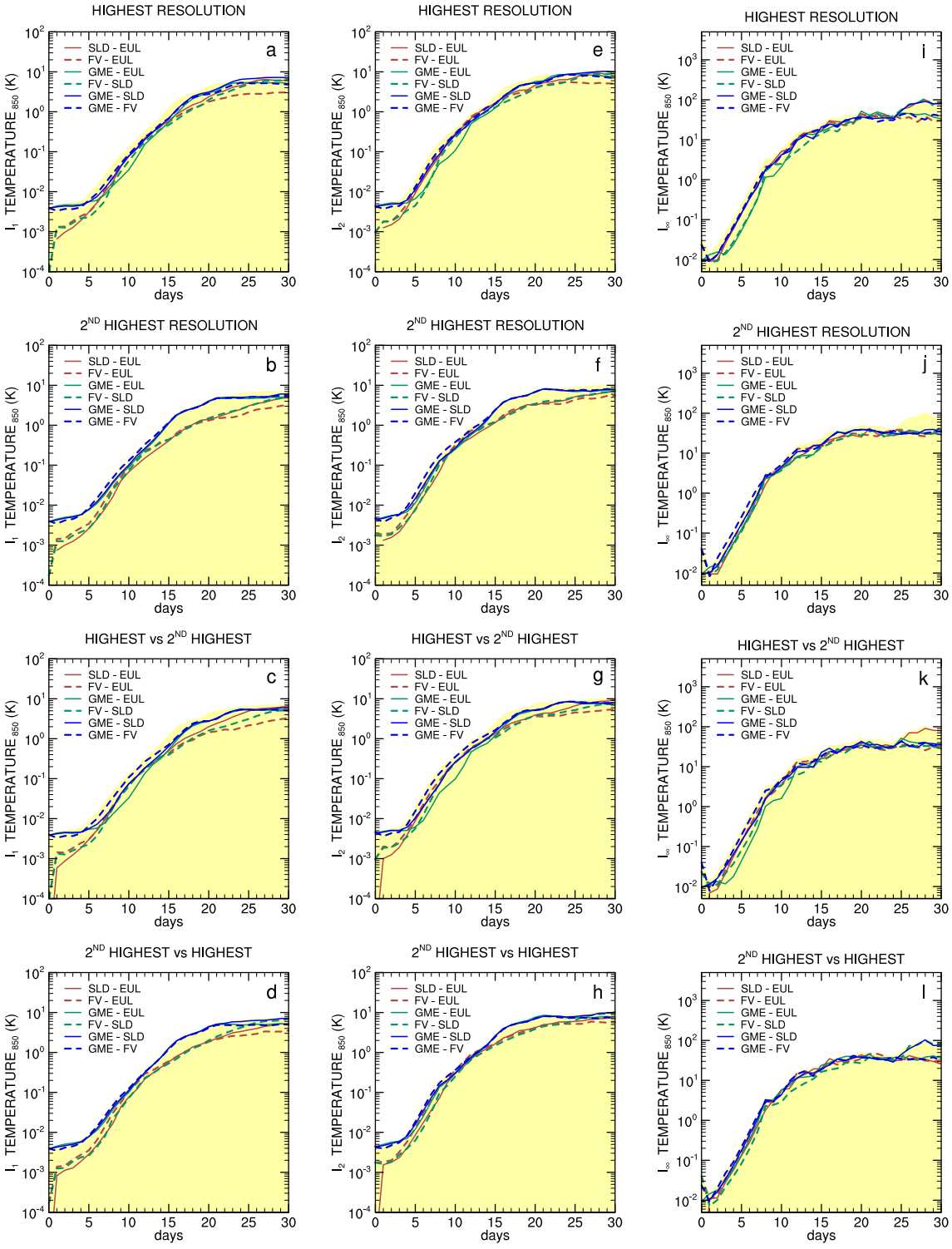

Figure 5.26: l_1, l_2 and l_∞ norms of the 850mb temperature differences (in K) between the four dynamical cores with 26 levels: (first row) highest horizontal resolutions, (second row) second-highest horizontal resolutions, (third and fourth rows) highest of one model compared to second-highest of the other. Fields are truncated to T42 before the calculations.

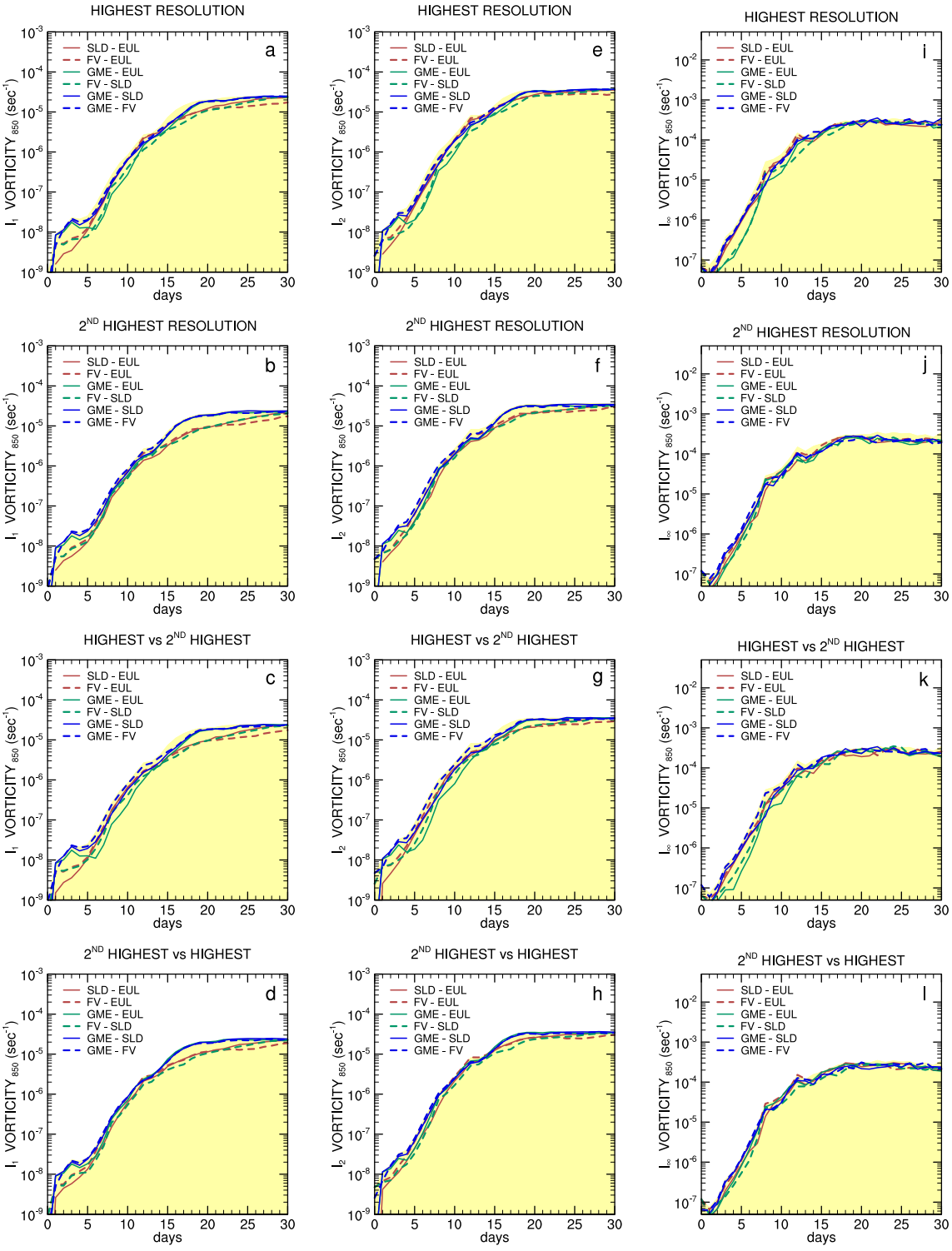

Figure 5.27: l_1, l_2 and l_∞ norms of the 850mb vorticity differences (in s^{-1}) between the four dynamical cores with 26 levels: (first row) highest horizontal resolutions, (second row) second-highest horizontal resolutions, (third and fourth rows) highest of one model compared to second-highest of the other. Fields are truncated to T42 before the calculations.

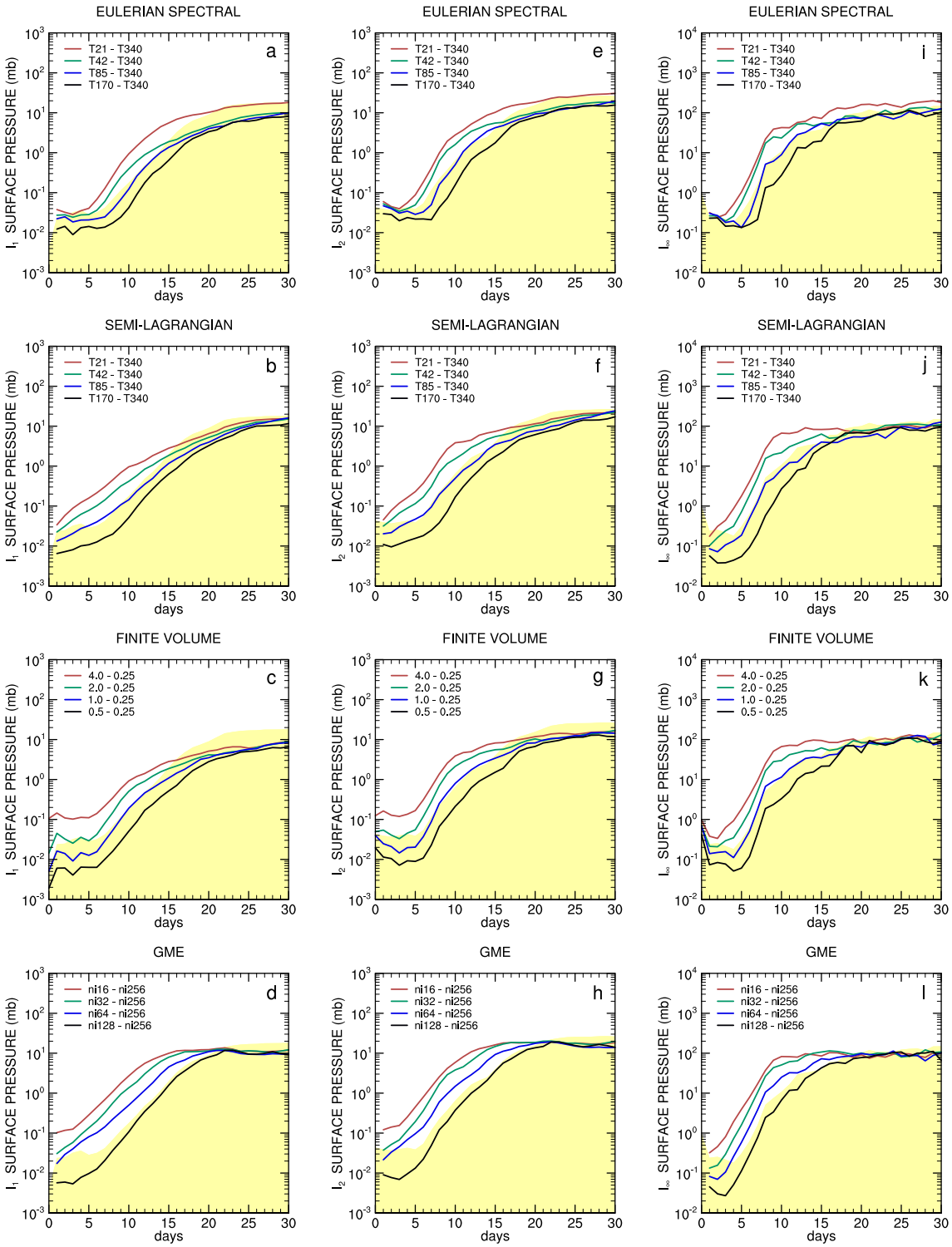

Figure 5.28: l_1, l_2 and l_∞ norms of the surface pressure differences (in hPa) for each horizontal resolution compared to the highest horizontal resolution of the same model with 26 levels: (first row) EUL, (second row) SLD, (third row) FV and (last row) GME. Fields are truncated to T42 before the calculations.

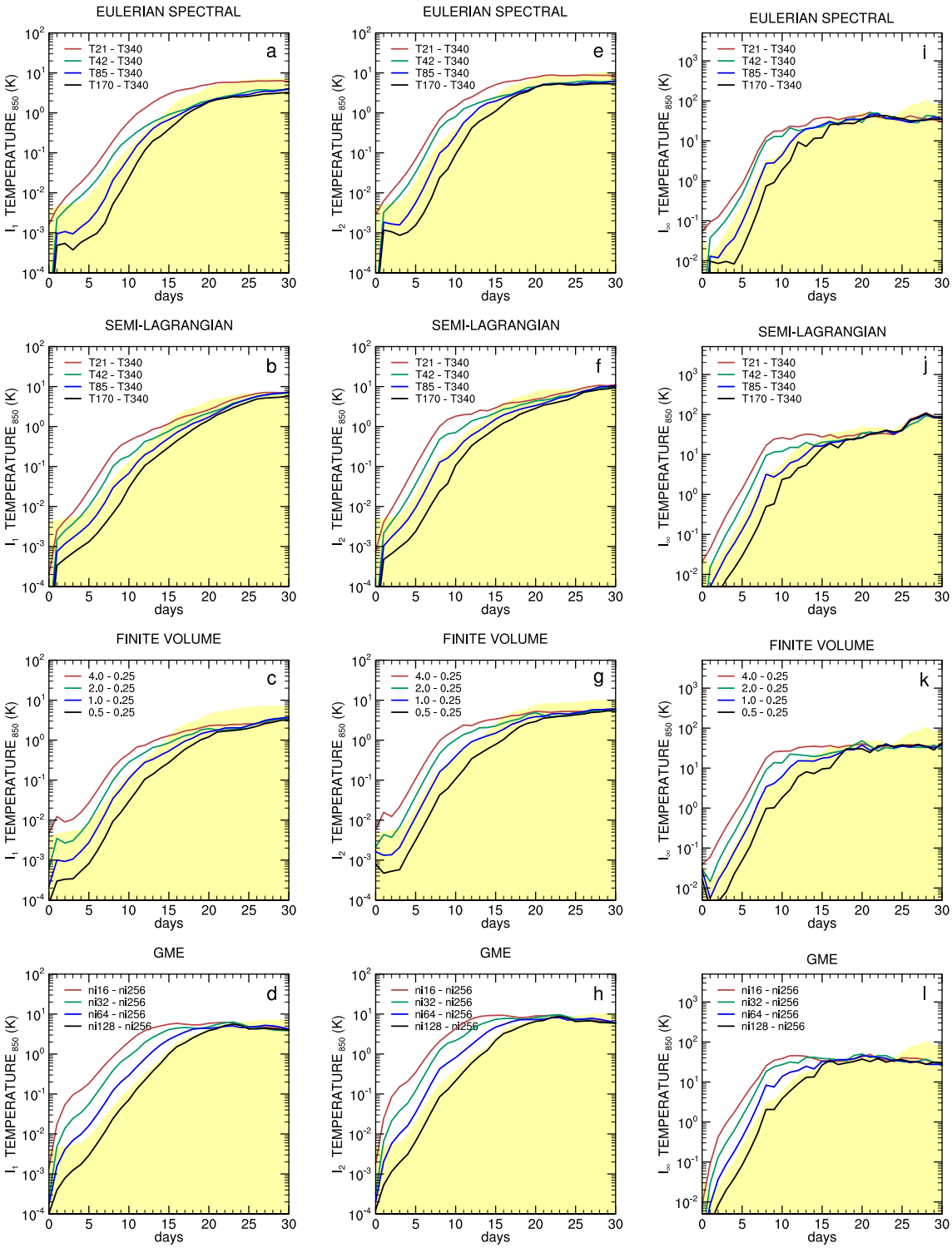

Figure 5.29: l_1, l_2 and l_∞ norms of the 850mb temperature differences (in K) for each horizontal resolution compared to the highest horizontal resolution of the same model with 26 levels: (first row) EUL, (second row) SLD, (third row) FV and (last row) GME. Fields are truncated to T42 before the calculations.

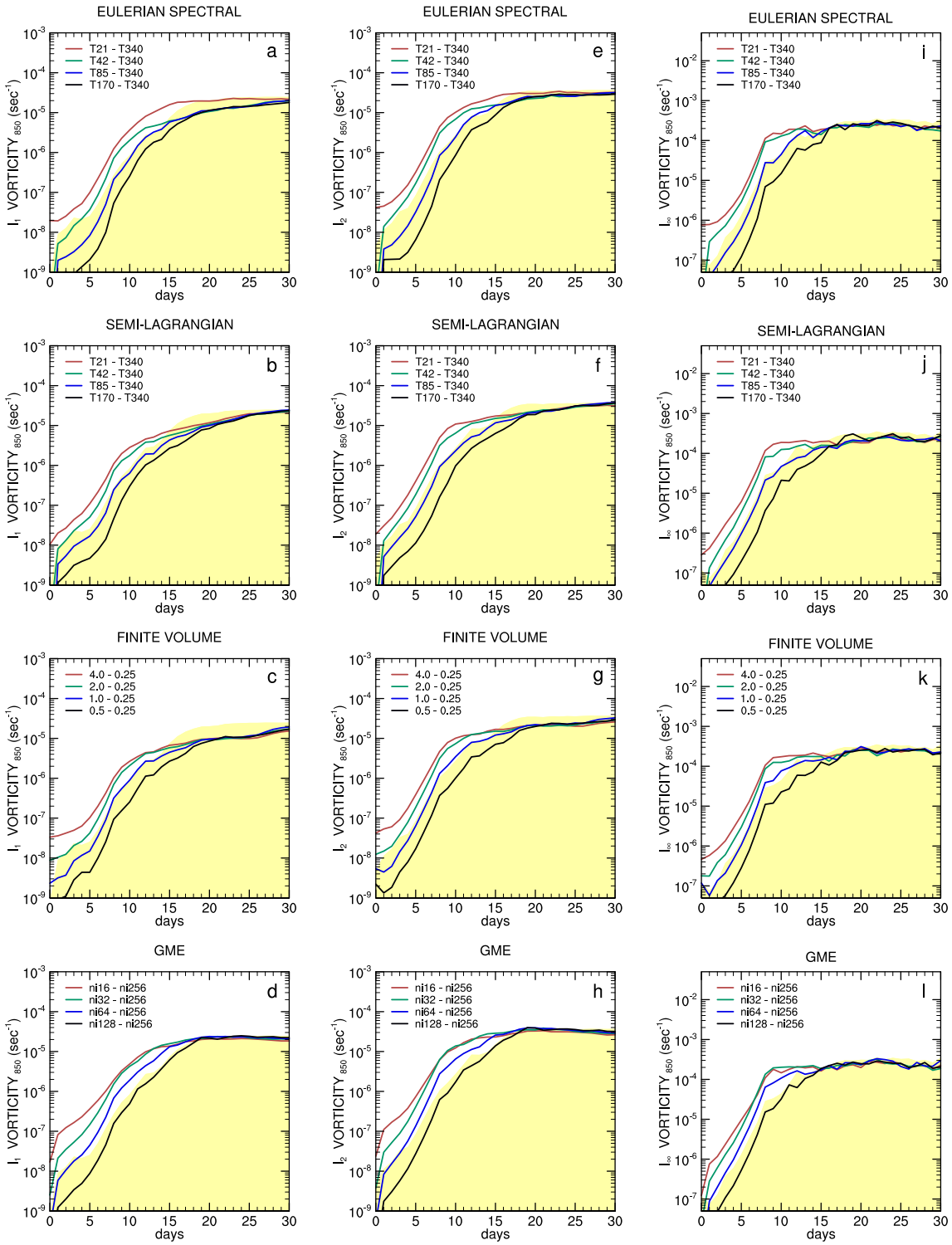

Figure 5.30: l_1, l_2 and l_∞ norms of the 850mb vorticity differences (in s^{-1}) for each horizontal resolution compared to the highest horizontal resolution of the same model with 26 levels: (first row) EUL, (second row) SLD, (third row) FV and (last row) GME. Fields are truncated to T42 before the calculations.

5.5.3 Phase error

Figure 5.31 shows the surface pressure phase error in degrees longitude for the various models, positive for phase lag of the coarser resolution model. We define the phase error to be the distance the field must be shifted in longitude with respect to the reference solution to produce the minimum l_2 difference. The reference solution is taken to be the highest resolution solution from the same model. The phase error is determined to an integral number of grid intervals of the reference solution. A meaningful phase error can only be calculated when there is a reasonable correlation between the growing unstable structures in the two fields. In our experience, the perturbation is neither large enough nor well organized enough to yield a consistent phase error before day 4. After day 10, the differences involving the coarser resolutions are too close to saturation (and randomly related) to yield a consistent phase error.

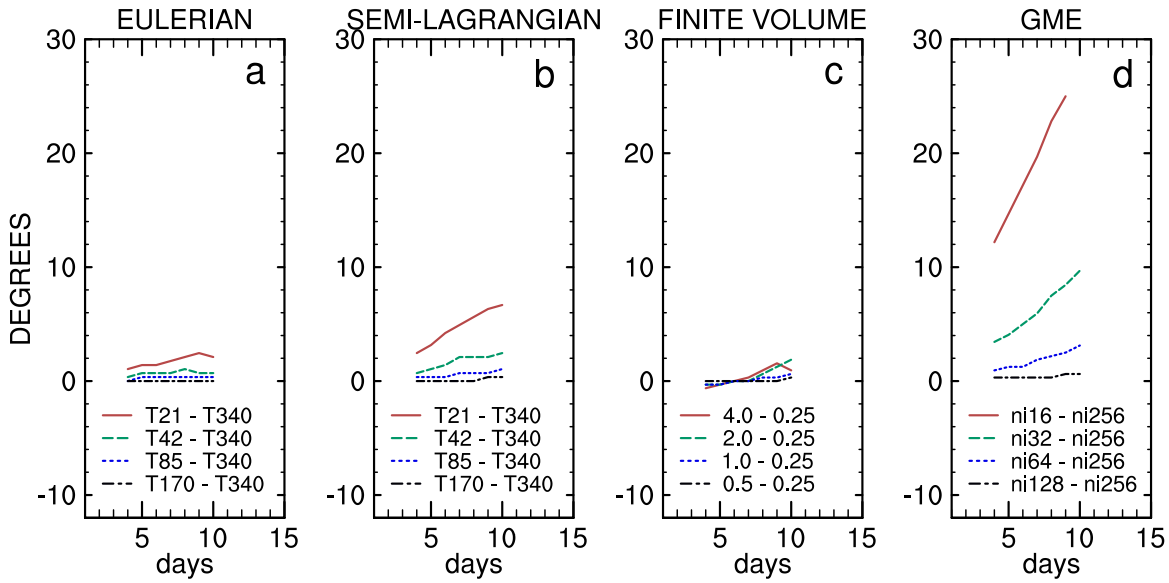

Figure 5.31: Surface pressure phase error (degrees longitude) for each horizontal resolution compared to the highest horizontal resolution for each model with 26 levels. The phase error is positive for a phase lag of the coarser resolution run.

The finer resolution solutions have insignificant phase error which is consistent with their matching the reference solution to within its uncertainty. The T21 EUL has about 2° phase error at day 10, and the 4.0 and 2.0 FV phase errors range from 1.5° to 2°. The T21 SLD phase error reaches 6.5° by day 10. The GME shows larger phase errors than the other three schemes at similar resolutions. The ni16, ni32 and ni64 GME phase errors are about 25°, 10°, and 3° respectively at day 10. The phase error is responsible for much of the total error in the ni64 GME solution, but not all. The "amplitude" error (not shown), i.e. the minimum l_2 used to determine the phase error, is close to the reference solution uncertainty but still does not fall within it. Some of the total error is also attributable to the growth of the wavenumber 5 perturbation.

5.5.4 Vertical Resolution

In addition to the standard 26-level configuration (see appendix B), calculations have also been performed with 18 and 49 vertical levels to address the impact of the vertical resolution on the reference state. For these simulations the mid-range horizontal resolutions are selected: T85 EUL and SLD, 1.0 FV and ni64 GME. Recall that the 26-level T85 EUL and SLD, and 1.0 FV have converged to within the uncertainty of the reference solutions, but the ni64 GME has not.

Figures 5.32 – 5.34 display the sensitivity of the solution to the vertical level distribution. The top rows of the figures show that the differences between all 49-level and 26-level model

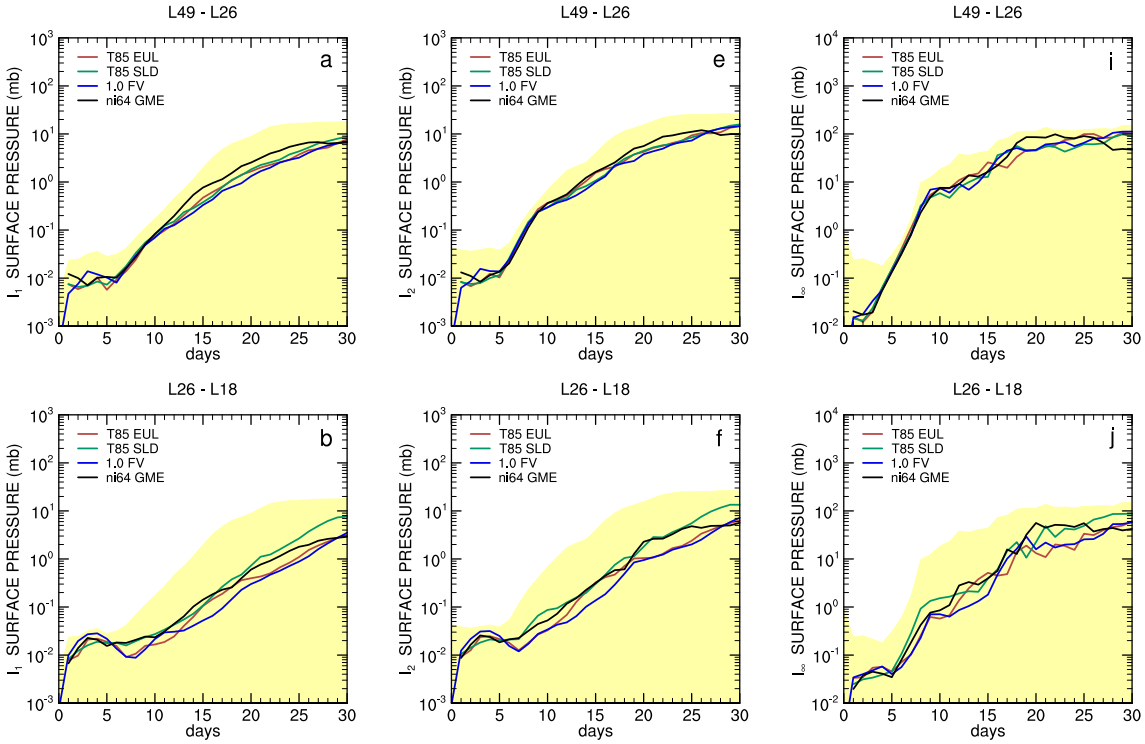

Figure 5.32: l_1, l_2 and l_2 norms of the surface pressure differences (in hPa) between each model (at its mid-range horizontal resolution) with different vertical resolutions: (first row) 49 levels versus 26 levels, (second row) 26 levels versus 18 levels.

simulations are within the uncertainty of the reference solutions. The same conclusion applies to the differences between the 26-level and 18-level model runs that are presented in second rows of the figures. However, these differences are significantly smaller than the differences between the 49-level and 26-level model setups. The effect is attributable to the similar placement of the levels in the 18- and 26-level configurations. This is especially true for the tropospheric levels since the 26-level distribution was created from the 18-level setup by adding levels around the tropopause with most of the new levels added between 200 hPa and 50 hPa (Williamson et al. 1998). Above 200 hPa the 26-level grid layers are therefore about half the thickness of the 18-level ones (in $\ln p$). In the lower troposphere, however, the levels of the two grids are very close to each other. As a consequence, the truncation errors of the 18- and 26-level setups are indeed very similar since the growing modes of our test case have most of their amplitude at lower levels. In contrast, the

level distribution of the 49-level configuration clearly differs from the 26-level setup in all regions which is reflected by the slightly elevated levels of the l_2 error norms. For practical purposes though, these differences stay well below the uncertainty limit so that the 26-level distribution is an adequate representative of the reference state.

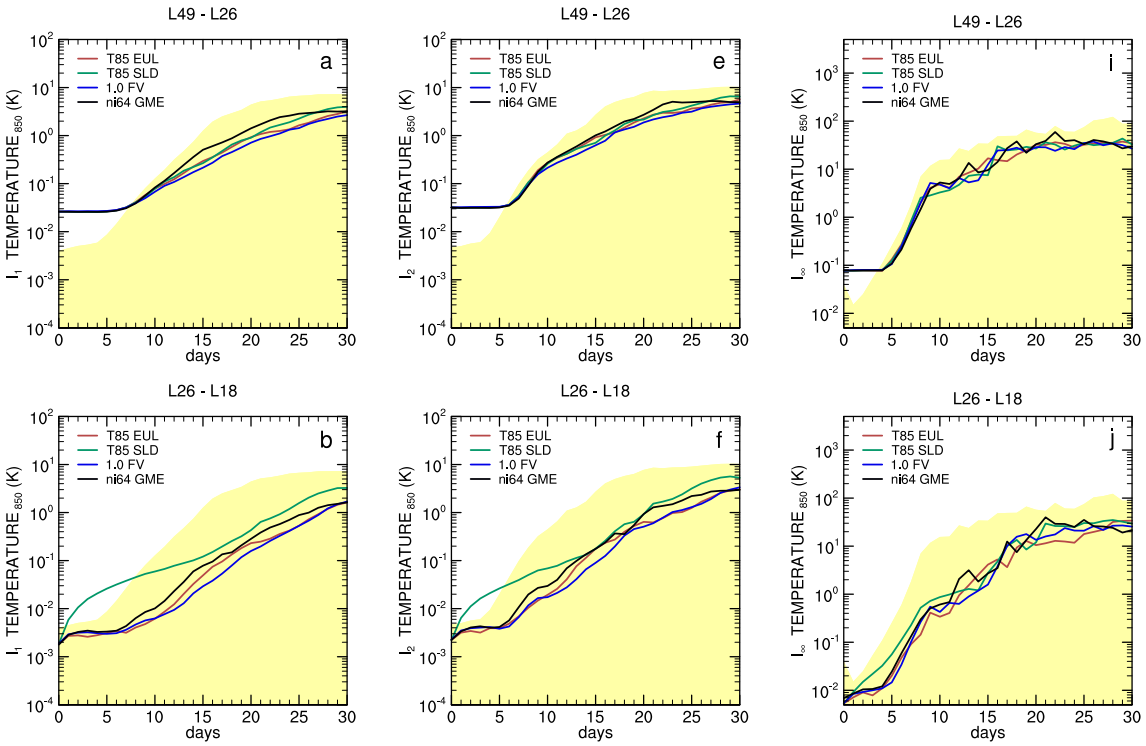

Figure 5.33: l_1, l_2 and l_2 norms of the 850mb temperature differences (in K) between each model (at its mid-range horizontal resolution) with different vertical resolutions: (first row) 49 levels versus 26 levels, (second row) 26 levels versus 18 levels.

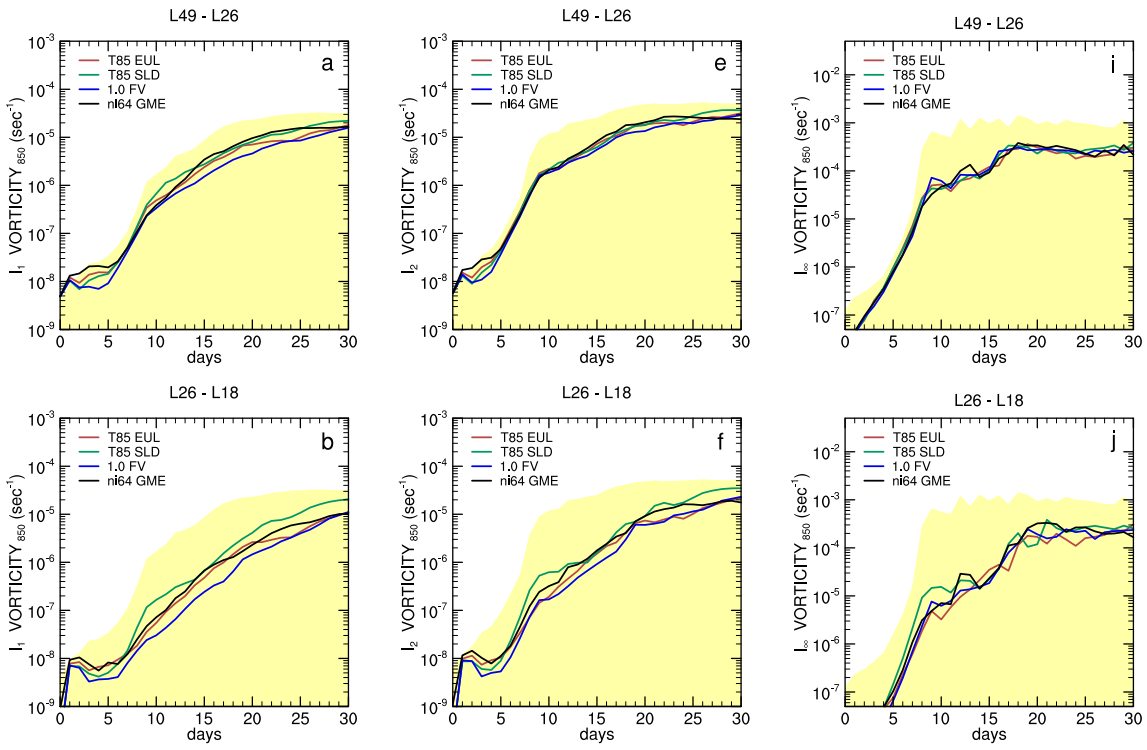

Figure 5.34: l_1, l_2 and l_2 norms of the 850mb vorticity differences (in s^{-1}) between each model (at its mid-range horizontal resolution) with different vertical resolutions: (first row) 49 levels versus 26 levels, (second row) 26 levels versus 18 levels.

Chapter 6

Summary

An idealized baroclinic wave test case for dynamical cores of GCMs has been developed that is deterministic, easy-to-use, relevant to typical atmospheric phenomena and applicable to a wide variety of model formulations and grids. The two-step test strategy first assesses the ability of the models to maintain a steady-state before an overlaid perturbation triggers the evolution of a baroclinic wave over the course of several days. The initial conditions are given in form of analytic expressions. The zonally symmetric initial state is a steady-state solution of the primitive equations that resembles the climatic conditions of a winter hemisphere.

The test has been applied to four very different dynamical cores at varying horizontal and vertical resolutions. In particular, two spectral transform models (Eulerian (EUL) and semi-Lagrangian (SLD)) and two grid point models (Finite Volume (FV) and DWD's finite difference, icosahedral model (GME)) with different numerical schemes and computational grids have been tested. All models provide independent reference solutions. The uncertainty in the reference solutions is established by comparing the solutions of all four dynamical cores at high horizontal resolutions. This approach not only takes the convergence-with-resolution characteristics of a single model into account but also assesses the cross-model differences to gain confidence in the reference states. Here, it is strongly emphasized that the maximum spread of all high resolution reference simulations defines the uncertainty of the reference state despite the fact that all single model assessments stay well below the uncertainty limit. Once a single model converges to within the uncertainty, finer horizontal resolutions do not provide a better estimate of the reference solution. Thus the test case tells the user at what resolution a new scheme is as good as those considered here and something about its behavior at coarser resolutions, but not at finer resolutions. In summary, it has been shown that the four dynamical cores with 26 levels converge to within the uncertainty at the horizontal resolutions EUL T85, SLD T85, FV $1.0^\circ \times 1.25^\circ$ and GME ni128. The higher resolution for GME was partly needed to reduce the phase error that is evident in the coarser GME simulations.

In the future, we would like to establish a standard test suite for dynamical cores that fosters the developments and intercomparisons of new numerical schemes and gridding options. We hope that this test finds broad acceptance in the modeling community to become part of such a test series. As a starting point for model intercomparions we make our reference solutions in netCDF format available online (contact the authors for details). In particular, the data sets contain the surface pressure fields for all four models at the highest and second-highest resolutions so that modeling groups can readily compute the l_2 norms against the established reference states.

Appendix A

Derivation of the analytic initial conditions

The derivation starts from the adiabatic and frictionless primitive equations in spherical (λ, φ) coordinates with hybrid η-levels. The u- and v-momentum equations, the hydrostatic equation as well as the continuity and thermodynamic equations are given by

$$\frac{d\,u}{d\,t} - \frac{u\,v\,\tan\varphi}{a} = \frac{-1}{a\,\cos\varphi}\left(\frac{\partial\,\Phi}{\partial\,\lambda} + R_d\,T\,\frac{\partial\,\ln p}{\partial\,\lambda}\right) + f\,v \tag{A.1}$$

$$\frac{d\,v}{d\,t} + \frac{u^2\,\tan\varphi}{a} = \frac{-1}{a}\left(\frac{\partial\,\Phi}{\partial\,\varphi} + R_d\,T\,\frac{\partial\,\ln p}{\partial\,\varphi}\right) - f\,u \tag{A.2}$$

$$\frac{\partial\,\Phi}{\partial\,\eta} = -\,\frac{R_d\,T}{p}\,\frac{\partial\,p}{\partial\,\eta} \tag{A.3}$$

$$\frac{\partial}{\partial t}\left(\frac{\partial p}{\partial \eta}\right) + \frac{1}{a\cos\varphi}\frac{\partial}{\partial\lambda}\left(u\,\frac{\partial p}{\partial\eta}\right) + \frac{1}{a\,\cos\varphi}\frac{\partial}{\partial\varphi}\left((v\cos\varphi)\,\frac{\partial p}{\partial\eta}\right) + \frac{\partial}{\partial\eta}\left(\dot\eta\,\frac{\partial p}{\partial\eta}\right) = 0 \tag{A.4}$$

$$\frac{d\,T}{d\,t} - \frac{R_d\,T\,\omega}{c_p\,p} = 0 \tag{A.5}$$

with the Coriolis parameter $f = 2\,\Omega\,\sin\varphi$. The constant $c_p = 1004$ J kg^{-1} K^{-1} stands for the specific heat of dry air at constant pressure, $\dot\eta$ is defined as $\dot\eta = d\eta/dt$ and $\omega = dp/dt$ symbolizes the pressure vertical velocity. The equation of state for dry air is given by

$$p = \rho\,R_d\,T$$

where ρ denotes the air density. In addition, the substantial derivative d/dt is defined as

$$\begin{aligned}\frac{d}{d\,t}(\,) &= \frac{\partial}{\partial\,t}(\,) + (\mathbf{v}\cdot\nabla)(\,)\\ &= \frac{\partial}{\partial\,t}(\,) + \frac{u}{a\,\cos\varphi}\frac{\partial}{\partial\,\lambda}(\,) + \frac{v}{a}\frac{\partial}{\partial\,\varphi}(\,) + \dot\eta\,\frac{\partial}{\partial\,\eta}(\,).\end{aligned}$$

All other symbols are explained in Section 2.1. For $p_s = p_0 = 10^5$ Pa with $p = \eta\,p_s$ (compare to appendix B) the hydrostatic equation (Eq. (A.3)) is equivalent to

$$\frac{\partial\,\Phi'}{\partial\,\eta} = \frac{-\,R_d\,T'}{\eta} \tag{A.6}$$

where Φ' and T' indicate the deviations from the horizontal-mean geopotential and temperature fields.

Based on this formulation the goal is to derive an analytic, steady-state balanced initial data set for the model variables u, v, p_s, T, Φ_s where Φ_s stands for the surface geopotential. The derivation contains several degrees of freedom. Here the chosen wind profiles and constant parameters guarantee that the resulting initial data closely resemble a realistic climatic state and fulfill the symmetric, inertial and static stability criterion. On the other hand, the flow is designed to be baroclinically and barotropically unstable. The derivation steps are

1. Choose a nondivergent wind field u and v and a constant p_s distribution (see Section 2.1).

2. Choose the horizontally averaged temperature profile $\langle\, T(\eta)\,\rangle$. This is first done in z coordinates using
$$\langle\, T\rangle = T_0 - \Gamma\, z \tag{A.7}$$
where $\Gamma = 0.005$ K m^{-1} is the vertical temperature gradient, $T_0 = 288$ K represents the horizontal-mean temperature at the surface and z denotes the horizontal-mean geopotential height in m. This equation is then transformed into the p system via integration of the hydrostatic relationship
$$\frac{\partial\, p}{p} = -\,\frac{g}{R_d\,\langle\, T\rangle}\;\partial z\;.$$
It follows
$$z = \frac{T_0}{\Gamma}\Big(\,1\,-\,\big(\frac{p}{p_0}\big)^{\frac{R_d\,\Gamma}{g}}\,\Big) \tag{A.8}$$
with $p_0 = p(z_0 = 0\text{ m}) = 10^5$ Pa. Equations (A.7) and (A.8) result in the expression for $\langle\, T(\eta)\,\rangle$ (Eq. (2.4)) with $\eta = p/p_0$.

3. Derive the geopotential Φ and compute the surface geopotential Φ_s: The derivation starts from the v momentum equation (Eq. (A.2)). A steady-state solution with $dv/dt = 0$ is sought. In case of a constant p_s field $\partial \ln p/\partial\varphi$ vanishes on constant η-surfaces. The chosen u wind profile (Eq. (2.2)) is inserted into the steady-state momentum equation for v
$$\frac{1}{a}\;\frac{\partial\Phi'}{\partial\varphi} = -\;u\;(2\;\Omega\;\sin\varphi\;+\;\frac{u}{a}\;\tan\varphi) \tag{A.9}$$
which is integrated analytically over φ. The integration leads to
$$\begin{aligned}\Phi'(\lambda,\varphi,\eta) = u_0\;\cos^{\frac{3}{2}}\eta_v\;\Big\{\,-\,2\sin^6\varphi\;\Big(\,\cos^2\varphi + \frac{1}{3}\Big)\,u_0\;\cos^{\frac{3}{2}}\eta_v\,+\\ \frac{8}{5}\cos^3\varphi\;\Big(\,\sin^2\varphi + \frac{2}{3}\Big)\;a\;\Omega\;\Big\} + \Phi_0(\eta)\end{aligned} \tag{A.10}$$
with a level-dependent integration constant $\Phi_0(\eta)$. Recall that η_v is defined as
$$\eta_v = (\eta - \eta_0)\frac{\pi}{2}\;.$$
Using the condition that the deviations Φ' from the horizontal mean must vanish when averaged horizontally $\Phi_0(\eta)$ is derived via
$$\frac{1}{4\pi}\int_0^{2\pi}\int_{-\frac{\pi}{2}}^{\frac{\pi}{2}}\Phi'(\lambda,\varphi,\eta)\;\cos\varphi\;d\varphi\,d\lambda = 0\quad.$$

This results in the expression

$$\Phi_0(\eta) = u_0 \ \cos^{\frac{3}{2}} \eta_v \left(\frac{10}{63} \ u_0 \ \cos^{\frac{3}{2}} \eta_v \ - \frac{\pi}{4} \ a \ \Omega \right) \quad . \tag{A.11}$$

The geopotential is given by $\Phi(\lambda, \varphi, \eta) = \langle \, \Phi(\eta) \, \rangle \ + \ \Phi'(\lambda, \varphi, \eta)$ where $\langle \, \Phi(\eta) \, \rangle$ is the horizontally averaged geopotential. In hydrostatic GCMs, it is only necessary to calculate the surface geopotential Φ_s where the horizontally averaged geopotential $\langle \, \Phi(\eta_s) \, \rangle$ at the surface level $\eta_s = 1$ is set to zero.

4. Finally, the temperature deviations T' are analytically derived using the hydrostatic equation (Eq. (A.6)) and the newly derived expression for Φ' (Eq. (A.10))

$$T'(\lambda, \varphi, \eta) = \frac{-\eta}{R_d} \ \frac{\partial \Phi'(\lambda, \varphi, \eta)}{\partial \eta} \quad . \tag{A.12}$$

The temperature field T is then composed of

$$T(\lambda, \varphi, \eta) = \langle \, T(\eta) \, \rangle \ + \ T'(\lambda, \varphi, \eta) \tag{A.13}$$

as displayed in Eq. (2.6). $\langle \, T(\eta) \, \rangle$ is the horizontally averaged temperature which is discussed in step 2. At upper levels $\langle \, T(\eta) \, \rangle$ is modified to introduce the typical stratospheric and mesospheric temperature profiles (Eq. (2.5)).

In this setup, the initial vertical velocities ω and $\dot{\eta}$ are zero when imposing the boundary condition $\dot{\eta} = 0$ at the lower and upper boundaries $\eta = 1$ and $\eta = 0$. In addition, the u-momentum (Eq. (A.1)), continuity (Eq. (A.4)) and thermodynamic (Eq. (A.5)) equations are automatically fulfilled. A baroclinic wave can be triggered when overlaying the steady-state initial conditions with an unbalanced perturbation at each model level.

Appendix B

Vertical η coordinate

The hybrid orography-following η-coordinate (Simmons and Burridge 1981) comprises a pure pressure coordinate and a σ-component with $\sigma = p/p_s$. The pressure p at a vertical level η is given by

$$p(\lambda, \varphi, \eta, t) = a(\eta)\, p_0 + b(\eta)\, p_s(\lambda, \varphi, t) \tag{B.1}$$

where the coefficients $a(\eta)$ and $b(\eta)$ are height-dependent and provided in tabular form (see below). Most commonly the reference pressure p_0 is set to 10^5 Pa or 1.01325×10^5 Pa. Here, a setup with $p_0 = 10^5$ Pa is chosen which coincides with the constant initial surface pressure p_s. This leads to the simplified expression

$$p(\lambda, \varphi, \eta, t = 0) = (a(\eta) + b(\eta))\, p_0 = \eta\, p_0\,. \tag{B.2}$$

In the discrete representation, the vertical direction is subdivided into N_{lev} model levels which are bounded by $N_{lev} + 1$ interface levels (denoted by the half indices $k + \frac{1}{2}$ below). The pressure at the interfaces is then given by

$$p_{k+\frac{1}{2}} = a_{k+\frac{1}{2}}\, p_0 + b_{k+\frac{1}{2}}\, p_s = \eta_{k+\frac{1}{2}}\, p_0 \tag{B.3}$$

with $\eta_{k+\frac{1}{2}} = a_{k+\frac{1}{2}} + b_{k+\frac{1}{2}}$ and $k = 0, 1, 2, \cdots N_{lev}$. The corresponding η_k values at the centers are determined via the average $\eta_k = \frac{1}{2}\,(\eta_{k+\frac{1}{2}} + \eta_{k-\frac{1}{2}})$. It follows $p_k = \eta_k\, p_0$.

For the baroclinic wave tests described here, three setups with 18, 26 and 49 model levels are chosen. The corresponding coefficients for the model interfaces $a_{k+\frac{1}{2}}$ and $b_{k+\frac{1}{2}}$ are listed in Tables B.1 and B.2. Here it is important to note that some GCMs (for example Majewski et al. (2002)) employ the alternative notation $p_{k+\frac{1}{2}} = a_{k+\frac{1}{2}} + b_{k+\frac{1}{2}}\, p_s$ where the coefficients $a_{k+\frac{1}{2}}$ are given in Pa. If such a setup is encountered, the $a_{k+\frac{1}{2}}$ coefficients in Tables B.1 and B.2 need to be multiplied by p_0.

Table B.1: Vertical coefficients for the 18- and 26-level setups. The parameter $a_{k+\frac{1}{2}}$ denotes the pure pressure component, $b_{k+\frac{1}{2}}$ defines the σ part of the hybrid η-system.

Index	18 Model levels (L18)		26 Model levels (L26)	
k	$a_{k+\frac{1}{2}}$	$b_{k+\frac{1}{2}}$	$a_{k+\frac{1}{2}}$	$b_{k+\frac{1}{2}}$
0	0.00251499	0.	0.002194067	0.
1	0.00710361	0.	0.004895209	0.
2	0.01904260	0.	0.009882418	0.
3	0.04607560	0.	0.01805201	0.
4	0.08181860	0.	0.02983724	0.
5	0.07869805	0.03756984	0.04462334	0.
6	0.07463175	0.08652625	0.06160587	0.
7	0.06955308	0.1476709	0.07851243	0.
8	0.06339061	0.221864	0.07731271	0.01505309
9	0.05621774	0.308222	0.07590131	0.03276228
10	0.04815296	0.4053179	0.07424086	0.05359622
11	0.03949230	0.509588	0.07228744	0.07810627
12	0.03058456	0.6168328	0.06998933	0.1069411
13	0.02193336	0.7209891	0.06728574	0.1408637
14	0.01403670	0.816061	0.06410509	0.1807720
15	0.007458598	0.8952581	0.06036322	0.2277220
16	0.002646866	0.953189	0.05596111	0.2829562
17	0.	0.985056	0.05078225	0.3479364
18	0.	1.	0.04468960	0.4243822
19			0.03752191	0.5143168
20			0.02908949	0.6201202
21			0.02084739	0.7235355
22			0.01334443	0.8176768
23			0.00708499	0.8962153
24			0.00252136	0.9534761
25			0.	0.9851122
26			0.	1.

Table B.2: Same as Table B.1 but for the 49-level setup.

Index	49 Model levels (L49)		Index	49 Model levels (L49)	
k	$a_{k+\frac{1}{2}}$	$b_{k+\frac{1}{2}}$	k	$a_{k+\frac{1}{2}}$	$b_{k+\frac{1}{2}}$
0	0.002251865	0.	25	0.07118414	0.1556586
1	0.003983890	0.	26	0.06962863	0.1737837
2	0.006704364	0.	27	0.06795950	0.1932327
3	0.01073231	0.	28	0.06616846	0.2141024
4	0.01634233	0.	29	0.06424658	0.2364965
5	0.02367119	0.	30	0.06218433	0.2605264
6	0.03261456	0.	31	0.05997144	0.2863115
7	0.04274527	0.	32	0.05759690	0.3139801
8	0.05382610	0.	33	0.05504892	0.3436697
9	0.06512175	0.	34	0.05231483	0.3755280
10	0.07569850	0.	35	0.04938102	0.4097133
11	0.08454283	0.	36	0.04623292	0.4463958
12	0.08396310	0.006755112	37	0.04285487	0.4857576
13	0.08334103	0.01400364	38	0.03923006	0.5279946
14	0.08267352	0.02178164	39	0.03534049	0.5733168
15	0.08195725	0.03012778	40	0.03116681	0.6219495
16	0.08118866	0.03908356	41	0.02668825	0.6741346
17	0.08036393	0.04869352	42	0.02188257	0.7301315
18	0.07947895	0.05900542	43	0.01676371	0.7897776
19	0.07852934	0.07007056	44	0.01208171	0.8443334
20	0.07751036	0.08194394	45	0.007959612	0.8923650
21	0.07641695	0.09468459	46	0.004510297	0.9325572
22	0.07524368	0.1083559	47	0.001831215	0.9637744
23	0.07398470	0.1230258	48	0.	0.9851122
24	0.07263375	0.1387673	49	0.	1.

Bibliography

Adams, J. C. and P. N. Swarztrauber, 1997: SPHEREPACK 2.0: A model development facility. NCAR Tech. Note NCAR/TN-436-STR, National Center for Atmospheric Research, Boulder, Colorado, 59 pp.

Bates, J. R. and Y. Li, 1997: Simulation of stratospheric vortex erosion using three global shallow water numerical models. *Numerical Methods in Atmospheric and Oceanic Modelling: The André J. Robert Memorial Volume of Atmos.-Ocean*, J. Côté, ed., 55–73.

Boer, G. J. and B. Denis, 1997: Numerical covergence of the dynamics of a GCM. *Climate Dynamics*, **13**, 359–374.

Bonaventura, L., 2003: Development of the ICON dynamical core: modelling strategies and preliminary results. *ECMWF/SPARC Workshop on Modelling and Assimilation for the Stratosphere and Tropopause*, 197–213.

Colella, P. and P. R. Woodward, 1984: The Piecewise Parabolic Method (PPM) for gas-dynamical simulations. *J. Comput. Phys.*, **54**, 174–201.

Collins, W. D., P. J. Rasch, B. A. Boville, J. J. Hack, J. R. McCaa, D. L. Williamson, B. P. Briegleb, C. M. Bitz, S.-J. Lin, M. Zhang, and Y. Dai, 2006: The formulation and atmospheric simulation of the Community Atmosphere Model: CAM3. J. Climate. In press.

Collins, W. D., P. J. Rasch, B. A. Boville, J. J. Hack, J. R. McCaa, D. L. Williamson, J. T. Kiehl, B. Briegleb, C. Bitz, S.-J. Lin, M. Zhang, and Y. Dai, 2004: Description of the NCAR Community Atmosphere Model (CAM3.0). NCAR Tech. Note NCAR/TN-464+STR, National Center for Atmospheric Research, Boulder, Colorado, 226 pp.

Fournier, A., M. A. Taylor, and J. J. Tribbia, 2004: The spectral element atmospheric model: High-resolution parallel computation and response to regional forcing. *Mon. Wea. Rev.*, **132**, 726–748.

Gates, W. L., ed., 1995: *Proceedings of the First International AMIP Scientific Conference*, 15-19 May 1995, Monterey, CA, World Climate Research Program Report WCRP-92, WMO/TD-No. 732, Geneva, 532 pp.

Gates, W. L., J. S. Boyle, C. C. Covey, C. G. Dease, C. M. Doutriaux, R. S. Drach, M. Fiorino, P. J. Gleckler, J. J. Hnilo, S. M. Marlais, T. J. Phillips, G. L. Potter, B. D. Santer, K. R. Sperber, K. E. Taylor, and D. N. Williams, 1999: An overview of the results of the Atmospheric Model Intercomparison Project (AMIP I). *Bull. Amer. Meteor. Soc.*, **80**, 29–55.

Giraldo, F. X. and T. E. Rosmond, 2004: A scalable Spectral Element Eulerian Atmospheric Model (SEE-AM) for NWP: Dynamical core tests. *Mon. Wea. Rev.*, **132**, 133–153.

Held, I. M. and M. J. Suarez, 1994: A proposal for the intercomparison of the dynamical cores of atmospheric general circulation models. *Bull. Amer. Meteor. Soc.*, **75**, 1825–1830.

Holton, J. R., 1992: *An Introduction to Dynamic Meteorology*. Academic Press, Inc., Third edition, ISBN 0-12-354355-X, 511 pp.

Hoskins, B. J. and A. J. Simmons, 1975: A multi-layer spectral model and the semi-implicit method. *Quart. J. Roy. Meteor. Soc.*, **101**, 637–655.

Jablonowski, C., 2004: *Adaptive Grids in Weather and Climate Modeling*. Ph.D. dissertation, University of Michigan, Ann Arbor, MI, Department of Atmospheric, Oceanic and Space Sciences, 292 pp.

Jablonowski, C. and D. L. Williamson, 2006: A baroclinic instabilitiy test case for atmospheric model dynamical cores. Submitted to Quart. J. Roy. Meteor. Soc.

Juckes, M. N. and M. E. McIntyre, 1987: A high-resolution one-layer model of breaking planetary waves in the stratosphere. *Nature*, **328**, 590–596.

Kiehl, J. T., J. J. Hack, G. B. Bonan, B. A. Boville, D. L. Williamson, and P. J. Rasch, 1998: The National Center for Atmospheric Research Community Climate Model: CCM3. *J. Climate*, **11**, 1131–1149.

Lin, S.-J., 2004: A "vertically Lagrangian" finite-volume dynamical core for global models. *Mon. Wea. Rev.*, **132**, 2293–2307.

Lin, S.-J. and R. B. Rood, 1996: Multidimensional flux-form semi-Lagrangian transport scheme. *Mon. Wea. Rev.*, **124**, 2046–2070.

— 1997: An explicit flux-form semi-Lagrangian shallow water model on the sphere. *Quart. J. Roy. Meteor. Soc.*, **123**, 2477–2498.

Machenhauer, B., 1979: The spectral method. *Numerical Methods Used in Atmospheric Models*, A. Kasahara, ed., GARP Publications Series No 17, WMO and ICSU, Geneva, volume 2, 121–275.

Majewski, D., D. Liermann, P. Prohl, B. Ritter, M. Buchhold, T. Hanisch, G. Paul, W. Wergen, and J. Baumgardner, 2002: The operational global icosahedral-hexagonal gridpoint model GME: Description and high-resolution tests. *Mon. Wea. Rev.*, **130**, 319–338.

Monaco, A. V. and R. T. Williams, 1975: An atmospheric global prediction model using a modified Arakawa differencing scheme. Technical report, Dept. of Meteorology, Naval Postgraduate School, Monterey, CA, NPS-51WU75041, 86pp.

Phillips, N. A., 1957: A coordinate system having some special advantages for numerical forecasting. *J. Meteor.*, **14**, 184–185.

— 1959: Numerical integration of the primitive equations on the hemisphere. *Mon. Wea. Rev.*, **87**, 333–345.

Polvani, L. M. and R. Saravanan, 2000: The three-dimensional structure of breaking Rossby waves in the polar wintertime stratosphere. *J. Atmos. Sci.*, **57**, 3663–3685.

Polvani, L. M., R. K. Scott, and S. J. Thomas, 2004: Numerically converged solutions of the global primitive equations for testing the dynamical core of atmospheric GCMs. *Mon. Wea. Rev.*, **132**, 2539–2552.

Simmons, A. J. and D. M. Burridge, 1981: An energy and angular-momentum conserving vertical finite-difference scheme and hybrid vertical coordinates. *Mon. Wea. Rev.*, **109**, 758–766.

Simmons, A. J. and B. J. Hoskins, 1975: A comparison of spectral and finite-difference simulations of a growing baroclinic wave. *Quart. J. Roy. Meteor. Soc.*, **101**, 551–565.

— 1976: Baroclinic instability on the sphere: Normal modes of the primitive and quasi-geostrophic equations. *J. Atmos. Sci.*, **33**, 1454–1477.

— 1977: Baroclinic instability on the sphere: Solutions with a more realistic tropopause. *J. Atmos. Sci.*, **34**, 581–588.

— 1979: The downstream and upstream development of unstable baroclinic waves. *J. Atmos. Sci.*, **36**, 1239–1254.

Tomita, H. and M. Sato, 2004: A new dynamical framework of nonhydrostatic global model using the icosahedral grid. *Fluid Dyn. Res.*, **34**, 357–400.

U.S. Standard Atmosphere, 1976: U.S. Government Printing Office, Washington D.C.

Williamson, D. L., J. B. Drake, J. J. Hack, R. Jakob, and P. N. Swarztrauber, 1992: A standard test set for numerical approximations to the shallow water equations in spherical geometry. *J. Comput. Phys.*, **102**, 211–224.

Williamson, D. L. and J. G. Olson, 1994: Climate simulations with a semi-Lagrangian version of the NCAR Community Climate Model. *Mon. Wea. Rev.*, **122**, 1594–1610.

Williamson, D. L., J. G. Olson, and B. A. Boville, 1998: A comparison of semi-Lagrangian and Eulerian tropical climate simulations. *Mon. Wea. Rev.*, **126**, 1001–1012.

Williamson, D. L., J. G. Olson, and C. Jablonowski, 2006: Two dynamical core formulation flaws exposed by a baroclinic instability test case. To be submitted to J. Geophys. Res.

Williamson, D. L. and P. J. Rasch, 1989: Two-dimensional semi-Lagrangian transport with shape-preserving interpolation. *Mon. Wea. Rev.*, **117**, 102–129.